SCUOLA DI DOTTORATO
UNIVERSITÀ DEGLI STUDI DI MILANO-BICOCCA

Dipartimento di Fisica "Giuseppe Occhialini"

Dottorato di Ricerca in Fisica e Astronomia - XXXV Ciclo
Curriculum in Fisica Teorica

Next-to-next-to-leading order predictions for diboson production in hadronic scattering combined with parton showers

Alessandro Gavardi
Mat. 777058

Tutor: Prof. Simone Alioli
Coordinator: Prof. Stefano Ragazzi

ANNO ACCADEMICO 2021/2022

Abstract

In this work, I present the implementations of two processes of electroweak (EW) boson pair production from hadronic scattering within two different Monte Carlo event generators at next-to-next-to-leading order (NNLO) in quantum chromodynamics (QCD) combined with parton showers (PS).

In the first part of the work, I discuss the implementation of the process of production of two same-flavor opposite-charge pairs of massless leptons from proton-proton scattering within the GENEVA Monte Carlo event generator. After briefly introducing the GENEVA method, I provide a detailed description of two of its newly-implemented features. After passing the events through the PYTHIA8 parton shower, I finally show several distributions of phenomenological interest and compare them with the data from the ATLAS and CMS experiments at the Large Hadron Collider (LHC).

The GENEVA event generator provides a framework for matching the NNLO calculation with the next-to-next-to-leading logarithmic prime (NNLL$'$) resummation of the zero-jettiness and next-to-leading logarithmic (NLL) resummation of the one-jettiness. Since the contribution from the resummation is only differential in the N-jettiness parameter, it can be used for generating events only after providing its dependence on the full radiation phase space. The functions used for this purpose are called splitting functions and must be normalized so as not to spoil the accuracy of the resummation. In this work, I present a way of normalizing them on the fly, which provides better stability to the Monte Carlo integration. However, such a method requires the analytic computation of several phase-space boundaries, which depend on the mappings used for projecting the configurations with $N + 1$ final-state partons onto those with N final-state partons. After describing all the mappings currently available in GENEVA, I present a detailed calculation of the normalization of the corresponding splitting functions. I then discuss the next-to-leading order (NLO) subtraction of the infrared QCD singularities for any process of production of a color singlet. Since GENEVA requires the on-the-fly Monte Carlo integration of the subtracted real amplitudes, I show a way to optimize the efficiency of the integration, which can be particularly useful for processes where the evaluation of the real matrix elements is computationally demanding.

In the second part of the work, I discuss the implementation of the process of production of a photon pair from a proton-proton scattering within the POWHEG BOX+MINNLO$_{\text{PS}}$ Monte Carlo event generator. Such a process requires a dedicated treatment since it is plagued by quantum electrodynamics (QED) divergences in the limit where any photons become collinear to a quark. After briefly introducing the POWHEG BOX event generator and the MINNLO$_{\text{PS}}$ method, I present the dedicated tools devised for this calculation. I begin by describing a generic way to deal with any process with a divergent Born cross section in the POWHEG BOX event generator without applying any generation-level cuts. I then present a mapping that prevents QED-finite configurations

with one final-state parton from being projected to singular configurations with no final-state partons. Finally, I discuss several modifications to the original version of the MiNNLO$_{\rm PS}$ method aimed at reducing the size of spurious contributions beyond NNLO. After passing the events through the Pythia8 parton shower, I conclude by showing several distributions of phenomenological interest and comparing them with the most recent LHC data from the ATLAS experiment.

Keywords: NNLO, QCD, Event Generator, Parton Shower, EW Bosons

Sommario

In questo lavoro presento le implementazioni di due processi di produzione di una coppia di bosoni elettrodeboli (EW) dallo scattering di due adroni in due diversi generatori di eventi Monte Carlo all'ordine next-to-next-to-leading (NNLO) nella cromodinamica quantistica (QCD) combinati con la parton shower (PS).

Nella prima parte della tesi discuto l'implementazione del processo di produzione di due coppie di leptoni privi di massa con lo stesso sapore e carica opposta dallo scattering protone-protone all'interno del generatore di eventi Monte Carlo GENEVA. Dopo aver brevemente introdotto il metodo GENEVA, fornisco una descrizione dettagliata di due delle sue funzioni recentemente implementate. Dopo aver passato gli eventi attraverso la parton shower di PYTHIA8, mostro infine diverse distribuzioni di interesse fenomenologico e le confronto con i dati degli esperimenti ATLAS e CMS al Large Hadron Collider (LHC).

Il generatore di eventi GENEVA consente di abbinare il calcolo NNLO con la resummazione all'ordine logaritmico next-to-next-to-leading primo (NNLL$'$) della zero-jettiness e quella all'ordine logaritmico next-to-leading (NLL) della one-jettiness. Poiché il contributo della risommazione è differenziale nel solo parametro della N-jettiness, può essere utilizzato per generare eventi soltanto dopo aver fornito la sua dipendenza dall'intero spazio delle fasi di radiazione. Le funzioni utilizzate a questo scopo sono dette funzioni di splitting e devono essere normalizzate in modo da non compromettere l'accuratezza della risommazione. In questo lavoro presento un modo per normalizzarle on the fly, che fornisce una migliore stabilità all'integrazione Monte Carlo. Tuttavia, tale metodo richiede il calcolo analitico di diversi limiti dello spazio delle fasi che dipendono dalle mappe utilizzate per proiettare le configurazioni con $N + 1$ partoni di stato finale su quelle con N partoni di stato finale. Dopo aver descritto tutte le proiezioni attualmente disponibili in GENEVA, presento un calcolo dettagliato della normalizzazione delle corrispondenti funzioni di splitting. Successivamente discuto la sottrazione all'ordine next-to-leading (NLO) delle singolarità infrarosse di QCD per qualsiasi processo di produzione di un singoletto di colore. Poiché GENEVA richiede l'integrazione Monte Carlo on-the-fly delle ampiezze reali sottratte, mostro un modo per ottimizzare l'efficienza dell'integrazione che può essere particolarmente utile per i processi in cui il calcolo degli elementi di matrice reali è computazionalmente impegnativa.

Nella seconda parte della tesi discuto l'implementazione del processo di produzione di una coppia di fotoni da uno scattering protone-protone all'interno del generatore di eventi Monte Carlo POWHEG BOX+MINNLO$_{\text{PS}}$. Tale processo richiede un trattamento dedicato poiché è afflitto da divergenze di elettrodinamica quantistica (QED) nel limite in cui qualsiasi fotone diventa collineare a un quark. Dopo aver brevemente introdotto il generatore di eventi POWHEG BOX e il metodo MINNLO$_{\text{PS}}$, presento gli strumenti appositamente creati per questo calcolo. Comincio descrivendo una tecnica generale per trattare qualsiasi processo con una sezione d'urto Born divergente nel generatore di eventi POWHEG BOX senza applicare alcun taglio a livello di generazione. Presento quindi una mappa che impedisce che le configurazioni finite dal punto di vista della QED

con un partone di stato finale siano proiettate su configurazioni singolari senza partoni di stato finale. Infine discuto alcune modifiche alla versione originale del metodo MiNNLO$_{\rm PS}$ volte a ridurre l'impatto dei contributi spuri oltre il NNLO. Dopo aver passato gli eventi attraverso la parton shower di Pythia8, concludo mostrando diverse distribuzioni di interesse fenomenologico e confrontandole con i dati di LHC più recenti dall'esperimento ATLAS.

Parole Chiave: NNLO, QCD, Event Generator, Parton Shower, EW Bosons

Declaration

This dissertation is a result of my own efforts. The work to which it refers is based on my Ph.D. research projects:

1. Simone Alioli et al. "Next-to-next-to-leading order event generation for Z boson pair production matched to parton shower". In: *Phys. Lett. B* 818 (2021), p. 136380. DOI: 10.1016/j.physletb.2021.136380. arXiv: 2103.01214 [hep-ph]

2. Alessandro Gavardi, Carlo Oleari, and Emanuele Re. "NNLO+PS Monte Carlo simulation of photon pair production with MiNNLO$_{PS}$". In: *JHEP* 09 (2022), p. 061. DOI: 10.1007/JHEP09(2022)061. arXiv: 2204.12602 [hep-ph]

I hereby declare that except where specific reference is made to the work of others, the contents of this dissertation are original and have not been submitted in whole or in part for consideration for any other degree or qualification in this, or any other university.

October 27, 2022 Alessandro Gavardi

Contents

Chapter 1

Introduction

Among the most useful experimental tools for investigating the subatomic structure of the matter are the colliders, machines where electromagnetic fields are used for accelerating two beams of particles and making them collide with each other. Currently, the world most high-energetic collider is the LHC, located at the CERN laboratory in Geneva, Switzerland, where two beams of protons are accelerated up to a center-of-mass energy $\sqrt{S} = 13$ TeV. Due to the electric charge of the proton, most of the collisions end up in elastic scatterings. However, one of the predictions of QCD is that, at such high energies, the strong force that is responsible for the confinement of the quarks and gluons within the proton loses intensity, and the accelerated protons start progressively to behave less as a bounded state and more as a superposition of free partons. When two partons belonging to the two different beams interact (in what is typically referred to as a *hard* scattering) new particles are produced. Studying the probability with which this happens is a powerful way to expose the most fundamental laws of nature. In particular, the mass distributions of subsets of particles produced in the collisions offers a direct way of discovering new massive particles by looking for their resonances. The search for large mass resonances is indeed one of the main motivation for building colliders capable to reach higher and higher energies.

The main success of the LHC has probably been the observation of the Higgs boson in 2012, which at the time remained the last unobserved particle predicted by the Standard Model. In the following years, due to the lack of a clear path towards the discovery of new particles, because of a general good agreement between the theoretical predictions based on the Standard Model and the experimental results, the LHC has progressively evolved into a precision machine. The goal has then become to lower the systematic and statistical uncertainties of the experimental results up to the point where even small discrepancies with respect to the Standard Model predictions could be exposed, which would give us hints on where to look for new physics. An interesting class of particles for making precision studies are the EW vector bosons, which, due to the fact that they do not undergo QCD interactions, have very clean signatures.

The chances of success of the LHC as a machine for precision studies relies, however, on the assumption that the theoretical uncertainties on the Standard Model predictions can be lowered to a size comparable to the experimental ones. One of the best tools for reaching such a goal are the Monte Carlo event generators, whose aim is exactly to simulate events, the name we give to the outcome of the collisions (i.e. the set of particles produced after the scattering with associated momenta). Historically, the first event generators to be implemented were only able to provide an accurate description of the QCD emissions in their collinear (parton showers) and/or soft limit (dipole showers). An extension to this approach was obtained by matching the showers to the tree-level matrix elements of the process with one or more jets (ME+PS), thus improving the accuracy of the description of the scattering also far from the soft and collinear regions of the phase space. This can be achieved by matching LO matrix elements to general purpose Monte Carlo event generators like Pythia [3], Herwig [4, 5] or Sherpa [6] (in some cases it can even be done automatically within such event generators).

Another direction of improvement consists instead in combining the shower with a partonic event generator with higher accuracy. Two notable methods that combine a QCD NLO partonic event generator with the shower (NLO+PS) are MC@NLO [7] and Powheg [8, 9, 10]. By doing so, they are able to produce NLO distributions for the observables that are inclusive over the real radiation, and LO distributions for those that require one additional jet. An extension to such methods is obtained by matching two NLO calculations, one with one more resolved parton than the other, thus allowing to reach NLO accuracy also for the observables that require one additional jet with respect to the Born process. Among the methods that provide such a matching there are MiNLO [11, 12], MEPS@NLO [13] FxFx [14] and UNLOPS [15].

The latest development in this direction has been the extension of the partonic event generator to the NNLO in QCD. Two notable NNLO+PS event generators are MiNNLO$_{\text{PS}}$ [16, 17] and Geneva. In the last few years several LHC processes have been implemented in the Geneva and MiNNLO$_{\text{PS}}$ event generators, covering Drell-Yan [18, 16, 19], Higgs boson [16], VH [20], $\gamma\gamma$ [21, 2], $V\gamma$ [22, 23], VV [1, 24, 25, 26] and $t\bar{t}$ [27] production.

In this thesis, I will present the implementations of two processes of boson pair production from hadronic scattering in two different NNLO QCD Monte Carlo event generators. In the first part, I will discuss the process of production of two same-flavor opposite-charge pairs of massless leptons within the Geneva event generator, while the second one will be on the process of production of two photons within the MiNNLO$_{\text{PS}}$+Powheg Box event generator.

The first part begins with a brief introduction to the Soft-Collinear Effective Theory (SCET) resummation in chapter 3 and the Geneva method in chapter 4. It continues with a detailed description of two newly-implemented features of the Geneva event generator that can be useful also for other color-singlet production processes. In chapter 5, I present a new implementation of the splitting functions (i.e. the functions used for making the contributions from the resummation differential over the entire phase space), which allows to compute their normal-

ization factor on the fly. Since such a method requires us to know the analytic expression for the boundaries of the radiation phase space for all the phase-space mappings employed, in chapters 6 and 7 I describe the default GENEVA mappings and compute the expression for their boundaries. An alternative mapping from the phase space with two final-state partons to that with one final-state parton is presented in chapter A of the appendix. In chapter 8, instead I present a way of optimizing the efficiency of the infrared NLO subtraction for the case of color-singlet production, which can be particularly useful for processes where the computation of the real matrix elements is computationally demanding. Finally, in chapter 9 I validate the entire implementation against the independent results provided by the MATRIX fixed-order calculation, and present the comparisons with the LHC data from the ATLAS and CMS experiments for several distributions of phenomenological interest.

The second part begins with a brief introduction to the MINNLO$_{\text{PS}}$ and POWHEG methods in chapters 10 and 11 respectively, and continues in chapter 12 with the description of the dedicated treatment that the process of photon pair production requires due to the presence of QED divergences. In particular, I start by discussing a general way of treating processes with a divergent Born cross section within the POWHEG BOX event generator. I then introduce a mapping that prevents QED-finite configurations with one final-state parton from being projected to singular configurations with no final-state partons. Finally, I conclude by discussing several modifications to the original version of the MINNLO$_{\text{PS}}$ method [16, 17] aimed at reducing the size of spurious contributions beyond NNLO. A detailed discussion on the way scale variations are performed within the MINNLO$_{\text{PS}}$ method to estimate the theoretical uncertainties is furthermore presented in chapter B of the appendix. Finally, in chapter 13 I validate the entire implementation against the independent result provided by the MATRIX fixed-order calculation, and present the comparisons with the LHC data from the ATLAS experiment for several distributions of phenomenological interest.

Chapter 2

Infrared subtraction and resummation

In QCD, the amplitudes of any process are affected by non-integrable divergences in the limit where the energy of any final-state gluon is small (soft limit) or the momenta of two of the partons treated as massless (either belonging to the initial or final state) are parallel, as long as they represent a valid splitting (collinear limit). The three valid QCD splittings are the emissions of a gluon from a quark ($q \to q\,g$ splitting) or a gluon ($g \to g\,g$ splitting), and the production of a quark-antiquark pair from a gluon ($g \to q\,\bar{q}$ splitting). The origin of such singularities ultimately lays in the expression of the QCD propagators, whose denominator (in the case where all the involved partons are treated as massless) is proportional to $E_i E_j\,(1-\cos\theta)$, where we called E_i and E_j the energies of the two partons produced in the splitting (in the following emitted and sister partons) and θ the angle between their momenta. However, one of the theory most important results is that, in the collinear limit, the tree-level amplitude $R(\Phi_{n+1})$ for the process with $n+1$ final-state partons factorizes on the underlying tree-level amplitude $B(\Phi_n)$ where the two collinear partons have been substituted by one single parton (in the following emitter parton) whose momentum is the sum of the momenta of the two original partons. This factorization property is universal and can be written as

$$R(\Phi_{n+1}) \to \frac{8\pi\alpha_{\mathrm{S}}}{t}\,P_{kj}^{\mathrm{AP}}(z)\,B(\Phi_n)\,, \tag{2.1}$$

where α_{S} is the strong coupling, and we called $t = (p_i + p_j)^2$ (with p_i and p_j being the momenta of the emitted and sister partons, respectively) the virtuality of the underlying parton, and $z = E_j/(E_i + E_j)$ the fraction of energy carried by the sister parton. The Altarelli–Parisi splitting functions P_{kj}^{AP} are four universal functions that depend on the flavor of the emitter k and the sister j. Their expressions will be given in eq. (3.24). Since in this chapter we are more interested in presenting the concept of resummation, rather than studying its

details, we focus on the simplest case where the emitted parton is a gluon close to its soft limit (the soft-collinear limit), in which case eq. (2.1) simplifies to

$$R(\Phi_{n+1}) \to \frac{8\pi\alpha_{\text{S}} C_i}{E^2\,(1-\cos\theta)}\, B(\Phi_n)\,, \tag{2.2}$$

where C_i is a Casimir factor of the SU(3) group ($C_i = C_{\text{F}} = 4/3$ in case of a $q \to q\,g$ splitting, $C_i = C_{\text{A}} = 3$ in case of a $g \to g\,g$ splitting), E is the gluon energy and θ the angle with respect to the sister parton. Since, in the same limit, the phase space $d\Phi_{n+1}$ for the process with $n+1$ final-state partons factorizes on the phase space $d\Phi_n$ for the underlying process as

$$d\Phi_{n+1} = \frac{E\,dE\,d\cos\theta}{8\pi^2}\,\frac{d\phi}{2\pi}\,d\Phi_n, \tag{2.3}$$

where ϕ is the azimuthal angle of the emission, the cross section σ_{n+1} can be written as

$$\sigma_{n+1} = \int d\Phi_{n+1}\, R(\Phi_{n+1}) \to \int d\Phi_n\, B(\Phi_n)\,\frac{\alpha_{\text{S}}}{\pi}\,C_i \int \frac{dE}{E} \int \frac{d\cos\theta}{1-\cos\theta} \int \frac{d\phi}{2\pi}, \tag{2.4}$$

which, as anticipated, is non-integrable in the limits of small E and θ.

The fact that this same problem of non-integrability arises with an opposite sign in the computation of the one-loop correction $V(\Phi_n)$ to the underlying amplitude suggests that what we are observing is not an issue of the full QCD theory, but a problem introduced by its perturbative expansion, as shown by the Kinoshita–Lee–Nauenberg theorem [28, 29]. However, to prove that the singularity coming from the integral of eq. (2.4) is exactly canceled by the one-loop correction, we need a way of regularizing it. To do that, we observe that the singularity would not be present in a phase space defined on $D > 4$ space-time dimensions, where the same integral would read

$$\sigma^{(D)}_{n+1} \to \int d\Phi_n\, B(\Phi_n)\,\frac{\alpha_{\text{S}}}{\pi}\,C_i \int \frac{dE}{E}\left(\frac{E}{\mu}\right)^{D-4} \int \frac{d\cos\theta}{1-\cos\theta}\,\sin^{D-4}\theta \int \frac{d\Omega^{(D-2)}}{2\pi}, \tag{2.5}$$

where we have introduced the scale μ in order not to change the physical dimensions of the resulting cross section, and the solid angle $\Omega^{(D-2)}$ in $D-2$ dimensions. At this point, after writing D as $4-2\epsilon$, the singularities of the original integral can be exposed as ϵ poles. After applying the same procedure to the loop corrections, it can be shown that they have exactly the same singular structure, with and opposite sign, which means that, provided we adopt the prescription of computing the phase space integrals in D dimensions, we can obtain a finite value for the NLO cross section if we sum the virtual and real corrections $V(\Phi_n)$ and $R(\Phi_{n+1})$ and take the limit $\epsilon \to 0$. This solution, however, cannot be straightforwardly applied to an event generator, where the integral of eq. (2.5) is done numerically in a fixed number of space-time dimensions $D = 4$. The solution to this is called infrared subtraction and consists in

introducing a counterterm $C(\Phi_{n+1})$ that reproduces the same soft and collinear divergences of $R(\Phi_{n+1})$, so that the full NLO cross section can be written as

$$\sigma_{\text{NLO}} = \int d\Phi_n \left\{ B(\Phi_n) + \lim_{D\to 4} \left[V(\Phi_n) + \int \frac{d\Phi_{n+1}^{(D)}}{d\Phi_n} C(\Phi_{n+1}) \right] \right\} + \int d\Phi_{n+1} \left[R(\Phi_{n+1}) - C(\Phi_{n+1}) \right]. \tag{2.6}$$

The singularities of the first integral can be analytically subtracted, as long as we know the expression of the integral of the counterterm $C(\Phi_{n+1})$ over the radiation phase space $d\Phi_{n+1}^{(D)}/d\Phi_n$, while the second integral (where the divergences are subtracted point by point) can now be performed numerically. The counterterm $C(\Phi_{n+1})$, by reproducing infrared limits like that reported in eq. (2.2) implicitly introduces the needing of a mapping between the $d\Phi_{n+1}$ and $d\Phi_n$ phase spaces. In order for the integral in the second line of eq. (2.6) to be well defined, such a mapping is required to project the Φ_{n+1} configurations close to the soft and collinear limits to the underlying Φ_n configuration whose virtual poles cancel the real singularities. At this point, as long as an observable O is defined such that, in the infrared limits, $O(\Phi_{n+1}) \to O(\Phi_n)$, its distribution is not affected by the infrared divergences. We call this class of observables infrared safe.

Before continuing with the discussion, we observe that treating all the quarks as massive (as they are in nature) would formally remove the collinear singularities, which could make the above procedure appear as unnecessary as far as the collinear limit is concerned. However, in such a limit, for small quark masses m the QCD propagators would still be proportional to m^2. Since the quark masses can be as small as few MeVs, while the energies of modern days colliders reach several TeVs, the matrix elements would still be affected by huge enhancements in the collinear limit, meaning that we would still need a local infrared subtraction between the virtual and real enhanced terms, in order for the Monte Carlo integrator to be efficient.

The above discussion shows how the infrared soft and collinear divergences are an artefact of the perturbative expansion of QCD. However, while the infrared subtraction by itself allows us to obtain finite predictions for all the infrared-safe observables, the distributions that are not inclusive over radiation (i.e. require the presence of an extra parton in the final state) will still present unphysical features due to the divergent behavior of the real matrix elements $R(\Phi_{n+1})$ in the infrared limits. The solution to this problem is provided by the resummation of contributions at all orders in the α_{S} expansion. To explain how this is done, we start from eq. (2.4) and rewrite the radiation integral in terms of the virtuality t and the energy fraction z, so that it reads

$$d\sigma_{n+1} = \frac{\alpha_{\text{S}}}{\pi} C_i \frac{dt}{t} \frac{dz}{1-z} \frac{d\phi}{2\pi} B(\Phi_n)\, d\Phi_n. \tag{2.7}$$

At this point we interpret

$$dp = \frac{\alpha_{\rm S}}{\pi}\, C_i\, \frac{dt}{t}\, \frac{dz}{1-z}\, \frac{d\phi}{2\pi}. \tag{2.8}$$

as the probability of having an emission with virtuality t, energy fraction z and azimuth ϕ for a given underlying configuration Φ_n, which implies that the probability $P(t_0)$ that the hardest (i.e. with the largest virtuality) emission has virtuality between t_0 and $t_1 = t_0 + dt_0$ is given by the product of the probability of having no emissions for all the intervals $dt_i = (t_{i+1} - t_i)$ for i from 1 to N up to the maximum kinematically allowed virtuality $t_{\rm max}$ times the probability of emitting in the interval dt_0

$$P(t_0) = \frac{dp}{dt}(t_0)\, dt_0 \prod_{i=1}^{N} \left(1 - \frac{dp}{dt}(t_i)\, dt_i\right) \to \frac{dp}{dt}(t_0)\, dt_0\, \exp\left(-\sum_{i=1}^{N} \frac{dp}{dt}(t_i)\, dt_i\right), \tag{2.9}$$

where the expression on the right-hand side of the above equation is obtained in the limit where the intervals dt_i are infinite and infinitely small. Going back to the continuous picture, where the sums becomes integrals, we can finally write that the probability density of the hardest QCD emission as a function of its virtuality is given by

$$\frac{dP}{dt} = \frac{\alpha_{\rm S}}{\pi}\, \frac{C_i}{t} \int \frac{dz}{1-z}\, \exp\left(-\int_t^{t_{\rm max}} \frac{\alpha_{\rm S}}{\pi}\, C_i\, \frac{dt'}{t'} \int \frac{dz}{1-z}\right). \tag{2.10}$$

The exponential function introduced in the above equation takes the name of Sudakov form factor. We highlight that it contains the strong coupling at the exponent, which makes it an all-order object with respect to the perturbative expansion. At fixed t, z belongs to the interval $\left(t/Q^2, 1 - t/Q^2\right)$ where Q is some hard scale of the process, so that, in the limit of small t, the above expression can be rewritten as

$$\frac{dP}{dt} = \frac{\alpha_{\rm S}}{\pi}\, \frac{C_i}{t}\, \log\left(\frac{Q^2}{t}\right) \exp\left(-\frac{\alpha_{\rm S}}{2\pi}\, C_i\, \log^2\left(\frac{Q^2}{t}\right)\right), \tag{2.11}$$

where we have neglected the $\log\left(Q^2/t_{\rm max}\right)$, which is not enhanced. We highlight that the above expression can be directly used as a probability density for generating the hardest emission, since it has already the correct normalization (i.e. its integral over t from 0 to Q is equal to 1).

From the numerical point of view, the above probability distribution is exactly equal to zero at $t = 0$, where before we had the singularity. However, it can be seen that its peak is still at small values of t, where the soft and collinear approximations still hold. This is a very important observation, since such approximations greatly simplify any QCD calculations, and are the principle on which dipole and parton showers are based. This example shows how the QCD singular structure, from being an obstacle in the context of fixed-order calculations, has really become an advantage in the context of resummation, due to its universal structure.

Part I

Z boson pair production with Geneva

Chapter 3

Resummation in SCET

Effective field theories are a useful tool for solving perturbatively problems of quantum field theory that involve two or more well separated scales. Such problems are generally plagued by the presence of large logarithms of the ratio of the scales that can spoil the convergence of the perturbative expansion. In the process of production of a color singlet at a hadronic collider, for example, the energy scale of the hard interaction is of the order of the mass m_{CS} of the color singlet, while the transverse momentum of the color singlet $p_{\text{T,CS}}$ typically defines the order of magnitude of the energy of the QCD emissions. In the simple example of eq. (2.11) we showed that these logarithms need to be resummed at all orders in the perturbation theory to make reliable predictions for observables that are not inclusive over the real radiation. The Soft-Collinear Effective Theory provides a framework for doing this systematically, by separating the perturbative expansion of the hard interaction from that of the lower-energy QCD emissions, predicting the structure of the terms enhanced by the logarithms of the ratio of the two scales, and resumming them at all perturbative orders.

In this chapter, we present the three fundamental ingredients of the resummation in the SCET formalism for the case of color-singlet production, i.e. the soft, beam and hard functions, and discuss their evolution from their characteristic scales to the common scale of the process. Finally, we prove that, by construction, their total cumulant is not affected by the resummation. This last property will allow us to straightforwardly match the resummed calculation to the fixed-order results within the GENEVA Monte Carlo event generator.

3.1 $\mathcal{N}$-jettiness

Instead of the transverse momentum of the color singlet, SCET was historically first developed using the so-called $\mathcal{N}$-jettiness as the lower scale of the process. Given a configuration Φ_N with a color singlet and N final-state partons of

momenta p_1, ..., p_N in the laboratory frame, the $\mathcal{N}$-jettiness is defined as

$$\mathcal{T}_{\mathcal{N}} = \sum_{i=1}^{N} \min_{\substack{q_1,\,...,\,q_{\mathcal{N}} \\ \text{lightlike with } q_i^0 = 1}} \left(q_a \cdot \hat{p}_i, q_b \cdot \hat{p}_i, q_1 \cdot \hat{p}_i, ..., q_{\mathcal{N}} \cdot \hat{p}_i\right), \tag{3.1}$$

where $q_a = (1,0,0,1)$, $q_b = (1,0,0,-1)$, and q_1, ..., $q_{\mathcal{N}}$ can be any lightlike vectors with $q_i^0 = 1$. Furthermore we used the $\hat{}$ symbol to refer to the momenta longitudinally boosted from the laboratory frame to the frame where the color singlet has zero rapidity.

The $\mathcal{N}$-jettiness can be used as a resolution parameter for the radiative emissions of the process. The q_i vectors that minimize the above definition can be thought of as the directions of the $\mathcal{N}$ hardest jets, so that any configuration with $\mathcal{N}$ or less final-state partons has $\mathcal{T}_{\mathcal{N}} = 0$. Any additional emission that is neither soft nor collinear leads instead to a positive value of $\mathcal{T}_{\mathcal{N}}$, so that we can interpret the $\mathcal{N}$-jettiness as a measure of how much the configuration differ from a configuration with $\mathcal{N}$ final-state partons.

The expression for the 0-jettiness reduces to

$$\mathcal{T}_0 = \sum_{i=1}^{N} \min\left(\hat{p}_i^+, \hat{p}_i^-\right), \tag{3.2}$$

where we have introduced the plus and minus components of the i-th momentum as

$$\hat{p}_i^{\pm} = \hat{p}_i^0 \mp \hat{p}_i^3, \tag{3.3}$$

and can be interpreted as a measure of the quantity of QCD radiation far from the hadronic beams.

3.2 Zero-jettiness resummation

We consider the process of production of a color singlet (CS) of mass Q from the scattering of two hadrons a and b, and we call x_a and x_b the fraction of momenta of a and b taken by the partons k_a and $\bar{k}_b$ which undergo the hard interaction. Using the SCET factorization theorem presented for example in eq. (1.6) of ref. [30], we can write the $\mathcal{T}_0$ spectrum of the resummed cross section differential over the Born phase space $d\Phi_0$ for such a process as

$$\begin{aligned}\frac{d\sigma_{\text{res}}}{d\Phi_0\, d\mathcal{T}_0} = \sum_{k_a \bar{k}_b} H_{k_a \bar{k}_b}(\Phi_0, \mu) \int dt_a \int dt_b\, B^a_{k_a}(t_a, x_a, \mu)\, B^b_{\bar{k}_b}(t_b, x_b, \mu) \\ \times S_{k_a \bar{k}_b}\left(\mathcal{T}_0 - \frac{t_a + t_b}{Q}, \mu\right),\end{aligned} \tag{3.4}$$

where we have introduced the hard function $H_{k_a \bar{k}_b}$, the two beam functions $B^a_{k_a}$ and $B^b_{\bar{k}_b}$, and the soft function $S_{k_a \bar{k}_b}$, all of them dependent on the resummation scale μ. The hard function describes the hard interaction from which the color

singlet is produced and incorporates the virtual radiation. The two beam functions describe the initial-state radiation collinear to the beams with virtuality $-t_a$ and $-t_b$ respectively, in the limit $t_a, t_b \ll Q$. Finally, the soft function describes the soft radiation.

To simplify the expression presented in eq. (3.4), we introduce the Laplace transform of a function f as

$$\mathcal{L}\{f\} = \tilde{f}(s) = \int_0^\infty dt\, e^{-st} f(t)\,, \tag{3.5}$$

and use it to rewrite the factorization theorem as

$$\mathcal{L}\left\{\frac{d\sigma_{\rm res}}{d\Phi_0\, d\mathcal{T}_0}\right\} = \sum_{k_a k_b} H_{k_a \bar{k}_b}(\Phi_0,\mu)\, \tilde{B}^a_{k_a}\left(\frac{s}{Q}, x_a, \mu\right) \tilde{B}^b_{\bar{k}_b}\left(\frac{s}{Q}, x_b, \mu\right) \tilde{S}_{k_a \bar{k}_b}(s,\mu)\,. \tag{3.6}$$

To be able to write the explicit expressions for the hard, beam and soft functions in a compact form in the following sections of this chapter, it is useful to define

$$\mathcal{L}_n(x) = \lim_{\beta\to 0^+}\left[\theta(x-\beta)\,\frac{\log^n x}{x} + \delta(x-\beta)\,\frac{\log^{n+1}\beta}{n+1}\right] \tag{3.7}$$

and

$$\mathcal{L}^\eta(x) = \lim_{\beta\to 0^+}\left[\frac{\theta(x-\beta)}{x^{1-\eta}} + \delta(x-\beta)\,\frac{\beta^\eta - 1}{\eta}\right], \tag{3.8}$$

and their Laplace transforms, which read

$$\int_0^\infty dt\, e^{-st}\, \mathcal{L}^\eta(t) = s^{-\eta}\,\Gamma(\eta) - \frac{1}{\eta} \tag{3.9}$$

and

$$\int_0^\infty dt\, e^{-st}\, \mathcal{L}_n(t) = \frac{1}{n+1}\int_0^\infty dx\, e^{-x}\, \log^{n+1}\!\left(\frac{x}{s}\right). \tag{3.10}$$

The above expressions can be obtained performing the integration appearing in the Laplace transform for a generic value of $\beta > 0$, and then taking the limit $\beta \to 0^+$. In particular, in the upcoming sections we will make use of the formulae

$$\int_0^\infty dt\, e^{-st}\, \mathcal{L}_0(t) = -\left(\log s + \gamma\right) \tag{3.11}$$

and

$$\int_0^\infty dt\, e^{-st}\, \mathcal{L}_1(t) = \frac{1}{2}\left[\left(\log s + \gamma\right)^2 + \frac{\pi^2}{6}\right]. \tag{3.12}$$

3.3 The soft function

Following eq. (2.24) of ref. [31], the soft function can be expressed as the convolution

$$S_{k\bar{\ell}}(k,\mu) = \int_0^k dk'\, S_{k\bar{\ell}}(k-k',\mu_{\rm S})\, U_{\rm S}(k',\mu_{\rm S},\mu)\,. \tag{3.13}$$

The soft function for the production of a color singlet at the soft scale $\mu_{\rm S}$ only depends on whether the Born process is quark- or gluon-initiated. The two expressions can be taken respectively from eq. (155) of ref. [32] and eqs. (2.22-2.23) of ref. [31] and, at NLO, read

$$\mu_{\rm S}\, S_{k\bar{\ell}}(k,\mu_{\rm S}) = \delta_{k\ell}\,\delta\!\left(\frac{k}{\mu_{\rm S}}\right) + \frac{\alpha_{\rm S}(\mu_{\rm S})}{2\pi}\, C_{k\ell}\left[-8\,\mathcal{L}_1\!\left(\frac{k}{\mu_{\rm S}}\right) + \frac{\pi^2}{6}\,\delta\!\left(\frac{k}{\mu_{\rm S}}\right)\right] + \mathcal{O}\big(\alpha_{\rm S}^2\big)\,, \tag{3.14}$$

where we have introduced

$$C_{qq} = C_{\rm F} \qquad\qquad C_{gg} = C_{\rm A}. \tag{3.15}$$

By directly substituting the expression given in eq. (3.14) in the $\mathcal{T}_0$ spectrum presented in eq. (3.4) we would obtain a divergent result in the limit $\mathcal{T}_0 \to 0$. This can be avoided by resumming the singular contributions at all orders of the strong coupling. In the SCET formalism such a resummation is achieved by evolving the soft function from its characteristic scale $\mu_{\rm S}$ to the common scale μ of the process according to the formula of eq. (3.13). The evolution kernel is presented for example in eq. (2.25) of ref. [31] and reads

$$\mu_{\rm S}\, U_{\rm S}(k,\mu_{\rm S},\mu) = \frac{e^{K_{\rm S}(\mu_{\rm S},\mu)-\gamma\eta_{\rm S}(\mu_{\rm S},\mu)}}{\Gamma(1+\eta_{\rm S}(\mu_{\rm S},\mu))}\left[\delta\!\left(\frac{k}{\mu_{\rm S}}\right) + \eta_{\rm S}(\mu_{\rm S},\mu)\,\mathcal{L}^{\eta_{\rm S}(\mu_{\rm S},\mu)}\!\left(\frac{k}{\mu_{\rm S}}\right)\right], \tag{3.16}$$

where

$$K_{\rm S} = -4K_\Gamma + K_{\gamma_{\rm S}} \qquad\qquad \eta_{\rm S} = 4\eta_\Gamma. \tag{3.17}$$

The explicit expression for K_Γ, $K_{\gamma_{\rm S}}$ and η_Γ will be given in section 3.8.

After applying the Laplace transform defined in eq. (3.5), the convolution of eq. 3.13 can be reduced to the product

$$\tilde{S}_{k\bar{\ell}}(s,\mu) = \tilde{S}_{k\bar{\ell}}(s,\mu_{\rm S})\,\tilde{U}_{\rm S}(s,\mu_{\rm S},\mu)\,, \tag{3.18}$$

where, using eq. (3.9),

$$\tilde{U}_{\rm S}(s,\mu_{\rm S},\mu) = e^{K_{\rm S}(\mu_{\rm S},\mu)-\gamma\eta_{\rm S}(\mu_{\rm S},\mu)}\,(s\mu_{\rm S})^{-\eta_{\rm S}(\mu_{\rm S},\mu)} \tag{3.19}$$

and, using eq. (3.12),

$$\tilde{S}_{k\bar{\ell}}(s,\mu_{\rm S}) = \delta_{k\ell} + \frac{\alpha_{\rm S}(\mu_{\rm S})}{2\pi}\, C_{k\ell}\left\{-4\left[\big(\log(s\mu_{\rm S})+\gamma\big)^2 + \frac{\pi^2}{6}\right] + \frac{\pi^2}{6}\right\} + \mathcal{O}\big(\alpha_{\rm S}^2\big)\,. \tag{3.20}$$

3.4 The beam function

Following eq. (2.17) of ref. [31], the beam function can be expressed as the convolution

$$B_k^h(t,x,\mu) = \int_0^t dt'\, B_k^h(t-t',x,\mu_{\rm B})\, U_{\rm B}(t',\mu_{\rm B},\mu)\,. \tag{3.21}$$

The beam function $B_k^h(t, x, \mu_{\rm B})$ for the production of a color singlet at the beam scale $\mu_{\rm B}$ only depends on whether the Born process is quark- or gluon-initiated. The two expressions can be taken respectively from eqs. (2.20), (2.38) and (3.48) of ref. [30] and eqs. (2.12-2.15) and (A.16) of ref. [31] and, at NLO, read

$$B_k^h(t, x, \mu_{\rm B}) = \sum_j \int_x^1 \frac{dz}{z}\, \mathcal{I}_{kj}(t, z, \mu_{\rm B})\, f_j^h\Big(\frac{x}{z}, \mu_{\rm B}\Big)\,, \tag{3.22}$$

where the index j runs over all the possible partons, $f_j^h(\xi, \mu)$ is the parton distribution function (PDF) of the parton j in the hadron h at momentum fraction ξ and factorization scale $\mu_{\rm B}$, and

$$\begin{aligned}\mu_{\rm B}^2\, \mathcal{I}_{kj}(t, z, \mu_{\rm B}) = {}& \delta\!\left(\frac{t}{\mu_{\rm B}^2}\right) \delta_{kj}\, \delta(1-z) + \frac{\alpha_{\rm S}(\mu_{\rm B})}{2\pi} \left\{ \mathcal{L}_1\!\left(\frac{t}{\mu_{\rm B}^2}\right) 2C_{kj}\, \delta(1-z) \right. \\ & + \mathcal{L}_0\!\left(\frac{t}{\mu_{\rm B}^2}\right) (1-z)\, P_{kj}^{\rm AP}(z)\, \mathcal{L}_0(1-z) \\ & + \delta\!\left(\frac{t}{\mu_{\rm B}^2}\right) \left[P_{kj}^{\rm AP}(z) \left((1-z)\, \mathcal{L}_1(1-z) - \log z \right) \right. \\ & \left. \left. - \frac{\pi^2}{6}\, C_{kj}\, \delta(1-z) + P'_{kj}(z) \right] \right\} + \mathcal{O}\big(\alpha_{\rm S}^2\big)\,, \end{aligned} \tag{3.23}$$

where we have introduced the Altarelli–Parisi splitting functions

$$\begin{aligned} P_{qq}^{\rm AP}(z) &= C_{\rm F}\, \frac{1+z^2}{1-z} & P'_{qq}(z) &= C_{\rm F}\,(1-z) \\ P_{qg}^{\rm AP}(z) &= T_{\rm F} \left[z^2 + (1-z)^2 \right] & P'_{qg}(z) &= 2\, T_{\rm F}\, z\, (1-z) \\ P_{gq}^{\rm AP}(z) &= C_{\rm F}\, \frac{1+(1-z)^2}{z} & P'_{gq}(z) &= C_{\rm F} z \\ P_{gg}^{\rm AP}(z) &= 2C_{\rm A} \left[\frac{z}{1-z} + \frac{1-z}{z} + z\,(1-z) \right] & P'_{gg}(z) &= 0. \end{aligned} \tag{3.24}$$

As explained for the soft function in the previous section, the beam function presented in eq. (3.22) needs to be resummed at all orders of the strong coupling by evolving it from its characteristic scale $\mu_{\rm B}$ to the common scale μ of the process according to the formula of eq. (3.21). The evolution kernel is presented for example in eq. (2.18) of ref. [31] and reads

$$\mu_{\rm B}^2\, U_{\rm B}(t, \mu_{\rm B}, \mu) = \frac{e^{K_{\rm B}(\mu_{\rm B}, \mu) - \gamma\eta_{\rm B}(\mu_{\rm B}, \mu)}}{\Gamma(1 + \eta_{\rm B}(\mu_{\rm B}, \mu))} \left[\eta_{\rm B}(\mu_{\rm B}, \mu)\, \mathcal{L}^{\eta_{\rm B}(\mu_{\rm B}, \mu)}\!\left(\frac{t}{\mu_{\rm B}^2}\right) + \delta\!\left(\frac{t}{\mu_{\rm B}^2}\right) \right], \tag{3.25}$$

where

$$K_{\rm B} = 4K_\Gamma + K_{\gamma_{\rm B}} \qquad\qquad \eta_{\rm B} = -2\eta_\Gamma. \tag{3.26}$$

The explicit expression for K_Γ, $K_{\gamma_{\rm B}}$ and η_Γ will be given in section 3.8.

After applying the Laplace transform defined in eq. (3.5), the convolution of eq. 3.22 can be reduced to the product

$$\tilde{B}_k^h(s,x,\mu) = \tilde{B}_k^h(s,x,\mu_{\rm B})\,\tilde{U}_{\rm B}(s,\mu_{\rm B},\mu)\,, \tag{3.27}$$

where, using eq. (3.9),

$$\tilde{U}_{\rm B}(s,\mu_{\rm B},\mu) = e^{K_{\rm B}(\mu_{\rm B},\mu)-\gamma\eta_{\rm B}(\mu_{\rm B},\mu)}\left(s\mu_{\rm B}^2\right)^{-\eta_{\rm B}(\mu_{\rm B},\mu)}. \tag{3.28}$$

We refrain from reporting the explicit expression for $\tilde{B}_k$, which can be derived by using the formulae given in eqs. (3.11) and (3.12).

3.5 The hard function

Following eq. (2.10) of ref. [31], the hard function can be expressed as the product

$$H_{k\bar{\ell}}(\Phi_0,\mu) = H_{k\bar{\ell}}(\Phi_0,\mu_{\rm H})\,U_{\rm H}\big(Q^2,\mu_{\rm H},\mu\big)\,. \tag{3.29}$$

The hard function $H_{k\bar{\ell}}(\Phi_0,\mu_{\rm H})$ evaluated at the hard scale $\mu_{\rm H}$ depends on the specific color-singlet production process that we are considering. It can be written as

$$H_{k\bar{\ell}}(\Phi_0,\mu_{\rm H}) = H_{k\bar{\ell}}^{(0)}(\Phi_0) + \frac{\alpha_{\rm S}(\mu_{\rm H})}{2\pi}\,H_{k\bar{\ell}}^{(1)}(\Phi_0,\mu_{\rm H}) + \mathcal{O}\big(\alpha_{\rm S}^2\big)\,, \tag{3.30}$$

where $H_{k\bar{\ell}}^{(0)}(\Phi_0)$ is the LO amplitude of the process and $H_{k\bar{\ell}}^{(n)}(\Phi_0,\mu_{\rm H})$ for $n > 0$ are its virtual corrections computed in the $\overline{\rm MS}$ subtraction scheme. The evolution kernel is given in eq. (2.11) of ref. [31] and reads

$$U_{\rm H}\big(Q^2,\mu_{\rm H},\mu\big) = \left|e^{K_{\rm H}(\mu_{\rm H},\mu)}\left(\frac{-Q^2-i0}{\mu_{\rm H}^2}\right)^{\eta_{\rm H}(\mu_{\rm H},\mu)}\right|^2, \tag{3.31}$$

where

$$K_{\rm H} = -2K_\Gamma + K_{\gamma_{\rm H}} \qquad\qquad \eta_{\rm H} = \eta_\Gamma. \tag{3.32}$$

The explicit expression for K_Γ, $K_{\gamma_{\rm H}}$ and η_Γ will be given in section 3.8.

3.6 The resummed cross section

At this point, we make the assumptions that

$$\mu_{\rm H}^2 = Q^2 \qquad\qquad \mu_{\rm B}^2 = Q\mu_{\rm S} \tag{3.33}$$

and introduce

$$\tilde{U}_0(s,Q,\mu_{\rm S},\mu) = U_{\rm H}\big(Q^2,\mu_{\rm H},\mu\big)\,\tilde{U}_{\rm B}^2\left(\frac{s}{Q},\mu_{\rm B},\mu\right)\tilde{U}_{\rm S}(s,\mu_{\rm S},\mu)\,, \tag{3.34}$$

so that, using eqs. (3.18), (3.27) and (3.29), we can further rewrite the factorization theorem as

$$\mathcal{L}\left\{\frac{d\sigma_{\rm res}}{d\Phi_0\, d\mathcal{T}_0}\right\} = \tilde{U}_0(s,Q,\mu_{\rm S},\mu)\sum_{k_a k_b} H_{k_a\bar{k}_b}(\Phi_0,\mu_{\rm H})\,\tilde{B}^a_{k_a}\left(\frac{s}{Q},x_a,\mu_{\rm B}\right) \times \tilde{B}^b_{\bar{k}_b}\left(\frac{s}{Q},x_b,\mu_{\rm B}\right)\tilde{S}_{k_a\bar{k}_b}(s,\mu_{\rm S})\,. \tag{3.35}$$

After defining

$$\eta = 2\eta_{\rm B} + \eta_{\rm S}, \tag{3.36}$$

the explicit expression for the evolution kernel reads

$$\tilde{U}_0(s,Q,\mu_{\rm S},\mu) = \exp(2K_{\rm H} + 2K_{\rm B} + K_{\rm S} - [\gamma + \log(\mu_{\rm S} s)]\,\eta)\,. \tag{3.37}$$

At this point, we can rewrite the Laplace transforms of eqs. (3.11) and (3.12) under the action of the above evolution kernel as derivatives with respect to the parameter η, so that they read

$$\tilde{U}_0(s,Q,\mu_{\rm S},\mu)\int_0^\infty dt\, e^{-s\mu_{\rm S} t}\,\mathcal{L}_0(t) = \frac{\partial}{\partial\eta}\,\tilde{U}_0(s,Q,\mu_{\rm S},\mu) \tag{3.38}$$

and

$$\tilde{U}_0(s,Q,\mu_{\rm S},\mu)\int_0^\infty dt\, e^{-s\mu_{\rm S} t}\,\mathcal{L}_1(t) = \frac{1}{2}\left(\frac{\partial^2}{\partial\eta^2} + \frac{\pi^2}{6}\right)\tilde{U}_0(s,Q,\mu_{\rm S},\mu)\,. \tag{3.39}$$

For example, the Laplace transform of the soft function given in eq. (3.20) under the action of the evolution kernel $\tilde{U}_0(s,Q,\mu_{\rm S},\mu)$ can be written equivalently as

$$\tilde{S}_{k\bar{\ell}}(s,\mu_{\rm S}) = \delta_{k\ell} + \frac{\alpha_{\rm S}}{2\pi}\,C_{k\ell}\left[-4\left(\frac{\partial^2}{\partial\eta^2} + \frac{\pi^2}{6}\right) + \frac{\pi^2}{6}\right] + \mathcal{O}\big(\alpha_{\rm S}^2\big)\,. \tag{3.40}$$

The advantage of this formulation is that the above expression does not depend anymore on s, which simplifies the inverse Laplace transform of the factorization theorem given in eq. (3.35). After applying the same procedure to the beam function, we are left with taking the inverse Laplace transform of the evolution kernel, which becomes

$$U_0(\mathcal{T}_0,Q,\mu_{\rm S},\mu) = \frac{1}{\mathcal{T}_0}\,\frac{\eta}{\Gamma(1+\eta)}\,\exp\left(2K_{\rm H} + 2K_{\rm B} + K_{\rm S} - \eta\left[\gamma + \log\left(\frac{\mu_{\rm S}}{\mathcal{T}_0}\right)\right]\right). \tag{3.41}$$

As an example, we can apply the η-derivative appearing in the Laplace transform of the soft function given in eq. (3.40) to the evolution kernel of eq. (3.41) to compute the NLL$'$ contribution of the soft function to the $\mathcal{T}_0$

spectrum of the resummed cross section, which becomes

$$\begin{aligned}
&\frac{d\sigma_{\text{res}}^{\text{soft}}}{d\Phi_0\, d\mathcal{T}_0} = \sum_k H^{(0)}_{k\bar{k}}(\Phi_0)\, f_k^a(x_a,\mu_{\text{B}})\, f_{\bar{k}}^b(x_b,\mu_{\text{B}}) \\
&\times \frac{1}{\mathcal{T}_0}\,\frac{\eta}{\Gamma(1+\eta)}\,\exp\!\left(2K_{\text{H}}+2K_{\text{B}}+K_{\text{S}}-\eta\left[\gamma+\log\!\left(\frac{\mu_{\text{S}}}{\mathcal{T}_0}\right)\right]\right) \\
&\times\left(1+\frac{\alpha_{\text{S}}(\mu_{\text{S}})}{2\pi}\,C_{kk}\left\{-4\left[\left(\psi^{(0)}(1+\eta)+\gamma+\log\!\left(\frac{\mu_{\text{S}}}{\mathcal{T}_0}\right)\right)^2-\psi^{(1)}(1+\eta)\right.\right.\right. \\
&\left.\left.\left.+\frac{\pi^2}{6}-\frac{2}{\eta}\left(\psi^{(0)}(1+\eta)+\gamma+\log\!\left(\frac{\mu_{\text{S}}}{\mathcal{T}_0}\right)\right)\right]+\frac{\pi^2}{6}\right\}+\mathcal{O}\big(\alpha_{\text{S}}^2\big)\right).
\end{aligned} \tag{3.42}$$

From the above equation, we can then compute the NLO contribution of the soft function to the resummed $\mathcal{T}_0$ cumulant to be

$$\begin{aligned}
&\int_0^{\mathcal{T}_0^{\text{cut}}} d\mathcal{T}_0\,\frac{d\sigma_{\text{res}}^{\text{soft}}}{d\Phi_0\, d\mathcal{T}_0} = \sum_k H^{(0)}_{k\bar{k}}(\Phi_0)\, f_k^a(x_a,\mu_{\text{B}})\, f_{\bar{k}}^b(x_b,\mu_{\text{B}}) \\
&\times \frac{1}{\Gamma(1+\eta)}\exp\!\left(2K_{\text{H}}+2K_{\text{B}}+K_{\text{S}}-\eta\left[\gamma+\log\!\left(\frac{\mu_{\text{S}}}{\mathcal{T}_0^{\text{cut}}}\right)\right]\right) \\
&\times\left(1+\frac{\alpha_{\text{S}}(\mu_{\text{S}})}{2\pi}\,C_{kk}\left\{-4\left[\left(\psi^{(0)}(1+\eta)+\gamma+\log\!\left(\frac{\mu_{\text{S}}}{\mathcal{T}_0^{\text{cut}}}\right)\right)^2\right.\right.\right. \\
&\left.\left.\left.-\psi^{(1)}(1+\eta)+\frac{\pi^2}{6}\right]+\frac{\pi^2}{6}\right\}+\mathcal{O}\big(\alpha_{\text{S}}^2\big)\right).
\end{aligned} \tag{3.43}$$

We will use this last equation in the next section to prove that the total cumulant of the resummed spectrum is equal to that of the resummed-expanded one (i.e. the $\mathcal{T}_0$ spectrum before the resummation).

3.7 The resummed-expanded cross section

The $\mathcal{T}_0$ spectrum of the differential cross section before the resummation can be simply obtained by directly substituting the expressions for the soft, beam and hard functions presented respectively in eqs. (3.14), (3.22 and (3.30) evaluated

at the resummation scale $\mu = Q$ in eq. (3.4), and at NLO reads

$$\begin{aligned}
\frac{d\sigma_{\rm RE}}{d\Phi_0\, d\mathcal{T}_0} &= \frac{1}{2}\sum_k H^{(0)}_{k\bar{k}}(\Phi_0)\, f^a_k(x_a,Q)\, f^b_{\bar{k}}(x_b,Q)\, \delta(\mathcal{T}_0) \\
&\quad + \frac{\alpha_{\rm S}(Q)}{2\pi\, Q}\sum_k \Bigg(H^{(0)}_{k\bar{k}}(\Phi_0) \left\{ f^a_k(x_a,Q)\, C_{kk} \left[-2\mathcal{L}_1\!\left(\frac{\mathcal{T}_0}{Q}\right) - \frac{\pi^2}{12}\,\delta\!\left(\frac{\mathcal{T}_0}{Q}\right)\right] \right. \\
&\quad + \sum_j \int_{x_a}^1 \frac{dz}{z}\, f^a_j\!\left(\frac{x_a}{z},Q\right) \left[\mathcal{L}_0\!\left(\frac{\mathcal{T}_0}{Q}\right)(1-z)\, P^{\rm AP}_{kj}(z)\, \mathcal{L}_0(1-z) \right. \\
&\quad \left. \left. + \delta\!\left(\frac{\mathcal{T}_0}{Q}\right) P^{\rm AP}_{kj}(z) \Big((1-z)\,\mathcal{L}_1(1-z) - \log z \Big) + \delta\!\left(\frac{\mathcal{T}_0}{Q}\right) P'_{kj}(z) \right] \right\} \\
&\quad \left. + \frac{1}{2} H^{(1)}_{k\bar{k}}(\Phi_0,Q)\, f^a_k(x_a,Q)\, \delta\!\left(\frac{\mathcal{T}_0}{Q}\right) \right) f^b_{\bar{k}}(x_b,Q) + (a \leftrightarrow b) + \mathcal{O}\big(\alpha_{\rm S}^2\big)\,.
\end{aligned} \tag{3.44}$$

Since

$$\int_0^{\mathcal{T}_0^{\rm cut}} d\mathcal{T}_0\, \mathcal{L}_n\!\left(\frac{\mathcal{T}_0}{Q}\right) = \frac{Q}{n+1}\, \log^{n+1}\!\left(\frac{\mathcal{T}_0^{\rm cut}}{Q}\right) \tag{3.45}$$

the NLO $\mathcal{T}_0$ cumulant becomes

$$\begin{aligned}
\frac{d\sigma_{\rm RE}}{d\Phi_0}(\mathcal{T}_0^{\rm cut}) &= \frac{1}{2}\sum_k H^{(0)}_{k\bar{k}}(\Phi_0)\, f^a_k(x_a,Q)\, f^b_{\bar{k}}(x_b,Q) \\
&\quad + \frac{\alpha_{\rm S}(Q)}{2\pi}\sum_k \Bigg(H^{(0)}_{k\bar{k}}(\Phi_0) \left\{ f^a_k(x_a,Q)\, C_{kk} \left[-\log^2\!\left(\frac{\mathcal{T}_0^{\rm cut}}{Q}\right) - \frac{\pi^2}{12}\right] \right. \\
&\quad + \sum_j \int_{x_a}^1 \frac{dz}{z} f^a_j\!\left(\frac{x_a}{z},Q\right) \left[\log\!\left(\frac{\mathcal{T}_0^{\rm cut}}{Q}\right)(1-z)\, P^{\rm AP}_{kj}(z)\, \mathcal{L}_0(1-z) \right. \\
&\quad \left. \left. + P^{\rm AP}_{kj}(z) \Big((1-z)\,\mathcal{L}_1(1-z) - \log z \Big) + P'_{kj}(z) \right] \right\} \\
&\quad \left. + \frac{1}{2} H^{(1)}_{k\bar{k}}(\Phi_0,Q)\, f^a_k(x_a,Q) \right) f^b_{\bar{k}}(x_b,Q) + (a \leftrightarrow b) + \mathcal{O}\big(\alpha_{\rm S}^2\big)\,.
\end{aligned} \tag{3.46}$$

We now want to show that the total cumulant (i.e. the cumulant up to the maximum kinematically allowed value of zero-jettiness $\mathcal{T}_0^{\rm max}$ for the configuration Φ_0) of the resummed-expanded contribution equals that of the resummed contribution. Since we have only computed the resummed cumulant of the soft function, we need to do the same for the resummed-expanded one. In the approximation where beam and hard functions are treated at LO, the resummed-

expanded cumulant reads

$$\frac{d\sigma^{\rm soft}_{\rm RE}}{d\Phi_0}(\mathcal{T}_0^{\rm cut}) = \sum_k H^{(0)}_{k\bar{k}}(\Phi_0)\, f^a_k(x_a,Q)\, f^b_{\bar{k}}(x_b,Q) \times \left\{1 + \frac{\alpha_{\rm S}(Q)}{2\pi}\, C_{kk} \left[-4\log^2\left(\frac{\mathcal{T}_0^{\rm cut}}{Q}\right) + \frac{\pi^2}{6}\right] + \mathcal{O}\big(\alpha_{\rm S}^2\big)\right\}. \tag{3.47}$$

Under the assumption that the soft scale becomes equal to the fixed-order scale Q for the maximum kinematically allowed value of $\mathcal{T}_0$

$$\mu_{\rm S}(\mathcal{T}_0^{\rm max}) = Q, \tag{3.48}$$

since

$$\psi^{(0)}(1) = -\gamma \qquad\qquad \psi^{(1)}(1) = \frac{\pi^2}{6}, \tag{3.49}$$

from eq. (3.43) the total resummed cumulant of the soft function reads

$$\frac{d\sigma^{\rm soft}_{\rm res}}{d\Phi_0}(\mathcal{T}_0^{\rm max}) = \sum_k H^{(0)}_{k\bar{k}}(\Phi_0)\, f^a_k(x_a,Q)\, f^b_{\bar{k}}(x_b,Q) \times \left\{1 + \frac{\alpha_{\rm S}(Q)}{2\pi}\, C_{kk} \left[-4\log^2\left(\frac{\mathcal{T}_0^{\rm max}}{Q}\right) + \frac{\pi^2}{6}\right] + \mathcal{O}\big(\alpha_{\rm S}^2\big)\right\}, \tag{3.50}$$

which is exactly equal to the total resummed-expanded cumulant presented in eq. (3.47).

3.8 Some SCET parameters

We finally report here the explicit expressions for K_Γ, η_Γ and K_γ, which are given in eq. (D.13) of ref. [30] or equivalently in eq. (B.16) of ref. [31] and read

$$K_\Gamma(\mu_0,\mu) = -\frac{\Gamma_0}{4\beta_0^2}\left[\frac{4\pi}{\alpha_{\rm S}(\mu_0)}\left(1-\frac{1}{r}-\log r\right) + \left(\frac{\Gamma_1}{\Gamma_0}-\frac{\beta_1}{\beta_0}\right)(1-r+\log r) + \frac{\beta_1}{2\beta_0}\log^2 r\right] + \mathcal{O}(\alpha_{\rm S}) \tag{3.51}$$

$$\eta_\Gamma(\mu_0,\mu) = -\frac{\Gamma_0}{2\beta_0}\left[\log r + \frac{\alpha_{\rm S}(\mu_0)}{4\pi}\left(\frac{\Gamma_1}{\Gamma_0}-\frac{\beta_1}{\beta_0}\right)(r-1)\right] + \mathcal{O}\big(\alpha_{\rm S}^2\big) \tag{3.52}$$

$$K_\gamma(\mu_0,\mu) = -\frac{\gamma_0}{2\beta_0}\log r + \mathcal{O}(\alpha_{\rm S})\,, \tag{3.53}$$

where

$$r = \frac{\alpha_{\rm S}(\mu)}{\alpha_{\rm S}(\mu_0)}, \tag{3.54}$$

and, from eqs. (D.15) of ref. [30],

$$\begin{aligned}\beta_0 &= \frac{11}{3}\,C_{\rm A} - \frac{4}{3}\,T_{\rm F} n_{\rm f} \\ \beta_1 &= \frac{34}{3}\,C_{\rm A}^2 - \left(\frac{20}{3} C_{\rm A} + 4 C_{\rm F}\right) T_{\rm F} n_{\rm f}.\end{aligned} \tag{3.55}$$

Finally, from eqs. (D.16-D.18) of ref. [30], in the case of quark-induced processes

$$\begin{aligned}\Gamma_0 &= 4 C_{\rm F} \\ \Gamma_1 &= 4 C_{\rm F} \left[\left(\frac{67}{9} - \frac{\pi^2}{3}\right) C_{\rm A} - \frac{20}{9} T_{\rm F} n_{\rm f}\right],\end{aligned} \tag{3.56}$$

and

$$\gamma_{\rm S_0} = 0 \qquad \gamma_{\rm B_0} = 6 C_{\rm F} \qquad \gamma_{\rm H_0} = -6 C_{\rm F}, \tag{3.57}$$

while, from eqs. (B.19-B.21) of ref. [31], in the case of gluon-induced processes

$$\begin{aligned}\Gamma_0 &= 4 C_{\rm A} \\ \Gamma_1 &= 4 C_{\rm A} \left[\left(\frac{67}{9} - \frac{\pi^2}{3}\right) C_{\rm A} - \frac{20}{9} T_{\rm F} n_{\rm f}\right],\end{aligned} \tag{3.58}$$

and

$$\gamma_{\rm S_0} = 0 \qquad \gamma_{\rm B_0} = 2\beta_0 \qquad \gamma_{\rm H_0} = -2\beta_0. \tag{3.59}$$

Chapter 4

The Geneva Monte Carlo differential cross section

4.1 The phase space mappings

Any event generator that aims to a QCD accuracy beyond leading order (LO) needs to rely on mappings between phase spaces with different number of final-state partons. If we call $d\Phi_0$, $d\Phi_1$, and $d\Phi_2$ the phase spaces with 0, 1, and 2 final-state partons respectively, for a NNLO event generator we need to introduce a mapping from $d\Phi_1$ to $d\Phi_0$, and one from $d\Phi_2$ to $d\Phi_1$. The composition of the two mappings gives the mapping from $d\Phi_2$ to $d\Phi_0$.

Such mappings allow us to define finite differential cross sections beyond LO. In particular, we can write

$$\begin{aligned}\frac{d\sigma^{\text{NNLO}}_{\geq 0}}{d\Phi_0} &= B_0(\Phi_0) + V_0(\Phi_0) + W_0(\Phi_0) \\ &\quad + \int \frac{d\Phi_1}{d\Phi_0}\left(B_1(\Phi_1) + V_1(\Phi_1) + \int \frac{d\Phi_2}{d\Phi_1} B_2(\Phi_2)\right) \qquad (4.1)\\ \frac{d\sigma^{\text{NLO}}_{\geq 1}}{d\Phi_1} &= B_1(\Phi_1) + V_1(\Phi_1) + \int \frac{d\Phi_2}{d\Phi_1} B_2(\Phi_2) \qquad (4.2)\\ \frac{d\sigma^{\text{LO}}_{\geq 2}}{d\Phi_2} &= B_2(\Phi_2)\,. \qquad (4.3)\end{aligned}$$

In the expressions above, we exploited the possibility of writing the phase space $d\Phi_{N+1}$ with $N+1$ partons as the product of the projected phase space $d\Phi_N$ with N partons times a radiation phase space. The expression $\int d\Phi_{N+1}/d\Phi_N$ denotes an integral over the radiation phase space of $d\Phi_{N+1}$ limited to the Φ_{N+1} configurations which are projected onto Φ_N by the $N+1 \to N$ mapping. The differential cross section of eq. (4.1) then contains all the contributions from the Φ_0 configurations, and those from the Φ_1 and Φ_2 configurations that are projectable onto $d\Phi_0$, which gives it NNLO accuracy. The differential cross section

of eq. (4.2) contains instead all the contributions from the Φ_1 configurations, and those from the Φ_2 configurations that are projectable onto $d\Phi_1$, which gives it NLO accuracy. Finally, the differential cross section of eq. (4.3) contains all the contributions from the Φ_2 configurations, which gives it LO accuracy.

In general, not all the points of Φ_{N+1} can be mapped to a valid Φ_N configuration, which makes it useful to classify the Φ_1 and Φ_2 configurations into two sets: the projectable, which can be mapped to a configuration with one parton less, and non-projectable ones, which cannot. Since all the configurations that are close to an infrared limit need to be projectable (otherwise the mapping would not be infrared safe), the non-projectable configurations are free from QCD singularities. We can then write the integrated NNLO cross section for the production of a color singlet as

$$\sigma_{\text{CS}}^{\text{NNLO}} = \int d\Phi_0 \, \frac{d\sigma_{\geq 0}^{\text{NNLO}}}{d\Phi_0} + \int d\Phi_1 \, \frac{d\sigma_{\geq 1,\text{nonproj}}^{\text{NLO}}}{d\Phi_1} + \int d\Phi_2 \, \frac{d\sigma_{\geq 2,\text{nonproj}}^{\text{LO}}}{d\Phi_2}, \tag{4.4}$$

where we have introduced the label *nonproj* to indicate that the integral is limited to the non-projectable configurations.

4.2 The zero-jettiness spectrum

The goal of GENEVA is to generate partonic events at NNLO in QCD matching the NNLL′ resummed $\mathcal{T}_0$ spectrum with the fixed-order contributions. To present the formula for the matching, we first need to introduce the fixed-order spectrum, which from eq. (4.1) can be written as

$$\frac{d\sigma_{\geq 0}^{\text{NNLO}}}{d\Phi_0 \, d\mathcal{T}_0} = \left[B_0(\Phi_0) + V_0(\Phi_0) + W_0(\Phi_0)\right] \delta(\mathcal{T}_0) + \int \frac{d\Phi_1}{d\Phi_0 \, d\mathcal{T}_0} \frac{d\sigma_1^{\text{NLO}}}{d\Phi_1}, \tag{4.5}$$

and the non-singular spectrum

$$\frac{d\sigma_{\text{nonsing}}^{\text{NLO}_1}}{d\Phi_0 \, d\mathcal{T}_0} = \frac{d\sigma_{\geq 0}^{\text{NNLO}}}{d\Phi_0 \, d\mathcal{T}_0} - \left.\frac{d\sigma_{\text{res}}^{\text{NNLL}'}}{d\Phi_0 \, d\mathcal{T}_0}\right|_{\text{NNLO}}, \tag{4.6}$$

defined as the difference between the fixed-order and the NNLO expansion in the strong coupling of the resummed spectra. Since the terms at order α_{S}^0 cancel in the above difference, we refer to the accuracy of the non-singular spectrum as NLO_1 (instead of NNLO): with the subscript 1 we indicate that the contribution has an α_{S} expansion that begins one order higher with respect to the Born cross section of the process.

Under the assumption that the total cumulant (i.e. the integral over all the kinematically allowed values of $\mathcal{T}_0$) of the NNLL′ resummed spectrum and its NNLO expansion are equal, we can write

$$\int_0^{\mathcal{T}_0^{\text{max}}} d\mathcal{T}_0 \, \frac{d\sigma_{\text{nonsing}}^{\text{NLO}_1}}{d\Phi_0 \, d\mathcal{T}_0} = \frac{d\sigma_{\geq 0}^{\text{NNLO}}}{d\Phi_0} - \int_0^{\mathcal{T}_0^{\text{max}}} d\mathcal{T}_0 \, \frac{d\sigma_{\text{res}}^{\text{NNLL}'}}{d\Phi_0 \, d\mathcal{T}_0}, \tag{4.7}$$

where $\mathcal{T}_0^{\max}$ is the maximum kinematically allowed value of $\mathcal{T}_0$ for the given Φ_0 configuration. From now on we will denote the $\mathcal{T}_0$ cumulants with the upper integration limit between parenthesis, so that the above formula can be equivalently rewritten as

$$\frac{d\sigma^{\mathrm{NLO_1}}_{\mathrm{nonsing}}}{d\Phi_0}(\mathcal{T}_0^{\max}) = \frac{d\sigma^{\mathrm{NNLO}}_{\geq 0}}{d\Phi_0} - \frac{d\sigma^{\mathrm{NNLL'}}_{\mathrm{res}}}{d\Phi_0}(\mathcal{T}_0^{\max})\,. \tag{4.8}$$

By inverting the above equations, we can write the NNLO differential cross section of eq. (4.1) as

$$\frac{d\sigma^{\mathrm{NNLO}}_{\geq 0}}{d\Phi_0} = \int_0^{\mathcal{T}_0^{\max}} d\mathcal{T}_0 \left(\frac{d\sigma^{\mathrm{NNLL'}}_{\mathrm{res}}}{d\Phi_0\, d\mathcal{T}_0} + \frac{d\sigma^{\mathrm{NLO_1}}_{\mathrm{nonsing}}}{d\Phi_0\, d\mathcal{T}_0} \right). \tag{4.9}$$

The above is the master formula for the matching between the resummation and the fixed-order calculation, and allows to generate events with a NNLL$'$ accurate $\mathcal{T}_0$ spectrum without spoiling the NNLO accuracy of the distributions that are inclusive over the radiation.

4.3 The splitting functions

The resummed spectrum appearing in eqs. (4.6) and (4.9) cannot be directly used to generate events with one parton, since it does not have a full dependence on the $d\Phi_1$ phase space. For this reason we need to introduce the concept of splitting functions.

In general, a splitting function $P_{N\to N+1}(\Phi_{N+1})$ is a function defined on the phase space with one extra parton $d\Phi_{N+1}$ such that, for every function $f(\Phi_N, \mathcal{T}_N)$

$$\int \frac{d\Phi_{N+1}}{d\Phi_N}\, f(\Phi_N, \mathcal{T}_N)\, P_{N\to N+1}(\Phi_{N+1}) = \int d\mathcal{T}_N\, f(\Phi_N, \mathcal{T}_N)\,. \tag{4.10}$$

In other words the splitting function provides the dependence on the extra variables that make the $\mathcal{T}_N$ spectrum differential over $d\Phi_{N+1}$ without spoiling the distributions that depend only on Φ_N and $\mathcal{T}_N$.

In our case we can define the NNLL$'$ resummed contribution differential over $d\Phi_1$ as the product between the $\mathcal{T}_0$ spectrum and the $0 \to 1$ splitting function

$$\frac{d\sigma^{\mathrm{NNLL'}}_{\mathrm{res}}}{d\Phi_1} = \frac{d\sigma^{\mathrm{NNLL'}}_{\mathrm{res}}}{d\Phi_0\, d\mathcal{T}_0}\, P_{0\to 1}(\Phi_1)\,. \tag{4.11}$$

4.4 0-jet exclusive and 1-jet inclusive cross sections

The formula presented in eq. (4.9) cannot be directly implemented in a Monte Carlo event generator, unless a $\mathrm{NLO_1}$ local cancellation of the infrared divergences appearing in the two terms of eq. (4.6) is provided.

Since that is not currently available in GENEVA, we need to introduce a resolution parameter $\mathcal{T}_0^{\rm cut}$ and divide the NNLO cross section into a 0-jet exclusive and a 1-jet inclusive contributions. The 0-jet exclusive cross section describes events without resolved final-state partons, and its expression is given by the cumulant of the $\mathcal{T}_0$ distribution up to the resolution parameter $\mathcal{T}_0^{\rm cut}$

$$\frac{d\sigma_0^{\rm MC}}{d\Phi_0}(\mathcal{T}_0^{\rm cut}) = \frac{d\sigma_{\rm res}^{\rm NNLL'}}{d\Phi_0}(\mathcal{T}_0^{\rm cut}) + \frac{d\sigma_{\rm nonsing}^{\rm NLO_1}}{d\Phi_0}(\mathcal{T}_0^{\rm cut})\,. \tag{4.12}$$

In most implementations of color-singlet production processes within GENEVA, $\mathcal{T}_0^{\rm cut}$ is chosen to be of the order of 1 GeV. The 1-jet inclusive cross section instead describes events with at least one resolved final-state parton. Its expression is given by the sum of the contributions coming from the projectable Φ_1 configurations, whose spectrum is described by eq. (4.9), and the non-projectable ones

$$\frac{d\sigma_{\geq 1}^{\rm MC}}{d\Phi_1} = \left(\frac{d\sigma_{\rm res}^{\rm NNLL'}}{d\Phi_1} + \frac{d\sigma_{\rm nonsing}^{\rm NLO_1}}{d\Phi_1}\right)\theta(\mathcal{T}_0 - \mathcal{T}_0^{\rm cut}) + \frac{d\sigma_{\geq 1,\rm nonproj}^{\rm NLO}}{d\Phi_1}, \tag{4.13}$$

where we have implicitly used the splitting function $P_{0\to 1}(\Phi_1)$ to provide the Φ_1 dependence to the resummed spectrum, as described in eq. (4.11). From the sum the 0-jet exclusive and the 1-jet inclusive contributions, upon integration over the radiation phase space of Φ_1, we recover the NNLO differential cross section of eq. (4.9)

$$\frac{d\sigma_0^{\rm MC}}{d\Phi_0}(\mathcal{T}_0^{\rm cut}) + \int \frac{d\Phi_1}{d\Phi_0}\,\frac{d\sigma_{\geq 1}^{\rm MC}}{d\Phi_1} = \frac{d\sigma_{\geq 0}^{\rm NNLO}}{d\Phi_0}. \tag{4.14}$$

The third and final contribution to the total cross section is given by the non-projectable Φ_2 configurations

$$\frac{d\sigma_{\geq 2,\rm nonproj}^{\rm MC}}{d\Phi_2} = \frac{d\sigma_{\geq 2,\rm nonproj}^{\rm LO}}{d\Phi_2}, \tag{4.15}$$

so that, similarly to what we did in eq. (4.4), we can write the total cross section for the production of a color singlet as

$$\sigma_{\rm CS}^{\rm NNLO} = \int d\Phi_0\,\frac{d\sigma_0^{\rm MC}}{d\Phi_0} + \int d\Phi_1\,\frac{d\sigma_{\geq 1}^{\rm MC}}{d\Phi_1} + \int d\Phi_2\,\frac{d\sigma_{\geq 2,\rm nonproj}^{\rm MC}}{d\Phi_2}. \tag{4.16}$$

4.4.1 Approximation of the non-singular cumulant

The formula presented in eq. (4.12) could be directly implemented in GENEVA only if a NNLO local subtraction of the infrared divergences were available.

Since that is not the case, we need to approximate the $\rm NLO_1$ non-singular cumulant with the $\rm LO_1$ one, and rewrite the 0-jet exclusive differential cross section of eq. (4.12) as

$$\frac{d\sigma_0^{\rm MC}}{d\Phi_0}(\mathcal{T}_0^{\rm cut}) = \frac{d\sigma_{\rm res}^{\rm NNLL'}}{d\Phi_0}(\mathcal{T}_0^{\rm cut}) + \frac{d\sigma_{\rm nonsing}^{\rm LO_1}}{d\Phi_0}(\mathcal{T}_0^{\rm cut})\,. \tag{4.17}$$

Since the non-singular spectrum is integrable up to $\mathcal{T}_0 = 0$, the missing contributions are power corrections in $\mathcal{T}_0^{\rm cut}$ (which means that they become smaller as $\mathcal{T}_0^{\rm cut}$ becomes smaller). The choice of the value of $\mathcal{T}_0^{\rm cut}$ will then be dictated by a compromise between minimizing the power corrections coming from the above approximation and maximizing the stability of the integration of the inclusive 1-jet cross section, where the cancellation of the logarithmically enhanced contributions is not fully local.

As we did for the 0-jet exclusive cross section, we also neglect the $\alpha_{\rm s}^2$ contributions below $\mathcal{T}_0^{\rm cut}$ appearing in the 1-jet inclusive cross section of eq. (4.13), which becomes

$$\begin{aligned}\frac{d\sigma_{\geq 1}^{\rm MC}}{d\Phi_1} = &\left(\frac{d\sigma_{\rm res}^{\rm NNLL'}}{d\Phi_1} + \frac{d\sigma_{\rm nonsing}^{\rm NLO_1}}{d\Phi_1} + \frac{d\sigma_{\geq 1,\rm nonproj}^{\rm NLO}}{d\Phi_1}\right)\theta(\mathcal{T}_0 - \mathcal{T}_0^{\rm cut}) \\ &+ \frac{d\sigma_{\geq 1,\rm nonproj}^{\rm LO}}{d\Phi_1}\,\theta(\mathcal{T}_0^{\rm cut} - \mathcal{T}_0)\,, \end{aligned} \tag{4.18}$$

and in the non-projectable contributions of eq. (4.15), which become

$$\frac{d\sigma_{\geq 2,\rm nonproj}^{\rm MC}}{d\Phi_2} = \frac{d\sigma_{\geq 2,\rm nonproj}^{\rm LO}}{d\Phi_2}\,\theta(\mathcal{T}_0 - \mathcal{T}_0^{\rm cut})\,. \tag{4.19}$$

Since the value of the NNLO total cross section for the processes under study can be independently obtained from publicly available fixed-order calculations, after the events have been generated, we can furthermore perform a reweight of those with no final-state partons to recover the contributions lost in the above approximation. By choosing appropriately the value of $\mathcal{T}_0^{\rm cut}$, the total size of the missing contributions can be reduced below 1% of the total cross section.

4.5 1-jet exclusive and 2-jet inclusive cross sections

The next step is to introduce a second resolution parameter $\mathcal{T}_1^{\rm cut}$ to distinguish between events with 1 and 2 resolved final-state partons, and divide the 1-jet inclusive cross section given in eq. (4.18) into a 1-jet exclusive and a 2-jet inclusive contributions, with the goals of

1. Performing the $\mathcal{T}_1$ resummation.

2. Preserving the 1-jet inclusive differential cross section

$$\frac{d\sigma_1^{\rm MC}}{d\Phi_1}(\mathcal{T}_1^{\rm cut}) + \int \frac{d\Phi_2}{d\Phi_1}\,\frac{d\sigma_{\geq 2}^{\rm MC}}{d\Phi_2} = \frac{d\sigma_{\geq 1}^{\rm MC}}{d\Phi_1}. \tag{4.20}$$

3. Giving pointwise NLO accuracy to the 1-jet exclusive cross section and LO accuracy to the 2-jet inclusive cross section.

We follow a multiplicative approach and, after calling $U_1(\Phi_1, \mathcal{T}_1^{\rm cut})$ the one-jettiness Sudakov form factor and $U_1^{(1)}(\Phi_1, \mathcal{T}_1^{\rm cut})$ its first order $\alpha_{\rm s}$ expansion, we write the exclusive 1-jet cross section as

$$\begin{aligned}\frac{d\sigma_1^{\rm MC}}{d\Phi_1}(\mathcal{T}_1^{\rm cut}) = \Bigg\{ & \frac{d\sigma_{\geq 1}^{\rm MC}}{d\Phi_1} U_1\left(\Phi_1, \mathcal{T}_1^{\rm cut}\right) - \frac{d\sigma_{\geq 1}^{\rm LO}}{d\Phi_1} U_1^{(1)}(\Phi_1, \mathcal{T}_1^{\rm cut}) \\ & - \int \frac{d\Phi_2}{d\Phi_1} \frac{d\sigma_{\geq 2,\rm proj}^{\rm LO}}{d\Phi_2} \theta(\mathcal{T}_1 - \mathcal{T}_1^{\rm cut}) \Bigg\} \theta(\mathcal{T}_0 - \mathcal{T}_0^{\rm cut}) \\ & + \frac{d\sigma_{\geq 1,\rm nonproj}^{\rm LO}}{d\Phi_1} \theta(\mathcal{T}_0^{\rm cut} - \mathcal{T}_0)\,. \end{aligned} \tag{4.21}$$

After calling $U_1'(\Phi_1, \mathcal{T}_1)$ the derivative of the Sudakov form factor with respect to $\mathcal{T}_1$, and $U_1^{(1)\prime}(\Phi_1, \mathcal{T}_1)$ its first order expansion in the strong coupling, we can instead write the contribution to the inclusive 2-jet cross section from a projectable Φ_2 configuration as

$$\begin{aligned}\frac{d\sigma_{\geq 2}^{\rm MC}}{d\Phi_2} = \Bigg\{ & \left[\frac{d\sigma_{\geq 1}^{\rm MC}}{d\Phi_1} U_1'\left(\Phi_1, \mathcal{T}_1\right) - \frac{d\sigma_{\geq 1}^{\rm LO}}{d\Phi_1} U_1^{(1)\prime}(\Phi_1, \mathcal{T}_1)\right] P_{1\to 2}(\Phi_2) \\ & + \frac{d\sigma_{\geq 2,\rm proj}^{\rm LO}}{d\Phi_2} \Bigg\} \theta(\mathcal{T}_1 - \mathcal{T}_1^{\rm cut})\, \theta(\mathcal{T}_0 - \mathcal{T}_0^{\rm cut}) \\ & + \frac{d\sigma_{\geq 2,\rm nonproj}^{\rm LO}}{d\Phi_2} \theta(\mathcal{T}_0 - \mathcal{T}_0^{\rm cut})\,, \end{aligned} \tag{4.22}$$

where $P_{1\to 2}(\Phi_2)$ is the $1 \to 2$ splitting function, and satisfy the relation given in eq. (4.10) with $N = 1$.

It can be seen that the above definitions for the 1-jet exclusive and 2-jet inclusive contributions preserve the 1-jet inclusive differential cross section, as stated in eq. (4.20). Furthermore, expanding eqs. (4.21) and (4.22) with respect to the strong coupling, we obtain

$$\begin{aligned}\frac{d\sigma_1^{\rm MC}}{d\Phi_1}(\mathcal{T}_1^{\rm cut}) = & \left[\frac{d\sigma_{\geq 1}^{\rm NLO}}{d\Phi_1} - \int \frac{d\Phi_2}{d\Phi_1} \frac{d\sigma_{\geq 2,\rm proj}^{\rm LO}}{d\Phi_2} \theta(\mathcal{T}_1 - \mathcal{T}_1^{\rm cut})\right] \theta(\mathcal{T}_0 - \mathcal{T}_0^{\rm cut}) \\ & + \frac{d\sigma_{\geq 1,\rm nonproj}^{\rm LO}}{d\Phi_1} \theta(\mathcal{T}_0^{\rm cut} - \mathcal{T}_0) + \mathcal{O}\big(\alpha_{\rm s}^3\big)\,, \end{aligned} \tag{4.23}$$

and

$$\frac{d\sigma_{\geq 2}^{\rm MC}}{d\Phi_2} = \left[\frac{d\sigma_{\geq 2,\rm proj}^{\rm LO}}{d\Phi_2} \theta(\mathcal{T}_1 - \mathcal{T}_1^{\rm cut}) + \frac{d\sigma_{\geq 2,\rm nonproj}^{\rm LO}}{d\Phi_2}\right] \theta(\mathcal{T}_0 - \mathcal{T}_0^{\rm cut}) + \mathcal{O}\big(\alpha_{\rm s}^3\big)\,, \tag{4.24}$$

which show that the 1-jet exclusive differential cross section has NLO accuracy for $\mathcal{T}_0 > \mathcal{T}_0^{\rm cut}$ and LO accuracy for $\mathcal{T}_0 < \mathcal{T}_0^{\rm cut}$, and the 2-jet inclusive differential cross section has LO accuracy for $\mathcal{T}_0 > \mathcal{T}_0^{\rm cut}$.

4.5.1 Approximation of the 1-jet inclusive cross section

The computation of the 1-jet inclusive differential cross section appearing in the formulae of eqs. (4.21) and (4.22) can become significantly time consuming from the computational point of view, since in the fixed-order contribution it requires a NLO_1 calculation to be performed for every Φ_1 or Φ_2 configuration generated by the Monte Carlo integrator.

To avoid that, when computing the 1-jet inclusive cross section, we approximate the matrix elements of the configurations with two final-state partons with their infrared limit. In the formulae, we label the contributions computed under this approximation with a C subscript. To compensate for this approximation, we need to add back the difference between the exact and the approximated 1-jet inclusive cross section

$$\int \frac{d\Phi_2}{d\Phi_1}\left[\frac{d\sigma^{\mathrm{LO}}_{\geq 2,\mathrm{proj}}}{d\Phi_2} - \frac{d\sigma^{\mathrm{LO}}_{\geq 2,C,\mathrm{proj}}}{d\Phi_2}\right]\theta(\mathcal{T}_0 - \mathcal{T}_0^{\mathrm{cut}})\,, \tag{4.25}$$

which allows us to approximate the 1-jet exclusive differential cross section of eq. (4.21) as

$$\begin{aligned}\frac{d\sigma^{\mathrm{MC}}_1}{d\Phi_1}(\mathcal{T}_1^{\mathrm{cut}}) = \Bigg\{ &\frac{d\sigma^{\mathrm{MC}}_{\geq 1,C}}{d\Phi_1}\,U_1\left(\Phi_1,\mathcal{T}_1^{\mathrm{cut}}\right) - \frac{d\sigma^{\mathrm{LO}}_{\geq 1}}{d\Phi_1}\,U_1^{(1)}(\Phi_1,\mathcal{T}_1^{\mathrm{cut}}) \\ &+ \int \frac{d\Phi_2}{d\Phi_1}\left[\frac{d\sigma^{\mathrm{LO}}_{\geq 2,\mathrm{proj}}}{d\Phi_2}\,\theta(\mathcal{T}_1^{\mathrm{cut}} - \mathcal{T}_1) - \frac{d\sigma^{\mathrm{LO}}_{\geq 2,C,\mathrm{proj}}}{d\Phi_2}\right]\Bigg\}\theta(\mathcal{T}_0 - \mathcal{T}_0^{\mathrm{cut}}) \\ &+ \frac{d\sigma^{\mathrm{LO}}_{\geq 1,\mathrm{nonproj}}}{d\Phi_1}\,\theta(\mathcal{T}_0^{\mathrm{cut}} - \mathcal{T}_0)\,,\end{aligned} \tag{4.26}$$

and the 2-jet inclusive differential cross section of eq. (4.22) as

$$\begin{aligned}\frac{d\sigma^{\mathrm{MC}}_{\geq 2}}{d\Phi_2} = \Bigg\{ &\left[\frac{d\sigma^{\mathrm{MC}}_{\geq 1,C}}{d\Phi_1}\,U_1'\left(\Phi_1,\mathcal{T}_1\right) - \frac{d\sigma^{\mathrm{LO}}_{\geq 1}}{d\Phi_1}\,U_1^{(1)\prime}(\Phi_1,\mathcal{T}_1)\right]P_{1\to 2}(\Phi_2) \\ &+ \frac{d\sigma^{\mathrm{LO}}_{\geq 2,\mathrm{proj}}}{d\Phi_2}\Bigg\}\,\theta(\mathcal{T}_1 - \mathcal{T}_1^{\mathrm{cut}})\,\theta(\mathcal{T}_0 - \mathcal{T}_0^{\mathrm{cut}}) \\ &+ \frac{d\sigma^{\mathrm{LO}}_{\geq 2,\mathrm{nonproj}}}{d\Phi_2}\,\theta(\mathcal{T}_0 - \mathcal{T}_0^{\mathrm{cut}})\,.\end{aligned} \tag{4.27}$$

We highlight that, after this approximation, the conditions given in eqs. (4.20), (4.23) and 4.24 are still satisfied.

4.6 The parton shower

After generating the two hardest emissions with GENEVA, we have to pass the events to a parton shower. Ideally, we would like to use a shower strongly

ordered in N-jettiness, such that, if we call $\mathcal{T}_{N-1}$ the $(N-1)$-jettiness after N emissions, and $\mathcal{T}_N$ the N-jettiness after $N+1$ emissions

$$\mathcal{T}_N \ll \mathcal{T}_{N-1}. \tag{4.28}$$

In this case, the $(N+1)$-th emission of the shower (on top of a Φ_N configuration with N final-state partons) would be distributed according to

$$\begin{aligned} S_{N+1} &= U_N(\Lambda, \mathcal{T}_N^{\max}) \\ &\quad + \frac{d\Phi_{N+1}}{d\Phi_N}\, U'_N(\mathcal{T}_N, \mathcal{T}_N^{\max})\, P_{N\to N+1}(\Phi_{N+1})\, \theta(\mathcal{T}_N - \Lambda)\, \theta(\mathcal{T}_N^{\max} - \mathcal{T}_N)\,, \end{aligned} \tag{4.29}$$

where U_N is the Sudakov form factor, U'_N its derivative with respect to $\mathcal{T}_N$, Λ the shower cutoff, $\mathcal{T}_N^{\max} \sim \mathcal{T}_{N-1}$ the maximum allowed value for $\mathcal{T}_N$, and $P_{N\to N+1}$ the splitting function used to make the event differential on Φ_{N+1}, such that

$$\begin{aligned} &\int \frac{d\Phi_{N+1}}{d\Phi_N}\, U'_N(\mathcal{T}_N, \mathcal{T}_N^{\max})\, P_{N\to N+1}(\Phi_{N+1})\, \theta(\mathcal{T}_N - \Lambda)\, \theta(\mathcal{T}_N^{\max} - \mathcal{T}_N) \\ &= \int_\Lambda^{\mathcal{T}_N^{\max}} d\mathcal{T}_N\, U'_N(\mathcal{T}_N, \mathcal{T}_N^{\max}) = U_N(\mathcal{T}_N^{\max}, \mathcal{T}_N^{\max}) - U_N(\Lambda, \mathcal{T}_N^{\max})\,. \end{aligned} \tag{4.30}$$

We can immediately notice that, as long as $U_N(\mathcal{T}_N^{\max}, \mathcal{T}_N^{\max}) = 1$, the emission is unitary.

Since $\mathcal{T}_N$-ordered parton showers are not currently available, we instead combine GENEVA with the PYTHIA8 parton shower, which is ordered in the transverse momentum. To do that, we still need to guarantee that there is no double counting, i.e. the hardest emission generated by the shower has

$$\mathcal{T}_2 < \mathcal{T}_1^{\text{allowed}}, \tag{4.31}$$

where $\mathcal{T}_1^{\text{allowed}}$ is the one-jettiness of the hard event computed after discarding the expressions of $\mathcal{T}_1$ that do not select a valid QCD clustering. However, since the PYTHIA8 parton shower is not ordered in N-jettiness, the first emission is not always the one with the highest $\mathcal{T}_N$. Since the ideal parton shower that we are trying to reproduce is strongly ordered in $\mathcal{T}_N$ we can assume that the $\mathcal{T}_2$ of the final event with all the emissions is similar to the would-be $\mathcal{T}_2$ after three emissions of a $\mathcal{T}_N$-ordered parton shower. In this way we can impose the veto given in eq. (4.31) after all the emissions have been generated.

Events generated by GENEVA with no final-state partons are distributed according to the $\mathcal{T}_0$ cumulant of the cross section up to $\mathcal{T}_0^{\text{cut}}$ (see eq. (4.17)), so, after the shower, they must keep

$$\mathcal{T}_0 < \mathcal{T}_0^{\text{cut}}. \tag{4.32}$$

Furthermore, if the parton shower adds them one single emission, the resulting configuration Φ_1 must be projectable on the original configuration Φ_0. Similarly, events generated by GENEVA with up to one final-state partons are distributed

according to the $\mathcal{T}_1$ cumulant of the cross section up to $\mathcal{T}_1^{\text{cut}}$ (see eq. (4.26)), so, after the shower, they must keep

$$\mathcal{T}_1 < \mathcal{T}_1^{\text{cut}}. \tag{4.33}$$

Furthermore, if the parton shower adds them one single emission, the resulting configuration Φ_2 must be projectable on the original configuration Φ_1.

We are now left with fixing the starting scale of the parton shower. In an ideal parton shower ordered in N-jettiness the starting scale $\mathcal{T}_N^{\text{hard}}$ for events with N final-state partons would be $\mathcal{T}_0^{\text{cut}}$, $\mathcal{T}_1^{\text{cut}}$ and $\mathcal{T}_1^{\text{allowed}}$ for events with 0, 1 and 2 final-state partons, respectively. In a p_{T}-ordered parton shower instead it must be the maximum allowed value for the transverse momentum p_{T} of the hardest emission provided by the shower such that $\mathcal{T}_N < \mathcal{T}_N^{\text{hard}}$. Calling p the momentum of such an emission and assuming that $\mathcal{T}_N = \hat{p}_0 - \hat{p}_3$, since

$$p_{\text{T}} = \sqrt{\hat{p}_0^2 - \hat{p}_3^2} = \sqrt{\mathcal{T}_N \left(\hat{p}_0 + \hat{p}_3\right)} \leq \sqrt{\mathcal{T}_N \sqrt{s}} < \sqrt{\mathcal{T}_N^{\text{hard}} \sqrt{s}}, \tag{4.34}$$

if we start the shower from the scale $\sqrt{\mathcal{T}_N^{\text{hard}} \sqrt{s}}$ we are covering the entire phase space.

Finally, we have to deal with the case of processes where the maximum number of final-state partons generated by GENEVA is one, instead of two. In this case the veto to apply to events with one final-state partons becomes

$$\mathcal{T}_1 < \mathcal{T}_0^{\text{allowed}}. \tag{4.35}$$

4.6.1 The first emission generated by the parton shower

The preservation of the NNLL$'$ partonic spectrum by the parton shower relies on the assumption that for events generated by GENEVA with $N \geq 1$ final-state partons, the zero-jettiness $\mathcal{T}_0$ computed at partonic level is spoiled by the shower by an amount of order

$$\mathcal{T}_N \ll \mathcal{T}_0. \tag{4.36}$$

Such variation is typically small enough for events with two final-state partons, for which

$$\mathcal{T}_2 \ll \mathcal{T}_1^{\text{allowed}} \ll \mathcal{T}_0, \tag{4.37}$$

but could lead to significant numerical deviations for events generated with a single final-state parton. In this case, we provide manually the generation of the first shower emission, using a (quasi) $\mathcal{T}_0$-preserving mapping (see sections 7 and A). Such emission is distributed according to eq. (4.29), with $N = 1$, $\Lambda < \mathcal{T}_1^{\text{cut}}$ and $\mathcal{T}_1^{\text{max}} = \mathcal{T}_0$.

Chapter 5

The splitting functions

To provide an explicit expression for the $N \to N+1$ splitting function $P_{N\to N+1}$, we need to write the subset of the phase space $d\Phi_{N+1}$ with $N+1$ final-state partons projectable onto the underlying phase space $d\Phi_N$ with N final-state partons as a product of $d\Phi_N$ times three radiation variables, one of which needs to be the N-jettiness $\mathcal{T}_N$ and the other two we will call z and ϕ. In this way the integral over the projectable $d\Phi_{N+1}$ phase space at fixed Φ_N and $\mathcal{T}_N$, can be written as

$$\int \frac{d\Phi_{N+1}}{d\Phi_N\, d\mathcal{T}_N} = \sum_{k=1}^{N+2} \int_{z^k_{\min}(\Phi_N,\mathcal{T}_N)}^{z^k_{\max}(\Phi_N,\mathcal{T}_N)} dz\, J_k(\Phi_N,\mathcal{T}_N,z) \int_{\phi^k_{\min}(\Phi_N,\mathcal{T}_N,z)}^{\phi^k_{\max}(\Phi_N,\mathcal{T}_N,z)} d\phi, \quad (5.1)$$

where the index k runs over the $N+2$ possible emitter partons (that in the following we will call mothers) of the Φ_N configuration, and we have made the only assumption that the Jacobian

$$J_k(\Phi_N,\mathcal{T}_N,z) = \left.\frac{d\Phi_{N+1}}{d\Phi_N\, d\mathcal{T}_N\, dz\, d\phi}\right|_k \quad (5.2)$$

does not depend on ϕ. As we will see, this is true for the cases we are interested in for this work (i.e. $P_{0\to1}$ and $P_{1\to2}$). We introduce here the names *ISRA* (initial-state radiation A), *ISRB* (initial-state radiation B), and *FSR* (final-state radiation), to indicate the three possible mothers we will have to deal with: the parton from the first and second beam, and the final-state parton, respectively. We furthermore label *ISRA* and *ISRB* collectively as *ISR*. The integral over the $d\Phi_{N+1}$ phase space summed over the n_{real} signatures (in the following we will call signature the set of particles of a configuration) with $N+1$

final-state partons can now be written as

$$\sum_{\beta=1}^{n_{\rm real}} \int d\Phi_{N+1} = \sum_{\beta=1}^{n_{\rm real}} \int_{\text{unprojectable } \Phi_{N+1}} d\Phi_{N+1} + \sum_{\alpha=1}^{n_{\rm Born}} \int d\Phi_N \int d\mathcal{T}_N \sum_{k=1}^{N+2} \int_{z^k_{\rm min}(\Phi_N,\mathcal{T}_N)}^{z^k_{\rm max}(\Phi_N,\mathcal{T}_N)} dz\, J_k(\Phi_N,\mathcal{T}_N,z) \int_{\phi^k_{\rm min}(\Phi_N,\mathcal{T}_N,z)}^{\phi^k_{\rm max}(\Phi_N,\mathcal{T}_N,z)} d\phi \sum_{j=1}^{n^k_{\rm split}}, \tag{5.3}$$

where $n_{\rm Born}$ is the number of signatures with N final-state partons, and $n^k_{\rm split}$ the number of possible QCD splittings of the parton k. The unprojectable Φ_{N+1} configurations are those for which the two closest partons do not represent a valid QCD splitting, or the Φ_N configurations obtained from the projection is not kinematically allowed or it is not a valid Φ_N signature.

The splitting function $P_{N\to N+1}(\Phi_{N+1})$ has to be identically null in the unprojectable regions of $d\Phi_{N+1}$, and satisfy the equation

$$\sum_{k=1}^{N+2} \int_{z^k_{\rm min}(\Phi_N,\mathcal{T}_N)}^{z^k_{\rm max}(\Phi_N,\mathcal{T}_N)} dz\, J_k(\Phi_N,\mathcal{T}_N,z) \int_{\phi^k_{\rm min}(\Phi_N,\mathcal{T}_N,z)}^{\phi^k_{\rm max}(\Phi_N,\mathcal{T}_N,z)} d\phi \sum_{j=1}^{n^k_{\rm split}} P_{N\to N+1}(\Phi_{N+1}) = 1. \tag{5.4}$$

We choose to define it such that in the projectable regions of $d\Phi_{N+1}$

$$P_{N\to N+1}(\Phi_{N+1}) = \frac{f_{kj}(\Phi_N,\mathcal{T}_N,z,\phi)}{\sum_{k'=1}^{N+2} \int_{z^{k'}_{\rm min}(\Phi_N,\mathcal{T}_N)}^{z^{k'}_{\rm max}(\Phi_N,\mathcal{T}_N)} dz' J_{k'}(\Phi_N,\mathcal{T}_N,z') \int_{\phi^{k'}_{\rm min}(\Phi_N,\mathcal{T}_N,z')}^{\phi^{k'}_{\rm max}(\Phi_N,\mathcal{T}_N,z')} d\phi' \sum_{j'=1}^{n^{k'}_{\rm split}} f_{k'j'}(\Phi_N,\mathcal{T}_N,z',\phi')} \tag{5.5}$$

where $f_{kj}(\Phi_N,\mathcal{T}_N,z,\phi)$ could be in principle a fully generic function. If we assume that f_{kj} does not depend on ϕ (this is true for the expressions of f_{kj} discussed in this work), we can simplify the above equation to

$$P_{N\to N+1}(\Phi_{N+1}) = \frac{f_{kj}(\Phi_N,\mathcal{T}_N,z)}{\sum_{k'=1}^{N+2} \int_{z^{k'}_{\rm min}(\Phi_N,\mathcal{T}_N)}^{z^{k'}_{\rm max}(\Phi_N,\mathcal{T}_N)} dz'\, J_{k'}(\Phi_N,\mathcal{T}_N,z')\, I^{k'}_{\phi}(\Phi_N,\mathcal{T}_N,z') \sum_{j'=1}^{n^{k'}_{\rm split}} f_{k'j'}(\Phi_N,\mathcal{T}_N,z')}, \tag{5.6}$$

where

$$I^k_{\phi}(\Phi_N,\mathcal{T}_N,z) = \phi^k_{\rm max}(\Phi_N,\mathcal{T}_N,z) - \phi^k_{\rm min}(\Phi_N,\mathcal{T}_N,z)\,. \tag{5.7}$$

In section 5.1 we will discuss the explicit expressions that we use for f_{kj}.

In the most recent version of GENEVA it has been introduced the possibility of evaluating the splitting functions on-the-fly, performing the integral at the

denominator of eq. (5.6) for every Φ_{N+1} configuration generated. To do this, we need to compute, both for the $1 \to 0$ and $2 \to 1$ mappings, the integration limits on z and ϕ and the Jacobian $J_k(\Phi_N, \mathcal{T}_N, z)$. We highlight that, whenever the constraints on z and ϕ are in the form of an inequality involving both the variables, computing analytically the integration limits on z is not necessary, since they can be imposed on-the-fly setting to zero the integrand function whenever the range of integration for ϕ is empty.

5.1 Altarelli–Parisi splitting functions

All the observables that can be written as a function of the N-jettiness $\mathcal{T}_N$ and the variables of $d\Phi_{N+1}$ preserved by the $N+1 \to N$ mapping do not depend on the particular expression of the splitting function $P_{N\to N+1}$ as long as it fulfills the normalization condition of eq. (5.4). This is true because every bin of the distribution will contain all the z and ϕ allowed points for the given Φ_N and $\mathcal{T}_N$. All the other distributions will instead be sensitive to $P_{N\to N+1}$. In particular, such a choice can affect significantly the efficiency of the Monte Carlo event generator in the region of small $\mathcal{T}_N$, where the cancellation between the logarithmically enhanced terms appearing in the fixed-order and the resummed expanded contributions happens. For this reason the main criterion we follow in the choice of the actual expression to use for the splitting functions is to provide the most accurate possible infrared limit, which leads us to defining the f_{kj} functions appearing in eq. (5.5) as

$$f_{kj}(\Phi_N, \mathcal{T}_N, z, \phi) = \begin{cases} \alpha_{\text{S}}(\mu_{\text{R}})\, f_j^a(x_a, \mu_{\text{F}})\, f_{\bar{p}_b}^b(x_b, \mu_{\text{F}})\, z\, P_{kj}^{\text{AP}}(z) & \text{if } k \text{ is } \textit{ISRA} \\ \alpha_{\text{S}}(\mu_{\text{R}})\, f_{\bar{p}_a}^a(x_a, \mu_{\text{F}})\, f_j^b(x_b, \mu_{\text{F}})\, z\, P_{kj}^{\text{AP}}(z) & \text{if } k \text{ is } \textit{ISRB} \\ \alpha_{\text{S}}(\mu_{\text{R}})\, f_{\bar{p}_a}^a(x_a, \mu_{\text{F}})\, f_{\bar{p}_b}^b(x_b, \mu_{\text{F}})\, P_{jk}^{\text{AP}}(z) & \text{if } k \text{ is } \textit{FSR}, \end{cases} \tag{5.8}$$

where $\bar{p}_a$ and $\bar{p}_b$ are the initial-state partons of the underlying signature, $\alpha_{\text{S}}(\mu_{\text{R}})$ is the strong coupling evaluated at the renormalization scale μ_{R}, $f_p^h(x_h, \mu_{\text{F}})$ is the PDF of the parton p in the hadron h evaluated at the momentum fraction x_h and factorization scale μ_{F}, and P_{kj}^{AP} are the Altarelli–Parisi splitting functions given in eq. (3.24). The renormalization and factorization scales are set to

$$\mu_{\text{R}} = \mu_{\text{F}} = m_{\text{CS}}. \tag{5.9}$$

We highlight that in the definition of the splitting functions provided in eq. 5.8 we chose to evaluate the PDFs at the actual fraction of momenta carried by the incoming partons in the configuration Φ_{N+1}, instead of its collinear limit. This allows to provide a better description of the tail of distributions like the transverse momentum of the color singlet $p_{\text{T,CS}}$. In the $0 \to 1$ splitting presented in chapter 6, the expression of $p_{\text{T,CS}}$ in terms of the Φ_0, $\mathcal{T}_0$ and z variables is given by

$$p_{\text{T,CS}}^2 = m_{\text{CS}} \mathcal{T}_0 \frac{1-z}{z}. \tag{5.10}$$

From this definition it can be seen that Φ_1 configurations with small values of z can have a large $p_{\mathrm{T,CS}}$ despite having a small $\mathcal{T}_0$. Such configurations, despite belonging to the tail of the $p_{\mathrm{T,CS}}$ distribution, receive contributions from the resummed terms, and thus depend on the explicit expressions used for the splitting functions.

Chapter 6

The $1 \to 0$ mapping

6.1 Definition of the mapping and zero-jettiness

We consider the process of production of a color singlet (that decays into n particles) in association with one parton. In the laboratory frame, we call P_a and P_b the momenta of the incoming beams, x_a and x_b the fraction of such momenta that undergo the hard process, q_i and m_i for i from 1 to n the momenta and masses of the particles that compose the color singlet, and p_1 the momentum of the final-state parton. The $1 \to 0$ mapping is defined such that

1. It preserves the mass m_{CS} of the color singlet.
2. It preserves the rapidity y_{CS} of the color singlet.
3. It does not change the momenta of the decay products in the center-of-mass frame of the color singlet.

It can be seen that the above conditions uniquely identify the mapping.

The zero-jettiness $\mathcal{T}_0$ of the process can be written as

$$\mathcal{T}_0 = \min\left(\hat{p}_1^+, \hat{p}_1^-\right). \tag{6.1}$$

We can assume without loss of generality that

$$\hat{p}_1^+ < \hat{p}_1^-, \tag{6.2}$$

so that

$$\mathcal{T}_0 = \hat{p}_1^+. \tag{6.3}$$

If this is not the case, the results presented below still hold after exchanging the labels of the beams.

6.2 Phase space

The phase space for the process reads

$$d\Phi_1 = dx_a\, dx_b \prod_{i=1}^{n} \frac{d^4q_i}{(2\pi)^3}\, \delta\big(q_i^2 - m_i^2\big)\, \theta\big(q_i^0\big)\, \frac{d^4p_1}{(2\pi)^3}\, \delta\big(p_1^2\big)\, \theta\big(p_1^0\big) \\ \times (2\pi)^4\, \delta^4\left(\sum_{i=1}^{n} q_i + p_1 - x_a P_a - x_b P_b\right). \tag{6.4}$$

After calling q the momentum of the color singlet (i.e. the sum of the momenta of its decay products), we multiply the above expression by

$$\frac{dm_{\text{CS}}^2}{2\pi} \frac{d^4q}{(2\pi)^3}\, \delta\big(q^2 - m_{\text{CS}}^2\big)\, \theta\big(q^0\big)\, (2\pi)^4\, \delta^4\left(\sum_{i=1}^{n} q_i - q\right) = 1, \tag{6.5}$$

so that we can rewrite the phase space as

$$d\Phi_1 = dx_a\, dx_b\, \frac{dm_{\text{CS}}^2}{2\pi}\, \frac{d^4q}{(2\pi)^3}\, \delta\big(q^2 - m_{\text{CS}}^2\big)\, \theta\big(q^0\big)\, \frac{d^4p_1}{(2\pi)^3}\, \delta\big(p_1^2\big)\, \theta\big(p_1^0\big) \\ \times (2\pi)^4\, \delta^4(q + p_1 - x_a P_a - x_b P_b)\, d\Phi_{\text{CS}}\big(m_{\text{CS}}^2\big), \tag{6.6}$$

with

$$d\Phi_{\text{CS}}\big(m_{\text{CS}}^2\big) = \prod_{i=1}^{n} \frac{d^4q_i}{(2\pi)^3}\, \delta\big(q_i^2 - m_i^2\big)\, \theta\big(q_i^0\big)\, (2\pi)^4\, \delta^4\left(\sum_{i=1}^{n} q_i - q\right). \tag{6.7}$$

At this point we can call

$$d\Phi_{\text{rad}} = \frac{dm_{\text{CS}}^2}{2\pi}\, \frac{d^4q}{(2\pi)^3}\, \delta\big(q^2 - m_{\text{CS}}^2\big)\, \theta\big(q^0\big)\, \frac{d^4p_1}{(2\pi)^3}\, \delta\big(p_1^2\big)\, \theta\big(p_1^0\big) \\ \times (2\pi)^4\, \delta^4(q + p_1 - x_a P_a - x_b P_b) = \frac{dm_{\text{CS}}^2}{2\pi} \left(1 - \frac{m_{\text{CS}}^2}{s}\right) \frac{d\cos\theta\, d\phi}{32\pi^2}, \tag{6.8}$$

where $s = (x_a\, P_a + x_b P_b)^2$ and θ and ϕ are the polar angles of p_1 in the partonic center-of-mass frame. If we introduce

$$\xi = 1 - \frac{m_{\text{CS}}^2}{s} \tag{6.9}$$

$$y = \cos\theta, \tag{6.10}$$

we can finally write

$$d\Phi_{\text{rad}} = \frac{s}{64\pi^3}\, \xi\, d\xi\, dy\, d\phi, \tag{6.11}$$

and

$$d\Phi_1 = \frac{S x_a x_b \xi}{64\pi^3}\, dx_a\, dx_b\, d\xi\, dy\, d\phi\, d\Phi_{\text{CS}}, \tag{6.12}$$

where we called $S = (P_a + P_b)^2$.

We have chosen to write the phase space in terms of the variables x_a, x_b, ξ, y, and ϕ because their integration limits are constant

$$x_a, x_b, \xi \in (0,1) \qquad y \in (-1,1) \qquad \phi \in (0, 2\pi)\,. \tag{6.13}$$

However, at this point our goal is to rewrite $d\Phi_1$ using the new variables m_{CS}, y_{CS}, $\mathcal{T}_0$, and

$$z = \frac{m_{\text{CS}}}{m_{\text{CS}} + \hat{p}_1^-}. \tag{6.14}$$

After writing them in terms of the old variables

$$\begin{cases} m_{\text{CS}} = \sqrt{S x_a x_b\,(1-\xi)} \\ y_{\text{CS}} = \dfrac{1}{2}\left[\log\left(\dfrac{x_a}{x_b}\right) + \log\left(\dfrac{2-\xi\,(1+y)}{2-\xi\,(1-y)}\right)\right] \\ \mathcal{T}_0 = \dfrac{\sqrt{S x_a x_b}}{2}\,\xi\,(1-y)\sqrt{\dfrac{2-\xi\,(1+y)}{2-\xi\,(1-y)}} \\ z = \dfrac{1}{1 + \dfrac{\xi\,(1+y)}{2\sqrt{1-\xi}}\sqrt{\dfrac{2-\xi\,(1-y)}{2-\xi\,(1+y)}}}, \end{cases} \tag{6.15}$$

and computing the Jacobian matrix we can write

$$d\Phi_1 = \frac{m_{\text{CS}}}{32\pi^3\, S\, z^2}\, dm_{\text{CS}}^2\, dy_{\text{CS}}\, d\mathcal{T}_0\, dz\, d\phi\, d\Phi_{\text{CS}}\big(m_{\text{CS}}^2\big)\,. \tag{6.16}$$

Since

$$d\Phi_0 = \frac{dm_{\text{CS}}^2\, dy_{\text{CS}}}{S}\, d\Phi_{\text{CS}}\big(m_{\text{CS}}^2\big) \tag{6.17}$$

we finally arrive to

$$d\Phi_1 = \frac{m_{\text{CS}}}{32\pi^3\, z^2}\, d\Phi_0\, d\mathcal{T}_0\, dz\, d\phi. \tag{6.18}$$

6.3 Integration limits

The last objects needed to compute the integral at the denominator of the splitting functions are the integration limits on z and ϕ at fixed Φ_0 and $\mathcal{T}_0$. Since we already know from eq. (6.13) that

$$\phi \in (0, 2\pi)\,, \tag{6.19}$$

we are left with deriving the integration limits on z.

To simplify the expressions in the rest of this section, we introduce the three auxiliary variables

$$\alpha = \frac{\mathcal{T}_0}{m_{\rm CS}} = \frac{\xi\,(1-y)}{2\sqrt{1-\xi}}\sqrt{\frac{2-\xi\,(1+y)}{2-\xi\,(1-y)}} \tag{6.20}$$

$$\beta = \frac{1-z}{z} = \frac{\xi\,(1+y)}{2\sqrt{1-\xi}}\sqrt{\frac{2-\xi\,(1-y)}{2-\xi\,(1+y)}}, \tag{6.21}$$

and

$$\kappa = \frac{\sqrt{S}}{m_{\rm CS}}. \tag{6.22}$$

From their definition and the integration limits on ξ and y provided in eq. (6.13) we can immediately see that they are both positive in the range of integration. Furthermore, the condition given in eq. (6.2) imposes that

$$0 < \alpha < \beta. \tag{6.23}$$

At this point we can write the old variables x_a, x_b, ξ, and y in terms of κ, $y_{\rm CS}$, α, and β as follows

$$\begin{cases} x_a = \dfrac{e^{y_{\rm CS}}}{\kappa}\left(\beta + \sqrt{1+\alpha\beta}\right) \\ x_b = \dfrac{e^{-y_{\rm CS}}}{\kappa}\left(\alpha + \sqrt{1+\alpha\beta}\right) \\ \xi = \dfrac{-\alpha\beta\,(\beta-\alpha)^2 - \left(\alpha^2+\beta^2\right) + (\alpha+\beta)\sqrt{1+\alpha\beta}}{(1+\alpha\beta-\alpha^2)\,(1+\alpha\beta-\beta^2)} \\ y = \dfrac{(\beta-\alpha)\sqrt{1+\alpha\beta}\left(\alpha-\sqrt{1+\alpha\beta}\right)\left(\beta-\sqrt{1+\alpha\beta}\right)}{-\alpha\beta\,(\beta-\alpha)^2 - (\alpha^2+\beta^2) + (\alpha+\beta)\sqrt{1+\alpha\beta}}, \end{cases} \tag{6.24}$$

and derive the integration limits on the new variables κ, $y_{\rm CS}$, α, and β from those on x_a, x_b, ξ, and y provided in eq. (6.13). It can be immediately seen that, under the condition given in eq. 6.23, the requirements that $\xi \in (0,1)$, $y \in (-1,1)$, $x_a > 0$, and $x_b > 0$ are automatically satisfied. We are then left with asking that $x_a < 1$ and $x_b < 1$, which is equivalent to imposing

$$\begin{cases} \beta + \sqrt{1+\alpha\beta} < \kappa e^{-y_{\rm CS}} \\ \alpha + \sqrt{1+\alpha\beta} < \kappa e^{y_{\rm CS}}. \end{cases} \tag{6.25}$$

At fixed κ, $y_{\rm CS}$, and α, the solutions to the above inequalities with respect to β impose that

$$\begin{cases} \beta < \beta_1 = \kappa e^{-y_{\rm CS}} + \dfrac{\alpha}{2} - \sqrt{1 + \kappa\alpha e^{-y_{\rm CS}} + \left(\dfrac{\alpha}{2}\right)^2} \\ \beta < \beta_2 = \dfrac{1}{\alpha}\left[\left(\kappa e^{y_{\rm CS}} - \alpha\right)^2 - 1\right]. \end{cases} \tag{6.26}$$

Putting the above solutions together with the original condition of eq. (6.23), we obtain the constraints on β

$$\alpha < \beta < \min(\beta_1, \beta_2)\,, \tag{6.27}$$

from which we can extract the integration limits of z

$$\frac{1}{1+\min(\beta_1,\beta_2)} < z < \frac{1}{1+\alpha}. \tag{6.28}$$

The phase space with one final-state parton is simple enough to allow us to compute analytically the integration limits for all the variables. From the constraints given in eq. (6.25), it can be seen that

$$0 < m_{\rm CS} < \sqrt{S} \qquad\qquad -\log\frac{\sqrt{S}}{m_{\rm CS}} < y_{\rm CS} < \log\frac{\sqrt{S}}{m_{\rm CS}}, \tag{6.29}$$

and, at fixed Φ_0,

$$0 < \mathcal{T}_0 < \frac{\sqrt{S}}{2} e^{-|y_{\rm CS}|} - \frac{m_{\rm CS}^2}{2\sqrt{S}} e^{|y_{\rm CS}|}. \tag{6.30}$$

Chapter 7

The $2 \to 1$ mapping

We consider a configuration Φ_2 that describes the process of production of a color singlet (that decays into n particles) in association with two partons. In the laboratory frame, we call P_a and P_b the momenta of the incoming beams, x_a and x_b the fractions of such momenta that undergo the hard process, q_i and m_i for i from 1 to n the momenta and masses of the particles that are produced from the decay of the color singlet, and p_1 and p_2 the momenta of the two final-state partons. Our goal is to define a mapping that projects Φ_2 onto an underlying configuration Φ_1 with one final-state parton. For such configuration, in the laboratory frame we call $\bar{x}_a$ and $\bar{x}_b$ the fractions of momenta of the incoming beams that undergo the hard process, $\bar{q}_i$ for i from 1 to n the momenta and masses of the particles that are produced from the decay of the color singlet, and $\bar{p}_1$ the momentum of the only final-state parton. In general, the mapping does not need to be defined throughout the entire $d\Phi_2$ phase space, but its existence is mandatory in the singular regions of $d\Phi_2$, where the condition of infrared safety dictates that the underlying configuration is obtained by clustering together the two collinear partons or removing the soft one.

7.1 One-jettiness

In the $d\Phi_2$ phase space the one-jettiness is defined as

$$\mathcal{T}_1 = \sum_{i=1}^{2} \min_n \left(\hat{p}_i^+, \hat{p}_i^-, \hat{p}_i \cdot n \right), \tag{7.1}$$

where n can be any lightlike vector with $n^0 = 1$. We distinguish between two possible cases.

1. *FSR*: There exists at least one vector n such that for both the final-state partons the expression in the sum of eq. (7.1) is minimized by $\hat{p}_i \cdot n$, in which case
$$\mathcal{T}_1 = \min_n ((\hat{p}_1 + \hat{p}_2) \cdot n) = \hat{p}_{12}^0 - \left| \vec{\hat{p}}_{12} \right|, \tag{7.2}$$

where we have introduced

$$p_{12} = p_1 + p_2. \tag{7.3}$$

2. *ISR*: At least for one of the two final-state partons the expression in the sum of eq. (7.1) is minimized by $\hat{p}_i^+$ or $\hat{p}_i^-$. In this case we can always choose n to be parallel to the other momentum, so that

$$\mathcal{T}_1 = \min\left(\hat{p}_1^+, \hat{p}_1^-, \hat{p}_2^+, \hat{p}_2^-\right). \tag{7.4}$$

Since up to now we have never distinguished between the two final-state partons, we can limit ourselves to studying the case where

$$\mathcal{T}_1 = \min\left(\hat{p}_2^+, \hat{p}_2^-\right). \tag{7.5}$$

If that is not the case, all the formulae derived in the following will still hold after exchanging the labels of the two final-state partons. From now on, we will call hardest the parton with momentum p_1 and softest the one with momentum p_2. We are then left with two possible cases.

(a) *ISRA*: In this case

$$\mathcal{T}_1 = \hat{p}_2^+. \tag{7.6}$$

(b) *ISRB*: In this case

$$\mathcal{T}_1 = \hat{p}_2^-. \tag{7.7}$$

We will only present the formulae for the *ISRA* case, since those for the *ISRB* one can simply be obtained from a parity transformation.

7.2 Fully recursive zero-jettiness

We have seen how the expression for the one-jettiness can be used to measure which couple of partons in the Φ_2 configuration is the closest to an infrared limit. This allows us to introduce the fully recursive zero-jettiness $\mathcal{T}_0^{\text{FR}}$, which differs from the exact zero-jettiness $\mathcal{T}_0$ since it is computed after clustering together the two closest partons if the emission belongs to the *FSR* class. In other words, in the *ISR* case $\mathcal{T}_0^{\text{FR}}$ has the same definition of $\mathcal{T}_0$ which, from eq. (3.1) can be expressed as

$$\mathcal{T}_0 = \min\left(\hat{p}_1^+ + \hat{p}_2^+, \hat{p}_1^+ + \hat{p}_2^-, \hat{p}_1^- + \hat{p}_2^+, \hat{p}_1^- + \hat{p}_2^-\right), \tag{7.8}$$

while in the *FSR* case $\mathcal{T}_0^{\text{FR}}$ has to be computed on a Φ_1 configuration with a single final-state parton of momentum p_{12}, so that

$$\mathcal{T}_0^{\text{FR}} = \min\left(\hat{p}_{12}^+, \hat{p}_{12}^-\right). \tag{7.9}$$

Ideally, we would like to use a $2 \to 1$ mapping that preserves the exact $\mathcal{T}_0$. However, due to the complicated expression of such a parameter, we limit ourselves to preserving $\mathcal{T}_0^{\text{FR}}$, since it has the same singular structure of $\mathcal{T}_0$.

In the *ISR* case $\mathcal{T}_0^{\text{FR}} = \mathcal{T}_0$, whose expression is given in eq. (7.8), and we need to impose that it is equal to the zero-jettiness computed on the projected Φ_1 configuration, which, from eq. (6.1), reads

$$\mathcal{T}_0 = \min\left(\hat{\bar{p}}_1^+, \hat{\bar{p}}_1^-\right). \tag{7.10}$$

We distinguish among four possible cases.

1. *Same Hemisphere ISRA*: In this case both $\hat{p}_1$ and $\hat{p}_2$ are in the hemisphere of the first beam, so that

$$\mathcal{T}_0^{\text{FR}} = \hat{p}_1^+ + \hat{p}_2^+ \qquad\qquad \mathcal{T}_1 = \hat{p}_2^+. \tag{7.11}$$

   The condition of infrared safety imposes that, in the limit of small $\mathcal{T}_1$, $\hat{p}_1$ approaches $\hat{\bar{p}}_1$, which imposes that the projected Φ_1 configuration must have

$$\mathcal{T}_0 = \hat{\bar{p}}_1^+. \tag{7.12}$$

2. *Opposite Hemisphere ISRA*: In this case $\hat{p}_1$ is in the hemisphere of the second beam, while $\hat{p}_2$ is in that of the first beam, so that

$$\mathcal{T}_0^{\text{FR}} = \hat{p}_1^- + \hat{p}_2^+ \qquad\qquad \mathcal{T}_1 = \hat{p}_2^+. \tag{7.13}$$

   The condition of infrared safety imposes that the projected Φ_1 configuration must have

$$\mathcal{T}_0 = \hat{\bar{p}}_1^-. \tag{7.14}$$

3. *Same Hemisphere ISRB*: In this case both $\hat{p}_1$ and $\hat{p}_2$ are in the hemisphere of the second beam, so that

$$\mathcal{T}_0^{\text{FR}} = \hat{p}_1^- + \hat{p}_2^- \qquad\qquad \mathcal{T}_1 = \hat{p}_2^-. \tag{7.15}$$

   The condition of infrared safety imposes that the projected Φ_1 configuration must have

$$\mathcal{T}_0 = \hat{\bar{p}}_1^-. \tag{7.16}$$

4. *Opposite Hemisphere ISRB*: In this case $\hat{p}_1$ is in the hemisphere of the first beam, while $\hat{p}_2$ is in that of the second beam, so that

$$\mathcal{T}_0^{\text{FR}} = \hat{p}_1^+ + \hat{p}_2^- \qquad\qquad \mathcal{T}_1 = \hat{p}_2^-. \tag{7.17}$$

   The condition of infrared safety imposes that the projected Φ_1 configuration must have

$$\mathcal{T}_0 = \hat{\bar{p}}_1^+. \tag{7.18}$$

In the *FSR* case instead we need to impose that the zero-jettiness given in eq. (7.10) computed on the projected Φ_1 configuration is equal to the fully-recursive zero-jettiness of eq. (7.9). We distinguish between two possible cases.

1. *FSRA*: In this case

$$\mathcal{T}_0^{\text{FR}} = \hat{p}_{12}^{+} \qquad \mathcal{T}_1 = \hat{p}_{12}^{0} - \left|\vec{\hat{p}}_{12}\right|. \tag{7.19}$$

   The condition of infrared safety imposes that, in the limit of small $\mathcal{T}_1$, $\hat{p}_{12}$ approaches $\hat{\bar{p}}_1$, which imposes that the projected Φ_1 configuration must have

$$\mathcal{T}_0 = \hat{\bar{p}}_1^{+}. \tag{7.20}$$

2. *FSRB*: In this case

$$\mathcal{T}_0^{\text{FR}} = \hat{p}_{12}^{-} \qquad \mathcal{T}_1 = \hat{p}_{12}^{0} - \left|\vec{\hat{p}}_{12}\right|. \tag{7.21}$$

   The condition of infrared safety imposes that the projected Φ_1 configuration must have

$$\mathcal{T}_0 = \hat{\bar{p}}_1^{-}. \tag{7.22}$$

We will only present the formulae for the *FSRA* case, since those for the *FSRB* one can simply be obtained from a parity transformation.

As can be seen from the equations above, the difference between $\mathcal{T}_0$ and $\mathcal{T}_0^{\text{FR}}$ arises only in the case where the two closest partons are the two final-state ones (*FSR* case) and, despite being the closest, their momenta are in different hemispheres, so that the expression for the exact zero-jettiness is given by $\min\left(\hat{p}_1^{+} + \hat{p}_2^{-}, \hat{p}_1^{-} + \hat{p}_2^{+}\right)$, which is different from that for the fully recursive zero-jettiness of eq. (7.9).

7.3 Direct mapping

The $2 \to 1$ mapping used in GENEVA is defined under the conditions that it preserves

1. The mass m_{CS} of the color singlet.
2. The rapidity y_{CS} of the color singlet.
3. The fully recursive zero-jettiness $\mathcal{T}_0^{\text{FR}}$.
4. The momenta q_i of the particles belonging to the color singlet in its center-of-mass frame.

The remaining two conditions needed to uniquely identify the mapping are chosen differently between the *ISR* and *FSR* cases.

1. *ISR*: We require that

$$\frac{\bar{p}_1^{+}}{\bar{p}_1^{-}} = \frac{p_1^{+}}{p_1^{-}}, \tag{7.23}$$

   and the azimuthal angle of the hard parton is preserved

$$\bar{\Phi}_1 = \Phi_1. \tag{7.24}$$

2. *FSR*: We require that

$$\bar{p}_1^- \bar{p}_1^+ = p_{12}^- p_{12}^+, \tag{7.25}$$

and the azimuthal angle of the color singlet is preserved

$$\bar{\Phi}_1 = \Phi_{12}. \tag{7.26}$$

The condition presented in eq. (7.25) ensures that in the *FSR* case both the possible expressions for $\mathcal{T}_0^{\text{FR}}$ (presented in eqs. (7.19) and (7.21) are preserved, which allows us to use the same mapping for both the *FSRA* and *FSRB* cases. The motivations behind the condition presented in eq. (7.23) are instead more subtle, and are discussed in section (A.5) of the appendix.

The 5 different expressions for $\mathcal{T}_1$ presented in eqs. (7.2) and (7.4) divide the phase space into 5 different regions (two *ISRA*, two *ISRB*, and one *FSR*). Each of the regions still admits two possible expressions for $\mathcal{T}_0^{\text{FR}}$ as discussed in section 7.2, which takes the total number of required different expressions for the mapping to 10. However, as explained in section 7.1, among the four possible *ISR* regions we will limit ourselves to studying the *ISRA* one where the softest parton has momentum p_2, since the formulae for the other three can be extracted from those for the first one through simple manipulations. We further notice that the condition presented in eq. (7.25) ensures that both the possible expression for $\mathcal{T}_0^{\text{FR}}$ in the *FSR* case are preserved, which makes the *FSRA* and *FSRB* mappings equivalent. In the following we then present the explicit expressions for the mapping in the three relevant regions: *Same Hemisphere ISRA*, *Opposite Hemisphere ISRA* and *FSR*.

7.3.1 Same Hemisphere ISRA

By imposing that the zero-jettiness of eq. (7.12) computed on the projected Φ_1 configuration is equal to the fully recursive zero-jettiness of eq. (7.11), and from the conditions given in section 7.3 we find the expressions for $\bar{p}$ and $\bar{q}$

$$\begin{cases} \hat{\bar{p}}_1^+ = \hat{p}_1^+ + \hat{p}_2^+ \\ \hat{\bar{p}}_1^- = \dfrac{\hat{p}_1^-}{\hat{p}_1^+}\left(\hat{p}_1^+ + \hat{p}_2^+\right) \\ \hat{\bar{p}}_{1\text{T}}^2 = \dfrac{\hat{p}_1^-}{\hat{p}_1^+}\left(\hat{p}_1^+ + \hat{p}_2^+\right)^2 \\ \bar{\Phi}_1 = \Phi_1. \end{cases} \qquad \begin{cases} \bar{q}^+ = e^{-y_{\text{CS}}}\sqrt{m_{\text{CS}}^2 + \dfrac{\hat{p}_1^-}{\hat{p}_1^+}\left(\hat{p}_1^+ + \hat{p}_2^+\right)^2} \\ \bar{q}^- = e^{y_{\text{CS}}}\sqrt{m_{\text{CS}}^2 + \dfrac{\hat{p}_1^-}{\hat{p}_1^+}\left(\hat{p}_1^+ + \hat{p}_2^+\right)^2} \\ \bar{q}_{\text{T}}^2 = \dfrac{\hat{p}_1^-}{\hat{p}_1^+}\left(\hat{p}_1^+ + \hat{p}_2^+\right)^2 \\ \bar{\Phi}_q = \Phi_1 + \pi. \end{cases} \tag{7.27}$$

Finally, from the equations of momentum conservation we find the expressions for $\bar{x}_a$ and $\bar{x}_b$

$$\begin{cases} \bar{x}_a = \dfrac{e^{y_{\text{CS}}}}{\sqrt{S}} \left[\sqrt{m_{\text{CS}}^2 + \dfrac{\hat{p}_1^-}{\hat{p}_1^+} \left(\hat{p}_1^+ + \hat{p}_2^+ \right)^2} + \dfrac{\hat{p}_1^-}{\hat{p}_1^+} \left(\hat{p}_1^+ + \hat{p}_2^+ \right) \right] \\ \bar{x}_b = \dfrac{e^{-y_{\text{CS}}}}{\sqrt{S}} \left[\sqrt{m_{\text{CS}}^2 + \dfrac{\hat{p}_1^-}{\hat{p}_1^+} \left(\hat{p}_1^+ + \hat{p}_2^+ \right)^2} + \hat{p}_1^+ + \hat{p}_2^+ \right], \end{cases} \tag{7.28}$$

where we called $S = (P_a + P_b)^2$.

7.3.2 Opposite Hemisphere ISRA

By imposing that the zero-jettiness of eq. (7.14) computed on the projected Φ_1 configuration is equal to the fully recursive zero-jettiness of eq. (7.13), and from the conditions given in section 7.3 we find the expressions for $\bar{p}$ and $\bar{q}$

$$\begin{cases} \hat{\bar{p}}_1^+ = \dfrac{\hat{p}_1^+}{\hat{p}_1^-} \left(\hat{p}_1^- + \hat{p}_2^+ \right) \\ \hat{\bar{p}}_1^- = \hat{p}_1^- + \hat{p}_2^+ \\ \hat{\bar{p}}_{\text{T}1}^2 = \dfrac{\hat{p}_1^+}{\hat{p}_1^-} \left(\hat{p}_1^- + \hat{p}_2^+ \right)^2 \\ \bar{\Phi}_1 = \Phi_1. \end{cases} \qquad \begin{cases} \bar{q}^+ = e^{-y_{\text{CS}}} \sqrt{m_{\text{CS}}^2 + \dfrac{\hat{p}_1^+}{\hat{p}_1^-} \left(\hat{p}_1^- + \hat{p}_2^+ \right)^2} \\ \bar{q}^- = e^{y_{\text{CS}}} \sqrt{m_{\text{CS}}^2 + \dfrac{\hat{p}_1^+}{\hat{p}_1^-} \left(\hat{p}_1^- + \hat{p}_2^+ \right)^2} \\ \bar{q}_{\text{T}}^2 = \dfrac{\hat{p}_1^+}{\hat{p}_1^-} \left(\hat{p}_1^- + \hat{p}_2^+ \right)^2 \\ \bar{\Phi}_q = \Phi_1 + \pi. \end{cases} \tag{7.29}$$

Finally, from the equations of momentum conservation we find the expressions for $\bar{x}_a$ and $\bar{x}_b$

$$\begin{cases} \bar{x}_a = \dfrac{e^{y_{\text{CS}}}}{\sqrt{S}} \left[\sqrt{m_{\text{CS}}^2 + \dfrac{\hat{p}_1^+}{\hat{p}_1^-} \left(\hat{p}_1^- + \hat{p}_2^+ \right)^2} + \hat{p}_1^- + \hat{p}_2^+ \right] \\ \bar{x}_b = \dfrac{e^{-y_{\text{CS}}}}{\sqrt{S}} \left[\sqrt{m_{\text{CS}}^2 + \dfrac{\hat{p}_1^+}{\hat{p}_1^-} \left(\hat{p}_1^- + \hat{p}_2^+ \right)^2} + \dfrac{\hat{p}_1^+}{\hat{p}_1^-} \left(\hat{p}_1^- + \hat{p}_2^+ \right) \right], \end{cases} \tag{7.30}$$

where we called $S = (P_a + P_b)^2$.

7.3.3 FSR

By imposing that the zero-jettiness of eq. (7.20) computed on the projected Φ_1 configuration is equal to the fully recursive zero-jettiness of eq. (7.19), and from

the conditions given in section 7.3 we find the expressions for $\bar{p}_1$ and $\bar{q}$

$$\begin{cases} \hat{\bar{p}}_1^+ = \hat{p}_{12}^+ \\ \hat{\bar{p}}_1^- = \hat{p}_{12}^- \\ \hat{\bar{p}}_{1\mathrm{T}}^2 = \hat{p}_{12}^- \hat{p}_{12}^+ \\ \bar{\Phi}_1 = \Phi_{12}. \end{cases} \qquad \begin{cases} \bar{q}^+ = e^{-y_{\mathrm{CS}}} \sqrt{m_{\mathrm{CS}}^2 + \hat{p}_{12}^- \hat{p}_{12}^+} \\ \bar{q}^- = e^{y_{\mathrm{CS}}} \sqrt{m_{\mathrm{CS}}^2 + \hat{p}_{12}^- \hat{p}_{12}^+} \\ \bar{q}_{\mathrm{T}}^2 = \hat{p}_{12}^- \hat{p}_{12}^+ \\ \bar{\Phi}_q = \Phi_q. \end{cases} \tag{7.31}$$

Finally, from the equations of momentum conservation we find the expressions for $\bar{x}_a$ and $\bar{x}_b$

$$\begin{cases} \bar{x}_a = \dfrac{e^{y_{\mathrm{CS}}}}{\sqrt{S}} \left(\sqrt{m_{\mathrm{CS}}^2 + \hat{p}_{12}^- \hat{p}_{12}^+} + \hat{p}_{12}^- \right) \\ \bar{x}_b = \dfrac{e^{-y_{\mathrm{CS}}}}{\sqrt{S}} \left(\sqrt{m_{\mathrm{CS}}^2 + \hat{p}_{12}^- \hat{p}_{12}^+} + \hat{p}_{12}^+ \right), \end{cases} \tag{7.32}$$

where we called $S = (P_a + P_b)^2$.

7.4 Inverse mapping

7.4.1 Same Hemisphere ISRA

From the expression of $\mathcal{T}_1$ given in eq. (7.6) and after introducing

$$z = \frac{\sqrt{S}\bar{x}_a}{\sqrt{S}\bar{x}_a + e^{y_{\mathrm{CS}}} \hat{p}_2^-}. \tag{7.33}$$

we find the expression for p_2. At that point p_1 is obtained by inverting the formulae for $\bar{p}_1$ given in eq. (7.27).

$$\begin{cases} \hat{p}_2^+ = \mathcal{T}_1 \\ \hat{p}_2^- = e^{-y_{\mathrm{CS}}} \sqrt{S}\, \bar{x}_a \dfrac{1-z}{z} \\ \hat{p}_{2\mathrm{T}}^2 = e^{-y_{\mathrm{CS}}} \sqrt{S}\, \bar{x}_a \mathcal{T}_1 \dfrac{1-z}{z} \end{cases} \qquad \begin{cases} \hat{p}_1^+ = \hat{\bar{p}}_1^+ - \mathcal{T}_1 \\ \hat{p}_1^- = \hat{\bar{p}}_1^- \left(1 - \dfrac{\mathcal{T}_1}{\hat{\bar{p}}_1^+} \right) \\ \hat{p}_{1\mathrm{T}}^2 = \hat{\bar{p}}_1^- \hat{\bar{p}}_1^+ \left(1 - \dfrac{\mathcal{T}_1}{\hat{\bar{p}}_1^+} \right)^2 \\ \Phi_1 = \bar{\Phi}_1. \end{cases} \tag{7.34}$$

Finally, from the conservation of $m_{\rm CS}$ and $y_{\rm CS}$ we find

$$\begin{cases} x_a = \dfrac{e^{y_{\rm CS}}}{\sqrt{S}} \left(\hat{p}_1^- + \hat{p}_2^- + \sqrt{m_{\rm CS}^2 + \hat{p}_{1\rm T}^2 + \hat{p}_{2\rm T}^2 + 2\hat{p}_{1\rm T}\hat{p}_{2\rm T}\cos(\phi - \Phi_1)} \right) \\ x_b = \dfrac{e^{-y_{\rm CS}}}{\sqrt{S}} \left(\hat{p}_1^+ + \hat{p}_2^+ + \sqrt{m_{\rm CS}^2 + \hat{p}_{1\rm T}^2 + \hat{p}_{2\rm T}^2 + 2\hat{p}_{1\rm T}\hat{p}_{2\rm T}\cos(\phi - \Phi_1)} \right). \end{cases} \tag{7.35}$$

Since x_a and x_b depend on ϕ, we cannot us the above expressions inside the f_{kj} functions presented in eq. (5.8), because otherwise we would need to perform a numerical integration over ϕ (see eq. (5.5)). To avoid that, we evaluate the PDFs inside the splitting functions at the approximated values

$$\begin{cases} x_a = \dfrac{e^{y_{\rm CS}}}{\sqrt{S}} \left(\hat{p}_1^- + \hat{p}_2^- + \sqrt{m_{\rm CS}^2 + (\hat{p}_{1\rm T} - \hat{p}_{2\rm T})^2} \right) \\ x_b = \dfrac{e^{-y_{\rm CS}}}{\sqrt{S}} \left(\hat{p}_1^+ + \hat{p}_2^+ + \sqrt{m_{\rm CS}^2 + (\hat{p}_{1\rm T} - \hat{p}_{2\rm T})^2} \right). \end{cases} \tag{7.36}$$

The above expressions guarantees that both x_a and x_b are still in the allowed interval $(0, 1)$. Furthermore, we remind that the normalization of the splitting functions ensures that such an approximation has no effect on the distributions that depend only on Φ_1 and $\mathcal{T}_1$. The effect on the other distributions has also proven to be well below the theoretical uncertainties estimated through the ordinary scale variations.

7.4.2 Opposite Hemisphere ISRA

The only differences with respect to the formulae presented above are in the expression for p_1, since now we need to invert the expressions of $\bar{p}_1$ given in eq. (7.29) and we find

$$\begin{cases} \hat{p}_1^+ = \hat{\bar{p}}_1^+ \left(1 - \dfrac{\mathcal{T}_1}{\hat{\bar{p}}_1^-} \right) \\ \hat{p}_1^- = \hat{\bar{p}}_1^- - \mathcal{T}_1 \\ \hat{p}_{1\rm T}^2 = \hat{\bar{p}}^- \hat{\bar{p}}^+ \left(1 - \dfrac{\mathcal{T}_1}{\hat{\bar{p}}^-} \right)^2 \\ \Phi_1 = \bar{\Phi}_1. \end{cases} \tag{7.37}$$

7.4.3 FSR

From the expression of $\mathcal{T}_1$ given in eq. (7.2) and by inverting the formulae for $\bar{p}_1$ from eq. (7.31) we find the expression for p_{12}

$$\begin{cases} \hat{p}_{12}^{+} = \hat{\bar{p}}_1^{+} \\ \hat{p}_{12}^{-} = \hat{\bar{p}}_1^{-} \\ \hat{p}_{12\mathrm{T}}^2 = \hat{\bar{p}}^{-}\hat{\bar{p}}^{+} - \mathcal{T}_1\left(\hat{\bar{p}}^{-} + \hat{\bar{p}}^{+}\right) + \mathcal{T}_1^2 \\ \Phi_{12} = \bar{\Phi}_1. \end{cases} \tag{7.38}$$

Moreover, from the conservation of m_{CS} and y_{CS} we find

$$\begin{cases} x_a = \dfrac{e^{y_{\mathrm{CS}}}}{\sqrt{S}}\left(\hat{\bar{p}}^{-} + \sqrt{m_{\mathrm{CS}}^2 + \hat{\bar{p}}^{-}\hat{\bar{p}}^{+} - \mathcal{T}_1\left(\hat{\bar{p}}^{-} + \hat{\bar{p}}^{+}\right) + \mathcal{T}_1^2}\right) \\ x_b = \dfrac{e^{-y_{\mathrm{CS}}}}{\sqrt{S}}\left(\hat{\bar{p}}^{+} + \sqrt{m_{\mathrm{CS}}^2 + \hat{\bar{p}}^{-}\hat{\bar{p}}^{+} - \mathcal{T}_1\left(\hat{\bar{p}}^{-} + \hat{\bar{p}}^{+}\right) + \mathcal{T}_1^2}\right). \end{cases} \tag{7.39}$$

In this case we define

$$z = \frac{p_1^0}{p_1^0 + p_2^0} \tag{7.40}$$

and ϕ as the azimuthal angle of p_2 in the center-of-mass frame of p_{12}. After calling

$$\beta_0 = \frac{|\vec{p}_{12}|}{p_{12}^0} \tag{7.41}$$

the speed of p_{12} in the laboratory frame, we can then rewrite

$$z = \frac{1 - \beta_0 y}{2}, \tag{7.42}$$

where $y = \cos\theta$, and θ and ϕ are the polar angles of p_2 in the center-of-mass frame of p_{12}. These definitions allow us to have two simple expressions for p_1 and p_2 in the center-of-mass frame of p_{12}. The corresponding formulae in the laboratory frame can then be obtained after the appropriate Lorentz transformation.

7.5 Integration limits

The phase space for the production of the color singlet with two final-state partons reads

$$\begin{aligned} d\Phi_2 = dx_a\, dx_b \prod_{i=1}^{n} \frac{d^4q_i}{(2\pi)^3}\,\delta\left(q_i^2 - m_i^2\right)\theta\left(q_i^0\right) \frac{d^4p_1}{(2\pi)^3}\,\delta\left(p_1^2\right)\theta\left(p_1^0\right) \\ \times \frac{d^4p_2}{(2\pi)^3}\,\delta\left(p_2^2\right)\theta\left(p_2^0\right)(2\pi)^4\,\delta^4\left(\sum_{i=1}^{n} q_i + p_1 + p_2 - x_a P_a - x_b P_b\right). \end{aligned} \tag{7.43}$$

As we did for the $1 \to 0$ mapping, we first want to write it as the product of the phase space with the undecayed color singlet times the phase space $d\Phi_{\text{CS}}$ for the decay presented in eq. (6.7). To do this, we multiply the above expression by

$$\frac{dm_{\text{CS}}^2}{2\pi}\frac{d^4q}{(2\pi)^3}\,\delta\big(q^2-m_{\text{CS}}^2\big)\,\theta\big(q^0\big)\,(2\pi)^4\,\delta^4\left(\sum_{i=1}^{n}q_i-q\right)=1, \tag{7.44}$$

so that we can rewrite $d\Phi_2$ as

$$\begin{aligned} d\Phi_2 = {} & dx_a\,dx_b\,\frac{dm_{\text{CS}}^2}{2\pi}\,\frac{d^4q}{(2\pi)^3}\,\delta\big(q^2-m_{\text{CS}}^2\big)\,\theta\big(q^0\big)\,\frac{d^4p_1}{(2\pi)^3}\,\delta\big(p_1^2\big)\,\theta\big(p_1^0\big) \\ & \times\frac{d^4p_2}{(2\pi)^3}\,\delta\big(p_2^2\big)\,\theta\big(p_2^0\big)\,(2\pi)^4\,\delta^4(q+p_1+p_2-x_aP_a-x_bP_b)\;d\Phi_{\text{CS}}\big(m_{\text{CS}}^2\big)\,. \end{aligned} \tag{7.45}$$

7.5.1 ISRA

To compute the limits on z and ϕ in the *ISRA* case, it will prove to be useful to use the $+$ and $-$ components of the momenta as integration variables. For this reason we begin this section by writing the formulae that, given a momentum p, allow to write

$$d^4p=\frac{1}{2}\,dp^-\,dp^+\,dp_x\,dp_y, \tag{7.46}$$

and

$$\delta^4(p)=2\,\delta\big(p^-\big)\,\delta\big(p^+\big)\,\delta(p_x)\,\delta(p_y)\,. \tag{7.47}$$

in terms of p^+ and p^-. Furthermore, given a mass $m \geq 0$, it can be seen that

$$\delta\big(p^2-m^2\big)\,\theta\big(p^0\big)=\delta\big(p^-p^+-p_{\text{T}}^2-m^2\big)\,\theta\big(p^-\big)\,\theta\big(p^+\big)\,. \tag{7.48}$$

Constraints imposed by the mapping

At this point, we exploit the invariance of the phase space under Lorentz transformations to rewrite the expression for $d\Phi_2$ given in eq. (7.45) as

$$\begin{aligned} d\Phi_2 = {} & dx_a\,dx_b\,\frac{dm_{\text{CS}}^2}{2\pi}\,\frac{d^4q}{(2\pi)^3}\,\delta\big(q^2-m_{\text{CS}}^2\big)\,\theta\big(q^0\big)\,\frac{d^4\hat{p}_1}{(2\pi)^3}\,\delta\big(\hat{p}_1^2\big)\,\theta\big(\hat{p}_1^0\big) \\ & \times\frac{d^4\hat{p}_2}{(2\pi)^3}\,\delta\big(\hat{p}_2^2\big)\,\theta\big(\hat{p}_2^0\big)\,2\,(2\pi)^4\,\delta\left(\hat{p}_1^-+\hat{p}_2^-+\sqrt{q^-q^+}-\sqrt{S}x_a\sqrt{\frac{q^+}{q^-}}\right) \\ & \times\delta\left(\hat{p}_1^++\hat{p}_2^++\sqrt{q^-q^+}-\sqrt{S}x_b\sqrt{\frac{q^-}{q^+}}\right) \\ & \times\delta(\hat{p}_{1x}+\hat{p}_{2x}+q_x)\,\delta(\hat{p}_{1y}+\hat{p}_{2y}+q_y)\,d\Phi_{\text{CS}}\big(m_{\text{CS}}^2\big)\,, \end{aligned} \tag{7.49}$$

where we used the formula of eq. (7.47) to decompose the δ function. After imposing

$$\begin{aligned} q_x &= -\hat{p}_{1x} - \hat{p}_{2x} & \hat{p}_{1\mathrm{T}}^2 &= \hat{p}_1^- \hat{p}_1^+ \\ q_y &= -\hat{p}_{1y} - \hat{p}_{2y} & \hat{p}_{2\mathrm{T}}^2 &= \hat{p}_2^- \hat{p}_2^+ . \end{aligned} \tag{7.50}$$

we can use four of the δ functions appearing in the expression above to remove the corresponding integrals, so that we arrive to

$$\begin{aligned} d\Phi_2 = dx_a\, dx_b\, dm_{\mathrm{CS}}^2\, dq^-\, dq^+\, \theta\big(q^-\big)\, \theta\big(q^+\big)\, \frac{d\hat{p}_1^-\, d\hat{p}_1^+\, d\Phi_1}{4\,(2\pi)^3}\, \theta\big(\hat{p}_1^-\big)\, \theta\big(\hat{p}_1^+\big) \\ \times \frac{d\hat{p}_2^-\, d\hat{p}_2^+\, d\phi}{4\,(2\pi)^3}\, \theta\big(\hat{p}_2^-\big)\, \theta\big(\hat{p}_2^+\big)\, \delta\left(\hat{p}_1^- + \hat{p}_2^- + \sqrt{q^- q^+} - \sqrt{S} x_a \sqrt{\frac{q^+}{q^-}}\right) \\ \times \delta\left(\hat{p}_1^+ + \hat{p}_2^+ + \sqrt{q^- q^+} - \sqrt{S} x_b \sqrt{\frac{q^-}{q^+}}\right) d\Phi_{\mathrm{CS}}\big(m_{\mathrm{CS}}^2\big) \\ \times \delta\left(q^- q^+ - \hat{p}_1^- \hat{p}_1^+ - \hat{p}_2^- \hat{p}_2^+ - 2\sqrt{\hat{p}_1^- \hat{p}_1^+ \hat{p}_2^- \hat{p}_2^+}\, \cos(\phi - \Phi_1) - m_{\mathrm{CS}}^2\right), \end{aligned} \tag{7.51}$$

where we also made use of the formulae of eqs. (7.46) and (7.48) to simplify the expression. At this point we introduce the new variables $q^- q^+$ and

$$y_{\mathrm{CS}} = \frac{1}{2} \log\left(\frac{q^-}{q^+}\right), \tag{7.52}$$

and rewrite

$$dq^-\, dq^+\, \theta\big(q^-\big)\, \theta\big(q^+\big) = d\big(q^- q^+\big)\; dy_{\mathrm{CS}}\, \theta\big(q^- q^+\big)\,. \tag{7.53}$$

Since the δ function appearing in the last line of above expression for the phase space already imposes that

$$q^- q^+ \geq \left(\sqrt{\hat{p}_1^- \hat{p}_1^+} - \sqrt{\hat{p}_2^- \hat{p}_2^+}\right)^2 + m_{\mathrm{CS}}^2 \geq 0, \tag{7.54}$$

we can remove the factor $\theta(q^- q^+)$. Finally, after setting

$$x_a = \frac{e^{y_{\mathrm{CS}}}}{\sqrt{S}} \left(\hat{p}_1^- + \hat{p}_2^- + \sqrt{q^- q^+}\right) \tag{7.55}$$

$$x_b = \frac{e^{-y_{\mathrm{CS}}}}{\sqrt{S}} \left(\hat{p}_1^+ + \hat{p}_2^+ + \sqrt{q^- q^+}\right), \tag{7.56}$$

and

$$q^- q^+ = \hat{p}_1^- \hat{p}_1^+ + \hat{p}_2^- \hat{p}_2^+ + 2\sqrt{\hat{p}_1^- \hat{p}_1^+ \hat{p}_2^- \hat{p}_2^+}\, \cos(\phi - \Phi_1) + m_{\mathrm{CS}}^2. \tag{7.57}$$

we can use the last three remaining δ functions to remove three more integrals, and arrive to

$$d\Phi_2 = \frac{dm_{\rm CS}^2\, dy_{\rm CS}}{S} \frac{d\hat{p}_1^-\, d\hat{p}_1^+\, d\Phi_1}{4\,(2\pi)^3}\, \theta\big(\hat{p}_1^-\big)\theta\big(\hat{p}_1^+\big) \frac{d\hat{p}_2^-\, d\hat{p}_2^+\, d\phi}{4\,(2\pi)^3}\, \theta\big(\hat{p}_2^-\big)\theta\big(\hat{p}_2^+\big)\, d\Phi_{\rm CS}\big(m_{\rm CS}^2\big) \\ \times \theta\Big(\sqrt{S}e^{-y_{\rm CS}} - \hat{p}_1^- - \hat{p}_2^- - \sqrt{q^-q^+}\Big)\, \theta\Big(\sqrt{S}e^{y_{\rm CS}} - \hat{p}_1^+ - \hat{p}_2^+ - \sqrt{q^-q^+}\Big)\,, \tag{7.58}$$

with the two θ functions coming from the requirements that x_a and x_b are smaller than 1. The integration limits on z and ϕ are then given by the conditions that

$$\begin{cases} \sqrt{q^-q^+} < \sqrt{S}e^{-y_{\rm CS}} - \hat{p}_1^- - \hat{p}_2^- \\ \sqrt{q^-q^+} < \sqrt{S}e^{y_{\rm CS}} - \hat{p}_1^+ - \hat{p}_2^+ . \end{cases} \tag{7.59}$$

The reason why it is useful to write the integral in such a way is that the integration variables $m_{\rm CS}$, $y_{\rm CS}$, $\hat{p}_1^-$, $\hat{p}_1^+$, Φ_1 and $\hat{p}_2^+$ are only functions of the underlying phase space $d\Phi_1$ and the one-jettiness $\mathcal{T}_1$, and we can directly associate $\hat{p}_2^-$ to the expression of z given in eq. (7.33). The integration limits we are looking for are then given by the solutions of the two above inequalities with respect to ϕ, which exist only if both the right-hand sides of the inequalities are positive. Since the second one does not depend neither on z nor on ϕ, meaning that it does not provide any condition on such variables, we can limit ourselves to requiring that

$$\hat{p}_2^- < \sqrt{S}e^{-y_{\rm CS}} - \hat{p}_1^- . \tag{7.60}$$

Finally, after solving the inequalities, we find that ϕ is constrained by the conditions

$$\begin{cases} \cos(\phi - \Phi_1) < \dfrac{\Big(\sqrt{S}e^{-y_{\rm CS}} - \hat{p}_1^- - \hat{p}_2^-\Big)^2 - \hat{p}_1^-\hat{p}_1^+ - \hat{p}_2^-\hat{p}_2^+ - m_{\rm CS}^2}{2\sqrt{\hat{p}_1^-\hat{p}_1^+\hat{p}_2^-\hat{p}_2^+}} \\ \cos(\phi - \Phi_1) < \dfrac{\Big(\sqrt{S}e^{y_{\rm CS}} - \hat{p}_1^+ - \hat{p}_2^+\Big)^2 - \hat{p}_1^-\hat{p}_1^+ - \hat{p}_2^-\hat{p}_2^+ - m_{\rm CS}^2}{2\sqrt{\hat{p}_1^-\hat{p}_1^+\hat{p}_2^-\hat{p}_2^+}} . \end{cases} \tag{7.61}$$

Constraints imposed by the slicing of the phase space

At this point, we have to keep in mind that the integral over z and ϕ should cover only the phase space where the one-jettiness, among the five possible different expressions presented in eqs. (7.2) and (7.4), reads $\mathcal{T}_1 = \hat{p}_2^+$, and the zero-jettiness, among the four possible different expressions presented in eq. (7.8), reads $\mathcal{T}_0 = \hat{p}_1^+ + \hat{p}_2^+$ for the *Same Hemisphere ISRA* case or $\mathcal{T}_0 = \hat{p}_1^- + \hat{p}_2^+$ for the *Opposite Hemisphere ISRA* case. This imposes further constraints on z and ϕ to be combined with those already derived in eqs. (7.60) and (7.61). The condition that

$$\mathcal{T}_1 = \hat{p}_2^+ < \min\Big(\hat{p}_1^+, \hat{p}_1^-, \hat{p}_2^-, \hat{p}_{12}^0 - \Big|\vec{\hat{p}}_{12}\Big|\Big) . \tag{7.62}$$

gives us four inequalities, of which only two depend on z and ϕ. By solving them, we find the two further constraints

$$\hat{p}_2^- > \hat{p}_2^+ \tag{7.63}$$

and

$$\cos(\phi - \Phi_1) < \frac{\hat{p}_1^+ \left(\hat{p}_2^- - \hat{p}_2^+\right) - \hat{p}_2^- \hat{p}_2^+}{2\sqrt{\hat{p}_1^- \hat{p}_1^+ \hat{p}_2^- \hat{p}_2^+}}. \tag{7.64}$$

After enforcing the constraint given in eq. (7.63), the condition on the zero-jettiness simplifies to $\hat{p}_1^+ < \hat{p}_1^-$ in the *Same Hemisphere ISRA* case and $\hat{p}_1^- < \hat{p}_1^+$ in the *Opposite Hemisphere ISRA* case. Since neither $\hat{p}_1^-$ nor $\hat{p}_1^+$ depend on z and ϕ, this does not impose any further constraint on such variables.

7.5.2 FSR

Constraints imposed by the mapping

As we did for the *ISRA* case in the section above, we start from the expression for $d\Phi_2$ given in eq. (7.45). This time we multiply it by

$$\frac{dM^2}{2\pi} \frac{d^4p_{12}}{(2\pi)^3} \delta\left(p_{12}^2 - M^2\right) \theta\left(p_{12}^0\right) (2\pi)^4 \delta^4(p_1 + p_2 - p_{12}) = 1, \tag{7.65}$$

so that we can write

$$\begin{aligned} d\Phi_2 = {} & dx_a\, dx_b\, \frac{dm_{\text{CS}}^2}{2\pi} \frac{dM^2}{2\pi} \frac{d^4q}{(2\pi)^3} \delta\left(q^2 - m_{\text{CS}}^2\right) \theta\left(q^0\right) \frac{d^4p_{12}}{(2\pi)^3} \delta\left(p_{12}^2 - M^2\right) \theta\left(p_{12}^0\right) \\ & \times (2\pi)^4 \delta^4(q + p_{12} - x_a P_a - x_b P_b)\, d\Phi_{\text{rad}}\left(M^2\right)\, d\Phi_{\text{CS}}\left(m_{\text{CS}}^2\right), \end{aligned} \tag{7.66}$$

factorizing out the radiation phase space

$$d\Phi_{\text{rad}} = \frac{d^4p_1}{(2\pi)^3} \delta\left(p_1^2\right) \theta\left(p_1^0\right) \frac{d^4p_2}{(2\pi)^3} \delta\left(p_2^2\right) \theta\left(p_2^0\right) (2\pi)^4 \delta^4(p_1 + p_2 - p_{12}) = \frac{dy\, d\phi}{32\pi^2}, \tag{7.67}$$

where $y = \cos\theta$, and θ and ϕ are the polar angles of p_2 in the center-of-mass frame of p_{12}. At this point, we follow the steps that took us from eq. (7.45) to eq. (7.58), which allows us to write

$$\begin{aligned} d\Phi_2 = {} & \frac{dm_{\text{CS}}^2\, dy_{\text{CS}}}{S} \frac{dM^2}{2\pi} \frac{d\hat{p}_{12}^-\, d\hat{p}_{12}^+\, d\Phi}{4\,(2\pi)^3} \theta\left(\hat{p}_{12}^-\right) \theta\left(\hat{p}_{12}^+\right) d\Phi_{\text{rad}}\left(M^2\right) d\Phi_{\text{CS}}\left(m_{\text{CS}}^2\right) \\ & \times \theta\left(\sqrt{S} e^{-y_{\text{CS}}} - \hat{p}_{12}^- - \sqrt{q^- q^+}\right) \theta\left(\sqrt{S} e^{y_{\text{CS}}} - \hat{p}_{12}^+ - \sqrt{q^- q^+}\right), \end{aligned} \tag{7.68}$$

where

$$q^- q^+ = \hat{p}_{12}^- \hat{p}_{12}^+ - M^2 + m_{\text{CS}}^2. \tag{7.69}$$

Since the dependence on z and ϕ is entirely within the radiation phase space $d\Phi_{\text{rad}}$ and $y \in (-1,1)$, from the expression of z given in eq. (7.42), at fixed Φ_1 and $\mathcal{T}_1$ the integration limits imposed by the *FSR* mapping on z and ϕ are

$$z \in \left(\frac{1-\beta_0}{2}, \frac{1+\beta_0}{2}\right) \qquad \phi \in (0, 2\pi)\,. \tag{7.70}$$

Constraints imposed by the slicing of the phase space

As we did for the *ISRA* case, we now need to impose that the expression for $\mathcal{T}_1$ in the *FSR* case, given in eq. (7.2), is smaller that those we would use in the *ISR* case, given in eq. (7.4), or in other words

$$\mathcal{T}_1 < \min\left(\hat{p}_1^+, \hat{p}_1^-, \hat{p}_2^+, \hat{p}_2^-\right). \tag{7.71}$$

However, to do that, we need first to define the offset of the azimuthal angle ϕ. We begin by introducing Θ and Φ as the polar angles of p_{12} in the laboratory frame, and $Y = \cos\Theta$, so that we can write

$$p_{12} = \frac{M}{\sqrt{1-\beta_0^2}} \left(\begin{array}{c} 1 \\ \beta_0 \left(\begin{array}{c} \sqrt{1-Y^2}\cos\Phi \\ \sqrt{1-Y^2}\sin\Phi \\ Y \end{array} \right) \end{array} \right). \tag{7.72}$$

At this point we can express p_1 and p_2 in terms of M, β_0, Y, Φ, y and ϕ, thus specifying the offset of ϕ. Since such expressions are lengthy, we report them separately in page 55. From them we can finally write the four additional constraints that y and ϕ needs to fulfill as

$$\begin{cases} e^{\pm y_{\text{CS}}} \dfrac{M}{2} \left[\dfrac{1-\beta_0 y \mp (\beta_0 - y)\, Y}{\sqrt{1-\beta_0^2}} \mp \sqrt{1-y^2}\sqrt{1-Y^2}\cos(\phi-\Phi) \right] > \mathcal{T}_1 \\ e^{\pm y_{\text{CS}}} \dfrac{M}{2} \left[\dfrac{1+\beta_0 y \mp (\beta_0 + y)\, Y}{\sqrt{1-\beta_0^2}} \pm \sqrt{1-y^2}\sqrt{1-Y^2}\cos(\phi-\Phi) \right] > \mathcal{T}_1 \end{cases} \tag{7.73}$$

where the expressions for β_0 and Y in terms of the integration variables used in eq. (7.68) are given by

$$\beta_0 = \frac{\sqrt{\left(e^{y_{\text{CS}}}\hat{p}_{12}^- - e^{-y_{\text{CS}}}\hat{p}_{12}^+\right)^2 + \hat{p}_{12}^-\hat{p}_{12}^+ - M^2}}{e^{y_{\text{CS}}}\hat{p}_{12}^- + e^{-y_{\text{CS}}}\hat{p}_{12}^+} \tag{7.74}$$

and

$$Y = \frac{e^{y_{\text{CS}}}\hat{p}_{12}^- - e^{-y_{\text{CS}}}\hat{p}_{12}^+}{\sqrt{\left(e^{y_{\text{CS}}}\hat{p}_{12}^- - e^{-y_{\text{CS}}}\hat{p}_{12}^+\right)^2 + \hat{p}_{12}^-\hat{p}_{12}^+ - M^2}}. \tag{7.75}$$

Momenta of the final-state partons

In the center-of-mass frame of p_{12}, p_1 and p_2 read respectively

$$p_1^* = \frac{M}{2}\left(\begin{array}{c} 1 \\ -\sqrt{1-y^2}\cos(\phi-\Phi)\begin{pmatrix} Y\cos\Phi \\ Y\sin\Phi \\ -\sqrt{1-Y^2}\end{pmatrix} - \sqrt{1-y^2}\sin(\phi-\Phi)\begin{pmatrix} -\sin\Phi \\ \cos\Phi \\ 0\end{pmatrix} - y\begin{pmatrix} \sqrt{1-Y^2}\cos\Phi \\ \sqrt{1-Y^2}\sin\Phi \\ Y\end{pmatrix}\end{array}\right)$$

$$p_2^* = \frac{M}{2}\left(\begin{array}{c} 1 \\ \sqrt{1-y^2}\cos(\phi-\Phi)\begin{pmatrix} Y\cos\Phi \\ Y\sin\Phi \\ -\sqrt{1-Y^2}\end{pmatrix} + \sqrt{1-y^2}\sin(\phi-\Phi)\begin{pmatrix} -\sin\Phi \\ \cos\Phi \\ 0\end{pmatrix} + y\begin{pmatrix} \sqrt{1-Y^2}\cos\Phi \\ \sqrt{1-Y^2}\sin\Phi \\ Y\end{pmatrix}\end{array}\right).$$

In the laboratory frame instead they read

$$p_1 = \frac{M}{2}\left(\begin{array}{c} \dfrac{1-\beta_0 y}{\sqrt{1-\beta_0^2}} \\ -\sqrt{1-y^2}\cos(\phi-\Phi)\begin{pmatrix} Y\cos\Phi \\ Y\sin\Phi \\ -\sqrt{1-Y^2}\end{pmatrix} - \sqrt{1-y^2}\sin(\phi-\Phi)\begin{pmatrix} -\sin\Phi \\ \cos\Phi \\ 0\end{pmatrix} + \dfrac{\beta_0-y}{\sqrt{1-\beta_0^2}}\begin{pmatrix} \sqrt{1-Y^2}\cos\Phi \\ \sqrt{1-Y^2}\sin\Phi \\ Y\end{pmatrix}\end{array}\right)$$

$$p_2 = \frac{M}{2}\left(\begin{array}{c} \dfrac{1+\beta_0 y}{\sqrt{1-\beta_0^2}} \\ \sqrt{1-y^2}\cos(\phi-\Phi)\begin{pmatrix} Y\cos\Phi \\ Y\sin\Phi \\ -\sqrt{1-Y^2}\end{pmatrix} + \sqrt{1-y^2}\sin(\phi-\Phi)\begin{pmatrix} -\sin\Phi \\ \cos\Phi \\ 0\end{pmatrix} + \dfrac{\beta_0+y}{\sqrt{1-\beta_0^2}}\begin{pmatrix} \sqrt{1-Y^2}\cos\Phi \\ \sqrt{1-Y^2}\sin\Phi \\ Y\end{pmatrix}\end{array}\right).$$

By solving the above inequalities with respect to ϕ we find the four additional constraints to impose to be

$$\begin{cases} \cos(\phi-\Phi) < \dfrac{1}{\sqrt{1-y^2}\sqrt{1-Y^2}}\left(\dfrac{1-\beta_0 y-(\beta_0-y)\,Y}{\sqrt{1-\beta_0^2}}-\dfrac{2\mathcal{T}_1}{M}e^{-y_{\rm CS}}\right) \\ \cos(\phi-\Phi) > -\dfrac{1}{\sqrt{1-y^2}\sqrt{1-Y^2}}\left(\dfrac{1-\beta_0 y+(\beta_0-y)\,Y}{\sqrt{1-\beta_0^2}}-\dfrac{2\mathcal{T}_1}{M}e^{y_{\rm CS}}\right) \\ \cos(\phi-\Phi) > -\dfrac{1}{\sqrt{1-y^2}\sqrt{1-Y^2}}\left(\dfrac{1+\beta_0 y-(\beta_0+y)\,Y}{\sqrt{1-\beta_0^2}}-\dfrac{2\mathcal{T}_1}{M}e^{-y_{\rm CS}}\right) \\ \cos(\phi-\Phi) < \dfrac{1}{\sqrt{1-y^2}\sqrt{1-Y^2}}\left(\dfrac{1+\beta_0 y+(\beta_0+y)\,Y}{\sqrt{1-\beta_0^2}}-\dfrac{2\mathcal{T}_1}{M}e^{y_{\rm CS}}\right). \end{cases} \tag{7.76}$$

Constraints imposed by the signature

In the case where there are two gluons in the final state, we always call p_2 the one with less energy, so that we need to impose the extra condition

$$z > \frac{1}{2}. \tag{7.77}$$

7.6 Jacobian

Starting from the expression of eq. (6.6) and following the same steps that took us from eq. (7.45) to eq. (7.58), we can write the phase space with one final-state partons as

$$\begin{aligned} d\Phi_1 = {} & dm^2_{\rm CS}\, dy_{\rm CS}\, \frac{d\hat{\bar{p}}_1^-\, d\hat{\bar{p}}_1^+\, d\bar{\Phi}_1}{4\,(2\pi)^3}\, \theta\big(\hat{\bar{p}}_1^-\big)\, \theta\big(\hat{\bar{p}}_1^+\big)\, d\Phi_{\rm CS}\big(m^2_{\rm CS}\big) \\ & \times \theta\Big(\sqrt{S}e^{-y_{\rm CS}} - \hat{\bar{p}}_1^- - \sqrt{\bar{q}^-\bar{q}^+}\Big)\, \theta\Big(\sqrt{S}e^{y_{\rm CS}} - \hat{\bar{p}}_1^+ - \sqrt{\bar{q}^-\bar{q}^+}\Big), \end{aligned} \tag{7.78}$$

where

$$\bar{q}^-\bar{q}^+ = \hat{\bar{p}}_1^-\hat{\bar{p}}_1^+ + m^2_{\rm CS}. \tag{7.79}$$

7.6.1 ISRA

At this point, we need to factorize out the underlying phase space $d\Phi_1$ presented above from the expression of $d\Phi_2$ given in eq. (7.58). We begin by using eqs. (7.34) and (7.37) to rewrite

$$d\hat{\bar{p}}_1^-\, d\hat{\bar{p}}_1^+\, d\Phi_1 = d\hat{\bar{p}}_1^-\, d\hat{\bar{p}}_1^+\, d\bar{\Phi}_1 \left(1-\frac{\mathcal{T}_1}{\mathcal{T}_0}\right). \tag{7.80}$$

Since $d\hat{p}_2^+ = d\mathcal{T}_1$ and, from eq. (7.33),

$$d\hat{p}_2^- = \sqrt{S}\bar{x}_a e^{-y_{\rm CS}} \frac{dz}{z^2}, \tag{7.81}$$

we can finally write

$$\frac{d\Phi_2}{d\Phi_1\, d\mathcal{T}_1\, dz\, d\phi} = \frac{\sqrt{S}\bar{x}_a e^{-y_{\rm CS}}}{4\,(2\pi)^3} \left(1 - \frac{\mathcal{T}_1}{\mathcal{T}_0}\right) \frac{1}{z^2}. \tag{7.82}$$

7.6.2 FSR

We start the derivation of the Jacobian from the expression for $d\Phi_2$ given in eq. (7.68). From eq. (7.38) we can write

$$d\hat{p}_{12}^-\, d\hat{p}_{12}^+\, d\Phi = d\hat{\bar{p}}_1^-\, d\hat{\bar{p}}_1^+\, d\bar{\Phi}_1 \tag{7.83}$$

and

$$\frac{dM^2}{2\pi} = \frac{d\mathcal{T}_1}{2\pi} \left(\hat{\bar{p}}^- + \hat{\bar{p}}^+ - 2\mathcal{T}_1\right). \tag{7.84}$$

Furthermore, from eqs. (7.67) and (7.42)

$$d\Phi_{\rm rad}\big(M^2\big) = \frac{dz\, d\phi}{4\,(2\pi)^2\,\beta_0}, \tag{7.85}$$

so that we can finally write

$$\frac{d\Phi_2}{d\Phi_1\, d\mathcal{T}_1\, dz\, d\phi} = \frac{\hat{\bar{p}}^- + \hat{\bar{p}}^+ - 2\mathcal{T}_1}{4\,(2\pi)^3\,\beta_0}. \tag{7.86}$$

Chapter 8

IR subtraction in the non-singular cumulant

In the fixed-order contribution to the 0-jet exclusive differential cross section, we have to deal with the subtraction of the infrared divergences appearing in the virtual and real matrix elements. In GENEVA this problem is solved by performing a Monte Carlo integration on the radiation phase space of eq. (6.11) parametrized with the FKS variables ξ, y and ϕ. However, with respect to a pure fixed-order calculation we have a further complication due to the fact that we need to move the real contributions with $\mathcal{T}_0 > \mathcal{T}_0^{\rm cut}$ to the 1-jet cross section. This amounts to giving a logarithmically-enhanced dependence on $\mathcal{T}_0^{\rm cut}$ to the fixed-order term, which will be cancelled by the corresponding resummed-expanded term. There are then two cancellations of different nature inside the non-singular contribution: one is the proper subtraction of the infrared divergences within the fixed-order term, while the other is the cancellation of the logarithmically-enhanced (with respect to $\mathcal{T}_0^{\rm cut}$) terms between the fixed-order and resummed-expanded contributions.

The easiest way of performing the infrared subtraction discussed above would be just to implement a $\theta(\mathcal{T}_0^{\rm cut} - \mathcal{T}_0)$ function that sets to zero the real contributions with $\mathcal{T}_0 > \mathcal{T}_0^{\rm cut}$. In this section we will instead try to optimize the calculation by performing an analytic separation of the terms that are not power-suppressed with respect to $\mathcal{T}_0^{\rm cut}$ and cancel in the sum with the resummed-expanded contribution (which we will call counterterms) from those that enter in the proper infrared subtraction. The first are numerically by far the larger contribution, but their integration requires a high precision (comparable to that used in the cumulant of the resummed-expanded term). The second can instead become significantly time consuming from the computational point of view, since they depend on the real matrix elements. Their separation allows us to obtain two computational improvements.

1. By setting differently the number of points used in the integration we can keep the computational time under control without sacrificing the

precision of the integral of the counterterms.

2. Since the counterterms do not depend on the real matrix elements, we can perform the integration over y analytically.

To separate the two contributions, we need to compute the integration limits on ξ, y and ϕ taking into account the constraint $\mathcal{T}_0 > \mathcal{T}_0^{\text{cut}}$. Furthermore, since we want to perform the integration over y analytically, we choose to compute the limits on y at fixed ξ, instead of the opposite.

8.1 Integration limits

The constraints imposed by the $1 \to 0$ mapping presented in section 6 on the FKS variables are given by eq. (6.25), and, using eqs. (6.20) and (6.21), can be rewritten as

$$\begin{cases} x_a(y) = \dfrac{\bar{x}_a}{\sqrt{1-\xi}} \sqrt{\dfrac{2-\xi\,(1-y)}{2-\xi\,(1+y)}} < 1 \\ x_b(y) = \dfrac{\bar{x}_b}{\sqrt{1-\xi}} \sqrt{\dfrac{2-\xi\,(1+y)}{2-\xi\,(1-y)}} < 1, \end{cases} \tag{8.1}$$

where

$$\bar{x}_a = \frac{m_{\text{CS}}}{\sqrt{S}}\, e^{y_{\text{CS}}} \qquad \bar{x}_b = \frac{m_{\text{CS}}}{\sqrt{S}}\, e^{-y_{\text{CS}}}. \tag{8.2}$$

We notice that x_a and x_b are respectively a growing and a decreasing function of y in the interval $y \in (-1, 1)$, with

$$x_a : (-1,1) \to \left(\bar{x}_a,\, \frac{\bar{x}_a}{1-\xi}\right) \qquad x_b : (-1,1) \to \left(\bar{x}_b,\, \frac{\bar{x}_b}{1-\xi}\right). \tag{8.3}$$

In order for both the inequalities to be satisfied we need to impose that the point y where $x_a(y) = x_b(y) = x$ is such that $x < 1$, which imposes that

$$\xi \in (0,\, 1 - \bar{x}_a \bar{x}_b)\,. \tag{8.4}$$

For a fixed ξ in the above range, the integration limits for y then read

$$-\min\left(1, \frac{2-\xi}{\xi}\frac{1-\bar{x}_b^2-\xi}{1+\bar{x}_b^2-\xi}\right) < y < \min\left(1, \frac{2-\xi}{\xi}\frac{1-\bar{x}_a^2-\xi}{1+\bar{x}_a^2-\xi}\right). \tag{8.5}$$

The constraints imposed by the inequalities of eq. (8.1) discard the points on the left of the blue and orange curves presented in figure 8.1.

When integrating over the radiation phase space for a given underlying configuration Φ_0 we need to divide $d\Phi_1$ into different regions to deal with the different infrared limits. In this case there are two singular regions (*ISRA* and *ISRB*), separated by the condition given in eq. (6.2), which, in terms of the FKS variables, simply reads

$$y > 0. \tag{8.6}$$

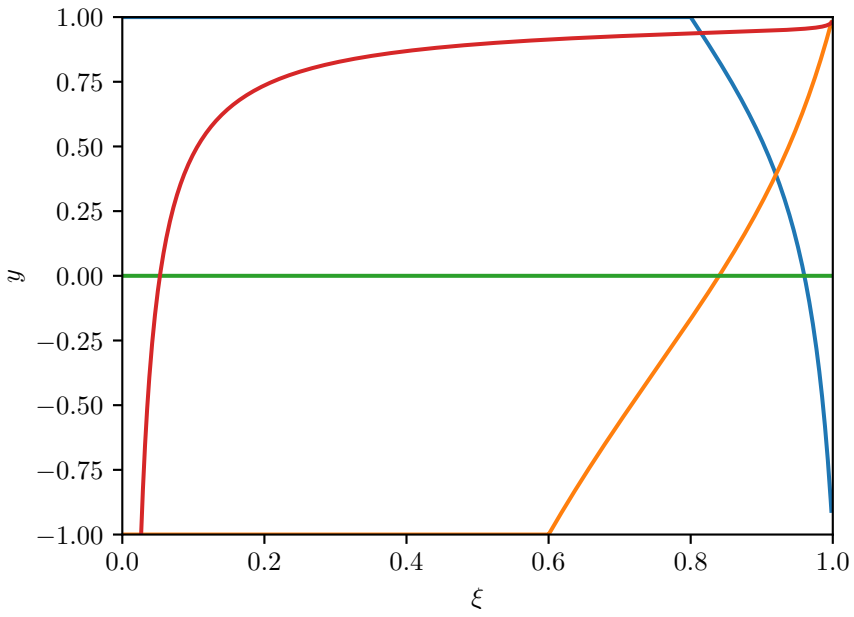

Figure 8.1: The four constraints on ξ and y.

In the rest of this section we will focus on the *ISRA* case (identified by the above equation), since the *ISRB* one can be obtained from a parity transformation. The above condition selects the points above the green line in figure 8.1. This new constraint on y introduces the possibility that the upper integration limit on ξ is dictated by the crossing of the blue and green lines of figure 8.1, instead of the blue and orange ones. This imposes the new constraint

$$\xi < 1 - \bar{x}_a^2, \tag{8.7}$$

to be combined with those given in eq. (8.4).

We are now left with imposing the constraint $\mathcal{T}_0 < \mathcal{T}_0^{\text{cut}}$, which from eq. (6.15) reads

$$\mathcal{T}_0(y) = \frac{m_{\text{CS}}}{2} \frac{\xi\,(1-y)}{\sqrt{1-\xi}} \sqrt{\frac{2-\xi\,(1+y)}{2-\xi\,(1-y)}} < \mathcal{T}_0^{\text{cut}}. \tag{8.8}$$

Since $\mathcal{T}_0$ is a monotonically decreasing function of y with

$$\mathcal{T}_0 : (0,1) \to \left(0,\, \frac{m_{\text{CS}}}{2} \frac{\xi}{\sqrt{1-\xi}}\right), \tag{8.9}$$

it sets an additional lower limit on y if

$$\frac{m_{\text{CS}}}{2} \frac{\xi}{\sqrt{1-\xi}} > \mathcal{T}_0^{\text{cut}}. \tag{8.10}$$

After introducing, for ease of notation, the auxiliary variables

$$x = \xi\,(1-y) \qquad \omega = 1-\xi \qquad \kappa = \frac{2\mathcal{T}_0^{\rm cut}}{m_{\rm CS}}, \tag{8.11}$$

such a limit on y is given by the real solution to the cubic equation

$$x^3 + 2\omega x^2 + \kappa^2\omega x - 2\kappa^2\omega = 0, \tag{8.12}$$

which, after defining

$$z = x + \frac{2}{3}\omega, \tag{8.13}$$

can be further simplified to

$$z^3 + pz + q = 0, \tag{8.14}$$

where we have introduced

$$p = -\omega\left(\frac{4}{3}\omega - \kappa^2\right) \qquad q = 2\omega\left[\frac{8}{27}\omega^2 - \kappa^2\left(1+\frac{\omega}{3}\right)\right]. \tag{8.15}$$

The three complex solutions to eq. (8.14) are given by

$$z = \sqrt[3]{-\frac{q}{2} + \sqrt{\frac{q^2}{4}+\frac{p^3}{27}}} - \frac{\frac{p}{3}}{\sqrt[3]{-\frac{q}{2} + \sqrt{\frac{q^2}{4}+\frac{p^3}{27}}}}, \tag{8.16}$$

where the square and cubic roots have to be understood as complex multivalued functions. There are then two possibilities.

1. If

$$\frac{q^2}{4}+\frac{p^3}{27} > 0 \tag{8.17}$$

the argument of the cubic root is real and we can simplify the expression of eq. (8.16) to be

$$z = e^{\frac{2}{3}k\pi i}\sqrt[3]{-\frac{q}{2} + \sqrt{\frac{q^2}{4}+\frac{p^3}{27}}} + e^{-\frac{2}{3}k\pi i}\sqrt[3]{-\frac{q}{2} - \sqrt{\frac{q^2}{4}+\frac{p^3}{27}}}, \tag{8.18}$$

where k can be any integer number and this time the squared and cubic roots have to be understood as real functions. Out of the three possible values for z only one (that with $k=0$) is real.

2. If instead

$$\frac{q^2}{4}+\frac{p^3}{27} < 0 \tag{8.19}$$

the argument of the cubic root is not real anymore, but its squared modulus is equal to $-\pi/3$, so that we can write

$$\sqrt[3]{-\frac{q}{2}+\sqrt{\frac{q^2}{4}+\frac{p^3}{27}}} = e^{i\left(\theta+\frac{2}{3}k\pi\right)}\sqrt{-\frac{p}{3}}, \tag{8.20}$$

for some real phase θ that we can always choose such that

$$-\frac{\pi}{3} < \theta < \frac{\pi}{3}. \tag{8.21}$$

At this point the expression of eq. (8.16) can be simplified to

$$z = 2\cos\left(\theta+\frac{2}{3}k\pi\right)\sqrt{-\frac{p}{3}}, \tag{8.22}$$

which gives us three different real solutions.

We now want to show that the solution with $k = 0$ (which we will call principal solution) provides the lower integration limit on y we are looking for. Since such a solution must be a continuous curve parametrized by the variables $\bar{x}_a$, κ and ω, we will provide the demonstration in two steps. First, we will show that the principal solution can never reach the boundaries of the principal region (where $\theta = \pm\pi/3$), and then we will prove that there exist one choice of the parameters for which the principal solution is the only real solution (meaning that it is the solution we are looking for). The principal solution would reach the boundaries of the principal region only if the argument of the cubic root became real and negative. This would mean that

$$\begin{cases} \dfrac{q^2}{4}+\dfrac{p^3}{27} > 0 \\ -\dfrac{q}{2}+\sqrt{\dfrac{q^2}{4}+\dfrac{p^3}{27}} < 0. \end{cases} \tag{8.23}$$

By solving the above inequalities in terms of κ and ω, we find that there are no solutions. It can be immediately seen that in the limit of high κ the argument of the cubic root is a positive number, meaning that the principal solution is the only real solution. This completes the demonstration.

This new constraint sets the integration region on y to be above the red curve in figure 8.1. However, it also introduces the possibility that the upper integration limit on ξ is dictated by the crossing of the blue and red lines of figure 8.1, instead of the blue and orange, or the blue and green ones. Similarly to what we did for $x_a(y)$ and $x_b(y)$, we have to impose that the point y for which $x = x_a(y) = \mathcal{T}_0(y)/\mathcal{T}_0^{\text{cut}}$ is such that $x < 1$. This imposes the new constraint

$$\xi < 1 - \bar{x}_a\left(\frac{-\kappa\bar{x}_a+\sqrt{16\bar{x}_a^2+8\kappa\bar{x}_a+\kappa^2\bar{x}_a^2}}{2\left(2\bar{x}_a+\kappa\right)}\right), \tag{8.24}$$

to be combined with those given in eqs. (8.4) and (8.7).

8.2 Fixed-order cumulant

In this section we consider a generic process of diboson production. We call $\bar{p}_a$ and $\bar{p}_b$ the flavors of the incoming partons in the LO process and $\bar{x}_a$ and $\bar{x}_b$ the fraction of hadronic momenta they carry. We also call $f_i^a(x)$ and $f_i^b(x)$ the PDFs of the parton i carrying a fraction of momentum x of the hadrons a and b respectively, and $H^{(0)}$ the LO amplitude for the process. The cumulant of the fixed-order is given by the sum of three independently finite contributions: the soft-virtual term, the collinear remnants, and the IR-subtracted real amplitude.

8.2.1 Soft-virtual contribution

The soft-virtual contribution can be recovered from eq. (2.99) of ref. [9] and in our case is given by

$$\sigma_{\text{softvirt}} = f^a_{\bar{p}_a}(\bar{x}_a)\, f^b_{\bar{p}_b}(\bar{x}_b)\, \frac{\alpha_{\text{S}}}{2\pi} \left\{ \left[C_k \left(\log^2\!\left(\frac{m^2_{\text{CS}}}{Q^2} \right) - \frac{\pi^2}{3} \right) - 2\gamma_k \log\!\left(\frac{\mu^2_{\text{F}}}{Q^2} \right) \right] H^{(0)} + H^{(1)}_{\text{OL}}\big(\mu^2_{\text{R}}, Q^2\big) \right\}, \tag{8.25}$$

where μ_{F} is the factorization scale, $H^{(1)}_{\text{OL}}\big(\mu^2_{\text{R}}, Q^2\big)$ is the one-loop amplitude evaluated at the renormalization scale μ_{R} and subtraction scale Q in the subtraction scheme used by OpenLoops (see eq. (4.2) of ref. [33]), $k = q$ for the quark-initiated processes, $k = g$ for the gluon-initiated ones, and

$$\begin{aligned} C_q &= C_{\text{F}} & \gamma_q &= \frac{3}{2} C_{\text{F}} \\ C_g &= C_{\text{A}} & \gamma_g &= \frac{11 C_{\text{A}} - 4 T_{\text{F}} n_{\text{f}}}{6}. \end{aligned} \tag{8.26}$$

Since

$$H^{(1)}_{\text{OL}}\big(\mu^2_{\text{R}}, Q^2\big) = H^{(1)}_{\overline{\text{MS}}}\big(m^2_{\text{CS}}, m^2_{\text{CS}}\big) + \left[- C_k \left(\log^2\!\left(\frac{Q^2}{m^2_{\text{CS}}} \right) + \frac{\pi^2}{6} \right) - 2\gamma_k \log\!\left(\frac{Q^2}{m^2_{\text{CS}}} \right) + n\beta_0 \log\!\left(\frac{\mu^2_{\text{R}}}{m^2_{\text{CS}}} \right) \right] H^{(0)}, \tag{8.27}$$

where n is the power of the strong coupling in the LO amplitude, we can rewrite the soft-virtual contribution given in eq. (8.25) as

$$\sigma_{\text{softvirt}} = f^a_{\bar{p}_a}(\bar{x}_a)\, f^b_{\bar{p}_b}(\bar{x}_b)\, \frac{\alpha_{\text{S}}}{2\pi} \left\{ \left[-\frac{\pi^2}{2} C_k - 2\gamma_k \log\!\left(\frac{\mu^2_{\text{F}}}{m^2_{\text{CS}}} \right) + n\beta_0 \log\!\left(\frac{\mu^2_{\text{R}}}{m^2_{\text{CS}}} \right) \right] H^{(0)} + H^{(1)}_{\overline{\text{MS}}}\big(m^2_{\text{CS}}, m^2_{\text{CS}}\big) \right\}. \tag{8.28}$$

Real	Collinear
$\xi \in (0, \xi_{\max})$	$\xi \in (0, 1-\bar{x}_a)$
$y \in (y_{\min}, y_{\max})$	$y \in (-1, 1)$
Soft	**Soft-Collinear**
$\xi \in (0, 1)$	$\xi \in (0, 1)$
$y \in (0, 1)$	$y \in (-1, 1)$

Table 8.1: Original integration limits on ξ and y for the unsubtracted real and the soft, collinear and soft-collinear counterterms. The limits of the same color should be made the same to guarantee the subtraction to be local.

8.2.2 Collinear remnants contribution

The expression for the collinear remnants can be derived from eq. (2.102) of [9] and read

$$\sigma_{\text{collremn}} = \frac{\alpha_{\text{S}}}{2\pi} f^b_{\bar{p}_b}(\bar{x}_b)\, H^{(0)} \int_{\bar{x}_a}^1 \frac{dz}{z} \sum_j f^a_j\left(\frac{\bar{x}_a}{z}\right) \Bigg\{ (1-z)\, P^{\text{AP}}_{\bar{p}_a j}(z) \times \left[\mathcal{L}_0(1-z) \log\left(\frac{m^2_{\text{CS}}}{z\mu^2_{\text{F}}}\right) + 2\mathcal{L}_1(1-z)\right] + P'_{\bar{p}_a j}(z) \Bigg\}, \quad (8.29)$$

where P^{AP}_{kj} and P'_{kj} are given in eq. (3.24) and we have defined

$$\mathcal{L}_n(x) = \lim_{\beta \to 0} \left[\theta(x-\beta)\, \frac{\log^n x}{x} + \delta(x-\beta)\, \frac{\log^{n+1} \beta}{n+1}\right]. \quad (8.30)$$

8.2.3 Subtracted real contribution

The subtraction of the infrared counterterms from the real contribution is done in GENEVA with a Monte Carlo integration after parametrizing the radiation phase space with the FKS variables ξ, y and ϕ. For a given Φ_0 configuration the integral of the real contribution runs over all the Φ_1 configurations with $\mathcal{T}_0 < \mathcal{T}_0^{\text{cut}}$ whose projection is Φ_0. These constraints restrict the integration to the region where $\xi \in (0, \xi_{\max})$ and $y \in (y_{\min}, y_{\max})$, where $\xi_{\max}$ is a function of Φ_0 and $\mathcal{T}_0^{\text{cut}}$ and $y_{\min}$ and $y_{\max}$ are functions of Φ_0, $\mathcal{T}_0^{\text{cut}}$ and ξ. However, in the FKS parametrization the integration limits on ξ and y for the collinear, soft and soft-collinear counterterms are different. We report the values in the case of an *ISRA* region in table 8.1. Since in the Monte Carlo integration the variables ξ and y are built from two random numbers belonging to the interval $(0, 1)$, having different integration limits could spoil the locality of the subtraction. In particular, we have highlighted with the same colors the integration limits which should be the same to guarantee such locality. In the following paragraphs we

will see how we can change the integration limits to become equal to those for the real contribution by changing the integrand function without affecting the subtraction.

Real contribution

The contribution to the cross section of the real matrix elements depends on the specific process we are considering. However, in the soft ($\xi \to 0$) and collinear ($y \to 1$ or $y \to -1$) limit the real amplitude for the production of a color singlet averaged over the azimuthal angle ϕ of the radiation factorizes on the Born amplitude $H^{(0)}$ as

$$R_{\text{IR}}^{kj} = \frac{32\pi\alpha_{\text{S}}}{m_{\text{CS}}^2} \frac{1-\xi}{\xi\,(1-y^2)}\, P_{kj}^{\text{AP}}(1-\xi)\, H^{(0)}. \tag{8.31}$$

Furthermore, we can rewrite the radiation phase space of eq. (6.11) as

$$d\Phi_{\text{rad}} = \frac{m_{\text{CS}}^2}{64\pi^3} \frac{\xi}{(1-\xi)^2}\, d\xi\, dy\, d\phi, \tag{8.32}$$

where this time we have included in the definition of $d\Phi_{\text{rad}}$ also the factor $(1-\xi)$ coming from the ratio between $dx_a\, dx_b$ and $d\bar{x}_a\, d\bar{x}_b$. At this point, the real contribution to the non-singular cumulant in such an approximation can be written as

$$\begin{aligned}\sigma_{\text{real}}^{a} = f_{\bar{p}_b}^{b}(\bar{x}_b)\, \frac{\alpha_{\text{S}}}{2\pi}\, H^{(0)} \int_{\epsilon_\xi}^{1} d\xi \sum_j f_j^a\left(\frac{\bar{x}_a}{1-\xi}\right) \frac{P_{\bar{p}_a j}^{\text{AP}}(1-\xi)}{1-\xi} \int_0^{1-\epsilon_y} dy\, \frac{2}{1-y^2} \\ \times\, \theta(1-x_a)\, \theta(1-x_b)\, \theta(\mathcal{T}_0^{\text{cut}} - \mathcal{T}_0)\,,\end{aligned} \tag{8.33}$$

where ϵ_ξ and ϵ_y are technical cuts used to avoid numerical instabilities in the infrared region. The three θ functions in the above expression enforce the constraints of eqs. (8.1) and (8.8) and set the integration limits on ξ to $(0, \xi_{\text{max}})$ and those on y to $(y_{\text{min}}, y_{\text{max}})$, which allows us to rewrite the integral as

$$\begin{aligned}\sigma_{\text{real}}^{a} = f_{\bar{p}_b}^{b}(\bar{x}_b)\, \frac{\alpha_{\text{S}}}{2\pi}\, H^{(0)} \int_{0}^{\xi_{\text{max}}} d\xi \sum_j f_j^a\left(\frac{\bar{x}_a}{1-\xi}\right) \frac{P_{\bar{p}_a j}^{\text{AP}}(1-\xi)}{1-\xi}\, \theta(\xi - \epsilon_\xi) \\ \times \int_{y_{\text{min}}}^{y_{\text{max}}} dy\, \frac{2}{1-y^2}\, \theta(1-y-\epsilon_y)\,.\end{aligned} \tag{8.34}$$

Collinear counterterm

From the $y \to 1$ limit of eq. (8.31) we can see that in the collinear limit the real amplitude factorizes on the Born one as

$$R_{\text{coll}}^{\bar{p}_a j} = \frac{16\pi\alpha_{\text{S}}}{m_{\text{CS}}^2} \frac{1-\xi}{\xi\,(1-y)}\, P_{\bar{p}_a j}^{\text{AP}}(1-\xi)\, H^{(0)}. \tag{8.35}$$

Using the radiation phase space introduced in eq. (8.32), the collinear counterterm can then be written as

$$\sigma^a_{\rm coll} = -f^b_{\bar{p}_b}(\bar{x}_b)\,\frac{\alpha_{\rm S}}{2\pi}\,H^{(0)}\int_{\epsilon_\xi}^{1-\bar{x}_a} d\xi \sum_j f^a_j\left(\frac{\bar{x}_a}{1-\xi}\right)\frac{P^{\rm AP}_{\bar{p}_a j}(1-\xi)}{1-\xi}\int_{-1}^{1-\epsilon_y}\frac{dy}{1-y}. \tag{8.36}$$

As described before, at this point we need to modify the integration limits on y to match those of the real contribution. After noticing that for every $\xi \in (0, 1-\bar{x}_a)$ $y_{\rm max} = 1$, in a fully general way we can change the range of integration on y from $(-1, 1-\epsilon_y)$ to $(y_{\rm min}, 1)$ by exploiting the relation

$$\int_{-1}^{1-\epsilon_y}\frac{dy}{1-y} = \int_{y_{\rm min}}^{1}\frac{dy}{1-y}\left[\theta(1-y-\epsilon_y) + \frac{1-y}{1-y_{\rm min}}\log\left(\frac{2}{1-y_{\rm min}}\right)\right]. \tag{8.37}$$

Finally, if we take the limits of integration of ξ to be $(0, 1-\bar{x}_a)$ and the limits of integration of y to be $(y_{\rm min}, 1)$ the collinear counterevent reads

$$\begin{aligned}\sigma^a_{\rm coll} = -f^b_{\bar{p}_b}(\bar{x}_b)\,\frac{\alpha_{\rm S}}{2\pi}\,H^{(0)}\int_{0}^{1-\bar{x}_a} d\xi \sum_j f^a_j\left(\frac{\bar{x}_a}{1-\xi}\right)\frac{P^{\rm AP}_{\bar{p}_a j}(1-\xi)}{1-\xi}\,\theta(\xi-\epsilon_\xi)\\ \times\int_{y_{\rm min}}^{1}\frac{dy}{1-y}\left[\theta(1-y-\epsilon_y) + \frac{1-y}{1-y_{\rm min}}\log\left(\frac{2}{1-y_{\rm min}}\right)\right].\end{aligned} \tag{8.38}$$

Soft counterterm

From the $\xi \to 0$ limit of eqs. (8.31) and (8.32) we can see that in the soft limit the real amplitude factorizes on the Born one as

$$R_{\rm soft} = \frac{64\pi\alpha_{\rm S}}{m^2_{\rm CS}}\frac{C_k}{\xi^2\,(1-y^2)}\,H^{(0)}, \tag{8.39}$$

and the soft radiation phase space reads

$$d\Phi^{\rm soft}_{\rm rad} = \frac{m^2_{\rm CS}}{64\pi^3}\,\xi\,d\xi\,dy\,d\phi. \tag{8.40}$$

The soft counterterm can then be written as

$$\sigma^a_{\rm soft} = -f^a_{\bar{p}_a}(\bar{x}_a)\,f^b_{\bar{p}_b}(\bar{x}_b)\,\frac{\alpha_{\rm S}}{2\pi}\,2C_k\,H^{(0)}\int_{\epsilon_\xi}^{1}\frac{d\xi}{\xi}\int_{0}^{1-\epsilon_y} dy\,\frac{2}{1-y^2}. \tag{8.41}$$

At this point we need to modify the integration limits on ξ and y to match those of the real contribution. In this case we can change the range of integration on ξ from $(\epsilon_\xi, 1)$ to $(0, \xi_{\rm max})$ by exploiting the relation

$$\int_{\epsilon_\xi}^{1}\frac{d\xi}{\xi} = \int_{0}^{\xi_{\rm max}}\frac{d\xi}{\xi}\left[\theta(\xi-\epsilon_\xi) + \frac{\xi}{\xi_{\rm max}}\log\left(\frac{1}{\xi_{\rm max}}\right)\right], \tag{8.42}$$

and that on y from $(0, 1-\epsilon_y)$ to $(y_{\min}, 1)$ by exploiting the relation

$$\int_0^{1-\epsilon_y} \frac{dy}{1-y^2} = \int_{y_{\min}}^1 \frac{dy}{1-y^2} \left[\theta(1-y-\epsilon_y) + \frac{1-y^2}{2\,(1-y_{\min})} \log\left(\frac{1+y_{\min}}{1-y_{\min}}\right)\right]. \tag{8.43}$$

This allows us to rewrite the soft counterterm as

$$\sigma^a_{\text{soft}} = -f^a_{\bar{p}_a}(\bar{x}_a)\, f^b_{\bar{p}_b}(\bar{x}_b)\, \frac{\alpha_{\text{S}}}{2\pi}\, 2C_k\, H^{(0)} \int_0^{\xi_{\max}} \frac{d\xi}{\xi} \left[\theta(\xi-\epsilon_\xi) + \frac{\xi}{\xi_{\max}} \log\left(\frac{1}{\xi_{\max}}\right)\right] \times \int_{y_{\min}}^1 dy\, \frac{2}{1-y^2} \left[\theta(1-y-\epsilon_y) + \frac{1-y^2}{2\,(1-y_{\min})} \log\left(\frac{1+y_{\min}}{1-y_{\min}}\right)\right]. \tag{8.44}$$

Soft-collinear counterterm

From the $\xi \to 0$ and $y \to 1$ limits of eqs. (8.31) we can see that in the soft-collinear limit the real amplitude factorizes on the Born one as

$$R_{\text{softcoll}} = \frac{32\pi\alpha_{\text{S}}}{m^2_{\text{CS}}} \frac{C_k}{\xi^2\,(1-y)} H^{(0)}. \tag{8.45}$$

Using the soft radiation phase space given in eq. (8.40), the soft-collinear counterterm can then be written as

$$\sigma^a_{\text{softcoll}} = f^a_{\bar{p}_a}(\bar{x}_a)\, f^b_{\bar{p}_b}(\bar{x}_b)\, \frac{\alpha_{\text{S}}}{2\pi}\, 2C_k\, H^{(0)} \int_{\epsilon_\xi}^1 \frac{d\xi}{\xi} \int_{-1}^{1-\epsilon_y} \frac{dy}{1-y}. \tag{8.46}$$

By using eqs. (8.37) and (8.42) to change the integration limits on ξ from $(\epsilon_\xi, 1)$ to $(0, \xi_{\max})$ and those on y from $(-1, 1-\epsilon_y)$ to $(y_{\min}, 1)$, the soft-collinear counterterm can be rewritten as

$$\sigma^a_{\text{softcoll}} = f^a_{\bar{p}_a}(\bar{x}_a)\, f^b_{\bar{p}_b}(\bar{x}_b)\, \frac{\alpha_{\text{S}}}{2\pi}\, 2C_k\, H^{(0)} \int_0^{\xi_{\max}} \frac{d\xi}{\xi} \left[\theta(\xi-\epsilon_\xi) + \frac{\xi}{\xi_{\max}} \log\left(\frac{1}{\xi_{\max}}\right)\right] \times \int_{y_{\min}}^1 \frac{dy}{1-y} \left[\theta(1-y-\epsilon_y) + \frac{1-y}{1-y_{\min}} \log\left(\frac{2}{1-y_{\min}}\right)\right]. \tag{8.47}$$

8.2.4 Bulk of the fixed-order cumulant

To separate the fixed-order cumulant into two integrals, we begin by summing the real contribution in the limit of small $\mathcal{T}_0$ given in eq. (8.34) with the collinear counterterm given in eq. (8.38)

$$d\sigma^a_{\text{real}} + d\sigma^a_{\text{coll}} = f^b_{\bar{p}_b}(\bar{x}_b)\, \frac{\alpha_{\text{S}}}{2\pi}\, H^{(0)}\, d\xi\, \theta(\xi-\epsilon_\xi) \sum_j f^a_j\left(\frac{\bar{x}_a}{1-\xi}\right) \frac{P^{\text{AP}}_{\bar{p}_a j}(1-\xi)}{1-\xi} \times dy \left[\frac{\theta(1-y-\epsilon_y)}{1+y} - \frac{1}{1-y_{\min}} \log\left(\frac{2}{1-y_{\min}}\right)\right] \frac{d\phi}{2\pi}, \tag{8.48}$$

and the soft and soft-collinear counterterms given in eqs. (8.44) and (8.47)

$$d\sigma^a_{\rm soft} + d\sigma^a_{\rm softcoll} = f^a_{\bar{p}_a}(\bar{x}_a)\, f^b_{\bar{p}_b}(\bar{x}_b)\, \frac{\alpha_{\rm S}}{2\pi}\, 2C_k\, H^{(0)} \frac{d\xi}{\xi} \left[\theta(\xi - \epsilon_\xi) + \frac{\xi}{\xi_{\rm max}} \log\!\left(\frac{1}{\xi_{\rm max}}\right)\right] \times dy \left[-\frac{\theta(1-y-\epsilon_y)}{1+y} + \frac{1}{1-y_{\rm min}} \log\!\left(\frac{2}{1+y_{\rm min}}\right)\right] \frac{d\phi}{2\pi}. \tag{8.49}$$

Both the above expressions are now finite in the collinear $y \to 1^-$ limit. To check the cancellation of the soft divergences, we take the $\xi \to 0^+$ limit of the expression given in eq. (8.48)

$$d\sigma^a_{\rm real} + d\sigma^a_{\rm coll} = f^a_{\bar{p}_a}(\bar{x}_a)\, f^b_{\bar{p}_b}(\bar{x}_b)\, \frac{\alpha_{\rm S}}{2\pi}\, 2C_k\, H^{(0)}\, \frac{d\xi}{\xi}\, \theta(\xi - \epsilon_\xi) \times dy \left[\frac{\theta(1-y-\epsilon_y)}{1+y} - \frac{1}{1-y_{\rm min}} \log\!\left(\frac{2}{1-y_{\rm min}}\right)\right] \frac{d\phi}{2\pi}, \tag{8.50}$$

and sum it with eq. (8.49), obtaining

$$\begin{aligned} & d\sigma^a_{\rm real} + d\sigma^a_{\rm coll} + d\sigma^a_{\rm soft} + d\sigma^a_{\rm softcoll} \\ &= f^a_{\bar{p}_a}(\bar{x}_a)\, f^b_{\bar{p}_b}(\bar{x}_b)\, \frac{\alpha_{\rm S}}{2\pi}\, 2C_k\, H^{(0)}\, \frac{d\xi}{\xi}\, dy \Bigg\{ -\frac{\theta(\xi-\epsilon_\xi)}{1-y_{\rm min}} \log\!\left(\frac{1+y_{\rm min}}{1-y_{\rm min}}\right) \\ &\quad + \frac{\xi}{\xi_{\rm max}} \log\!\left(\frac{1}{\xi_{\rm max}}\right) \left[-\frac{\theta(1-y-\epsilon_y)}{1+y} + \frac{1}{1-y_{\rm min}} \log\!\left(\frac{2}{1+y_{\rm min}}\right)\right] \Bigg\} \frac{d\phi}{2\pi}. \end{aligned} \tag{8.51}$$

The expression above is finite in the $\xi \to 0^+$ limit since, for ξ small enough, $y_{\rm min} = 0$. At this point, after integrating over y and ϕ, we define the bulk of the real subtracted integral as

$$\sigma^a_{\rm bulk} = -f^b_{\bar{p}_b}(\bar{x}_b)\, \frac{\alpha_{\rm S}}{2\pi}\, H^{(0)} \int_{\epsilon_\xi}^{1-\bar{x}_a} d\xi \sum_j f^a_j\!\left(\frac{\bar{x}_a}{1-\xi}\right) \frac{P^{\rm AP}_{\bar{p}_a j}(1-\xi)}{1-\xi}\, \log\!\left(\frac{1+y_{\rm min}}{1-y_{\rm min}}\right). \tag{8.52}$$

We now want to show that the above expression contains all the terms that are not power suppressed in $\mathcal{T}_0^{\rm cut}$ by matching them to those of the cumulant of the resummed-expanded. In the limit of small $\mathcal{T}_0^{\rm cut}$ the constraint on $\mathcal{T}_0$ given in eq. (8.8) reduces to

$$\mathcal{T}_0 = \frac{m_{\rm CS}}{2}\, \xi\, (1-y) < \mathcal{T}_0^{\rm cut}. \tag{8.53}$$

The expression above can be obtained equivalently by taking the limit $\xi \to 0^+$ or $y \to 1^-$ in eq. (8.8), since those are the only limits for which $\mathcal{T}_0 \to 0$. By

solving the above inequality we find the expression of $y_{\min}$ in the limit of small $\mathcal{T}_0^{\rm cut}$ to be

$$y_{\min} = \begin{cases} 1 - \dfrac{\kappa}{\xi} & \text{if } \xi > \kappa \\ 0 & \text{if } \xi < \kappa. \end{cases} \tag{8.54}$$

In such a limit the bulk of the integral of the subtracted real contribution presented in eq. (8.52) becomes

$$\sigma^a_{\rm bulk} = -f^b_{\bar{p}_b}(\bar{x}_b)\,\frac{\alpha_{\rm S}}{2\pi}\,H^{(0)}\int_\kappa^{1-\bar{x}_a} d\xi \sum_j f^a_j\left(\frac{\bar{x}_a}{1-\xi}\right)\frac{P^{\rm AP}_{\bar{p}_a j}(1-\xi)}{1-\xi}\log\left(\frac{2\xi}{\kappa}-1\right). \tag{8.55}$$

At this point, we call

$$f(\xi) = -f^b_{\bar{p}_b}(\bar{x}_b)\,\frac{\alpha_{\rm S}}{2\pi}\,H^{(0)}\,\sum_j f^a_j\left(\frac{\bar{x}_a}{1-\xi}\right)\frac{\xi}{1-\xi}P^{\rm AP}_{\bar{p}_a j}(1-\xi) \tag{8.56}$$

and write

$$\sigma^a_{\rm bulk} = \sigma^a_{\rm bulksoft} + \sigma^a_{\rm bulkcoll}, \tag{8.57}$$

where

$$\sigma^a_{\rm bulksoft} = \int_\kappa^1 \frac{d\xi}{\xi}\,f(0)\log\left(\frac{2\xi}{\kappa}-1\right) \tag{8.58}$$

and

$$\sigma^a_{\rm bulkcoll} = \int_\kappa^{1-\bar{x}_a}\frac{d\xi}{\xi}\,f(\xi)\log\left(\frac{2\xi}{\kappa}-1\right) - \int_\kappa^1\frac{d\xi}{\xi}\,f(0)\log\left(\frac{2\xi}{\kappa}-1\right). \tag{8.59}$$

Since

$$\begin{aligned}\int_\kappa^1 \frac{d\xi}{\xi}\log\left(\frac{2\xi}{\kappa}-1\right) &= \log\left(\frac{m_{\rm CS}}{\mathcal{T}_0^{\rm cut}}\right)\log\left(\frac{m_{\rm CS}}{\mathcal{T}_0^{\rm cut}}-1\right) + {\rm Li}_2\left(1-\frac{m_{\rm CS}}{\mathcal{T}_0^{\rm cut}}\right) + \frac{\pi^2}{12} \\ &= \frac{1}{2}\log^2\left(\frac{m_{\rm CS}}{\mathcal{T}_0^{\rm cut}}\right) - \frac{\pi^2}{12} + \mathcal{O}\left(\frac{\mathcal{T}_0^{\rm cut}}{m_{\rm CS}}\right),\end{aligned} \tag{8.60}$$

the soft contribution to the bulk can be expressed as

$$\sigma^a_{\rm bulksoft} = -f^a_{\bar{p}_a}(\bar{x}_a)\,f^b_{\bar{p}_b}(\bar{x}_b)\,\frac{\alpha_{\rm S}}{2\pi}\,H^{(0)}\,C_k\,\left[\log^2\left(\frac{m_{\rm CS}}{\mathcal{T}_0^{\rm cut}}\right) - \frac{\pi^2}{6}\right] + \mathcal{O}\left(\frac{\mathcal{T}_0^{\rm cut}}{m_{\rm CS}}\right). \tag{8.61}$$

The collinear contribution can instead be written as

$$\begin{aligned}\sigma^a_{\rm bulkcoll} &= \lim_{\beta\to 0^+}\left[\int_\beta^{1-\bar{x}_a}\frac{d\xi}{\xi}\,f(\xi)\log\left(\frac{2\xi}{\kappa}\right) - \int_\beta^1\frac{d\xi}{\xi}\,f(\beta)\log\left(\frac{2\xi}{\kappa}\right)\right] + \mathcal{O}(\kappa) \\ &= \int_0^{1-\bar{x}_a} d\xi\,f(\xi)\left[\log\left(\frac{m_{\rm CS}}{\mathcal{T}_0^{\rm cut}}\right)\mathcal{L}_0(\xi) + \mathcal{L}_1(\xi)\right] + \mathcal{O}\left(\frac{\mathcal{T}_0^{\rm cut}}{m_{\rm CS}}\right)\end{aligned} \tag{8.62}$$

and, after introducing the new integration variable $z = 1 - \xi$, it is finally equal to

$$\sigma^a_{\text{bulkcoll}} = -f^b_{\bar{p}_b}(\bar{x}_b)\,\frac{\alpha_{\text{S}}}{2\pi}\,H^{(0)}\int_{\bar{x}_a}^1 \frac{dz}{z}\sum_j f^a_j\left(\frac{\bar{x}_a}{z}\right)(1-z)\,P^{\text{AP}}_{\bar{p}_a j}(z) \\ \times\left[\log\left(\frac{m_{\text{CS}}}{\mathcal{T}_0^{\text{cut}}}\right)\mathcal{L}_0(1-z)+\mathcal{L}_1(1-z)\right]+\mathcal{O}\left(\frac{\mathcal{T}_0^{\text{cut}}}{m_{\text{CS}}}\right). \quad (8.63)$$

After summing half (since we are just considering *ISRA* emissions) of the soft-virtual contribution from eq. (8.28) with the collinear remnants of eq. (8.29) and the bulk of the IR-subtracted real integral given by eqs. (8.61) and (8.63), we arrive to the final expression for the cumulant of the fixed-order contribution

$$\begin{aligned}
&\sigma^a_{\text{FO}}(\mathcal{T}_0^{\text{cut}}) = \frac{1}{2}\sigma_{\text{softvirt}} + \sigma^a_{\text{collremn}} + \sigma^a_{\text{bulksoft}} + \sigma^a_{\text{bulkcoll}} \\
&= \frac{\alpha_{\text{S}}}{2\pi}\,f^b_{\bar{p}_b}(\bar{x}_b)\;H^{(0)}\Bigg\{f^a_{\bar{p}_a}(\bar{x}_a)\,C_k\left[-\log^2\left(\frac{m_{\text{CS}}}{\mathcal{T}_0^{\text{cut}}}\right)-\frac{\pi^2}{12}\right] \\
&\quad-\int_{\bar{x}_a}^1\frac{dz}{z}\sum_j f^a_j\left(\frac{\bar{x}_a}{z}\right)(1-z)\,P^{\text{AP}}_{\bar{p}_a j}(z)\left[\mathcal{L}_0(1-z)\log\left(\frac{m_{\text{CS}}}{\mathcal{T}_0^{\text{cut}}}\right)-\mathcal{L}_1(1-z)\right] \\
&\quad+\int_{\bar{x}_a}^1\frac{dz}{z}\sum_j f^a_j\left(\frac{\bar{x}_a}{z}\right)\left[P'_{\bar{p}_a j}(z)-P^{\text{AP}}_{\bar{p}_a j}(z)\log z\right]\Bigg\} \\
&\quad+\frac{\alpha_{\text{S}}}{2\pi}\,f^a_{\bar{p}_a}(\bar{x}_a)\,f^b_{\bar{p}_b}(\bar{x}_b)\,\frac{1}{2}H^{(1)}_{\overline{\text{MS}}}+\mathcal{O}\left(\frac{\mathcal{T}_0^{\text{cut}}}{m_{\text{CS}}}\right), \qquad (8.64)
\end{aligned}$$

where we have set $\mu_{\text{R}} = \mu_{\text{F}} = m_{\text{CS}}$. We notice that the above expression exactly matches the resummed-expanded cumulant presented in eq. (3.46) up to $\mathcal{T}_0^{\text{cut}}$ power corrections.

Chapter 9

Phenomenological results

9.1 Physical parameters

The phenomenological results presented in this chapter were obtained for a proton-proton collider with a hadronic center-of-mass energy $\sqrt{S} = 13$ TeV. We used the PDF set `NNPDF31_nnlo_as_0118` from LHAPDF [34] and the evolution of α_s provided by the same package, treating all the quarks except for the top as massless (5-flavor scheme).

The EW constants are set in the G_μ scheme, where the Fermi constant G_μ and the masses m_W and m_Z and widths Γ_W and Γ_Z of the W and Z bosons are taken as independent parameters, from which the EW coupling α_{EW} and the Weinberg angle θ_W are derived. Furthermore, we work in the complex-mass scheme [35] and define the complex masses of the $V = W, Z$ bosons as

$$\mu_V^2 = m_V^2 - i\Gamma_V m_V. \tag{9.1}$$

Using the above definition, the Weinberg angle θ_W is given by

$$\cos^2\theta_W = \frac{\mu_W^2}{\mu_Z^2} \tag{9.2}$$

and the EW coupling reads

$$\alpha_{EW} = \frac{\sqrt{2}}{\pi} G_\mu \left| \mu_W^2 \sin^2\theta_W \right|. \tag{9.3}$$

The physical distributions presented in this section were obtained setting the Fermi constant to [36]

$$G_\mu = 1.1663787 \times 10^{-5}\ \text{GeV}^{-2} \tag{9.4}$$

and the on-shell masses and widths of the W and Z bosons to [37]

$$\begin{aligned} m_W^{OS} &= 80.379\ \text{GeV} & \Gamma_W^{OS} &= 2.085\ \text{GeV} \\ m_Z^{OS} &= 91.1876\ \text{GeV} & \Gamma_Z^{OS} &= 2.4952\ \text{GeV}. \end{aligned} \tag{9.5}$$

Finally, following the prescription of ref. [38], the pole masses and widths of the $V = W, Z$ bosons are obtained from the corresponding on-shell masses and widths as

$$m_{\rm V}^2 = \frac{\left(m_{\rm V}^{\rm OS}\right)^2}{\left(m_{\rm V}^{\rm OS}\right)^2 + \left(\Gamma_{\rm V}^{\rm OS}\right)^2} \qquad \Gamma_{\rm V}^2 = \frac{\left(\Gamma_{\rm V}^{\rm OS}\right)^2}{\left(m_{\rm V}^{\rm OS}\right)^2 + \left(\Gamma_{\rm V}^{\rm OS}\right)^2}. \tag{9.6}$$

Starting from the order $\alpha_{\rm s}^2$ in the strong coupling expansion, Feynman diagrams with top-quark loops appear. To evaluate them, we set the mass of the top quark to [39]

$$m_{\rm t} = 173.1 \text{ GeV}. \tag{9.7}$$

Since such diagrams may contain Higgs-boson propagators, we set the mass $m_{\rm H}$ and width $\Gamma_{\rm H}$ of the Higgs boson to [40]

$$m_{\rm H} = 125 \text{ GeV} \qquad \Gamma_{\rm H} = 4.07 \times 10^{-3} \text{ GeV}. \tag{9.8}$$

9.2 External code and theoretical parameters

The phase space for the process is generated by the Monte Carlo integrator MUNICH, also used in the MATRIX NNLO calculations [41]. The matrix elements up to one loop are instead computed by OPENLOOPS2 [33, 42, 43], while those with two loops were implemented analytically within GENEVA starting from the master integrals provided by the VVAMP code [44].

The phenomenological distributions presented in this chapter were obtained using the $2 \to 1$ mapping that does not preserve the transverse momentum $q_{\rm T}$ of the color singlet (see section 7), and setting the N-jettiness resolution parameters appearing in the GENEVA formulae (see eqs. (4.17), (4.26) and (4.27)) to

$$\mathcal{T}_0^{\rm cut} = 1 \text{ GeV} \qquad \mathcal{T}_1^{\rm cut} = 1 \text{ GeV}. \tag{9.9}$$

The factorization and renormalization scales are set to the mass of the color singlet and the theoretical uncertainties are estimated through a 3-point scale variation where such scales are multiplied and divided by a factor $K = 1/2, 1, 2$ and the minimum and maximum results are taken as the envelope of the uncertainties.

9.3 Analysis cuts

In the following we will present distributions for two different final-state signatures associated to the production of two Z bosons, for which we define two sets of phase-space cuts.

1. The *different-flavor* signature $p\,p \to e^-\,e^+\,\mu^-\,\mu^+$. In this case, we include in the definition of the cross section only the configurations where the masses of the two lepton-antilepton pairs $m_{e^-e^+}$ and $m_{\mu^-\mu^+}$ are in the range

$$50 \text{ GeV} < m_{\ell^-\ell^+} < 150 \text{ GeV}. \tag{9.10}$$

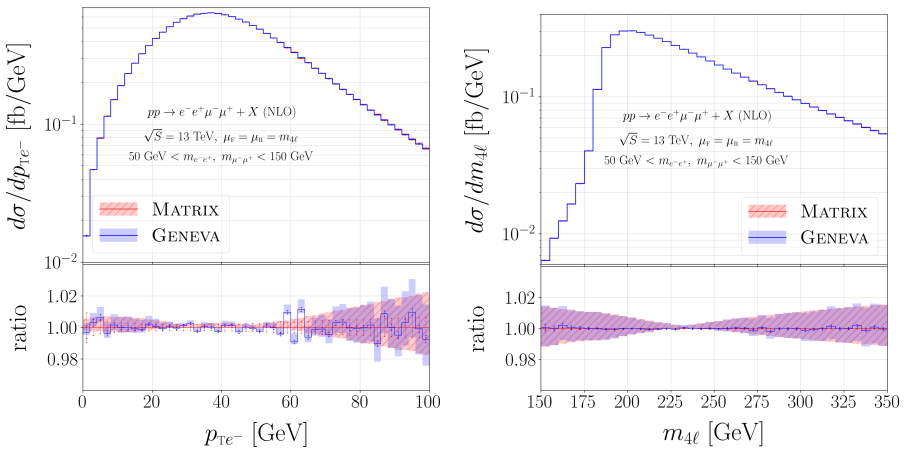

Figure 9.1: MATRIX and GENEVA NLO distributions for the transverse momentum $p_{T e^-}$ of the electron and the mass $m_{4\ell}$ of the 4-lepton system in the process $pp \to e^- e^+ \mu^- \mu^+ + X$. The bands represent the theoretical uncertainties estimated through three-point scale variations. The lower panes show the ratio between the two curves.

This ensures the removal of the EW singularities in the limit $m_{\ell^-\ell^+} \to 0$.

2. The *same-flavor* signature $pp \to e^- e^+ e^- e^+$. In this case we remove the EW singularities by asking that any electron-positron pair has mass

$$m_{e^-e^+} > 4 \text{ GeV}. \tag{9.11}$$

At this point, we call Z_1 the intermediate off-shell Z boson given by the sum of the momenta of the electron-positron pair whose mass is the closest to the physical mass m_Z given in eq. (9.6), and Z_2 the other pair. We limit the definition of the cross section to the configurations where

$$60 \text{ GeV} < m_{Z_1}, m_{Z_2} < 120 \text{ GeV}. \tag{9.12}$$

All the phase-space cuts described above are applied on observables that are preserved by both the $1 \to 0$ and $2 \to 1$ mappings. Because of this, we can apply them at the generation level (i.e. not generating the configurations that are outside the boundaries), thus improving the efficiency of the event generator.

9.4 Validation

To validate the implementation of the code, we begin by comparing the two NLO calculations on which the GENEVA results are based to the fixed-order predictions provided by MATRIX. In figure 9.1 we show the comparison between the MATRIX

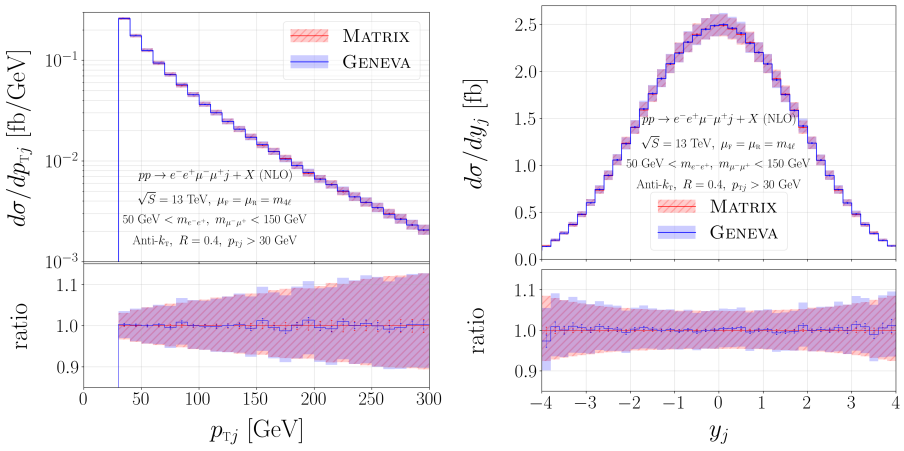

Figure 9.2: MATRIX and GENEVA NLO distributions for the transverse momentum p_{tj} and rapidity y_j of the hardest jet in the process $p\,p \to e^-\,e^+\,\mu^-\,\mu^+\,j+X$. The bands represent the theoretical uncertainties estimated through three-point scale variations. The lower panes show the ratio between the two curves.

and GENEVA NLO predictions for the transverse momentum of the electron and the mass of the 4-lepton system in the process $p\,p \to e^-\,e^+\,\mu^-\,\mu^+ + X$. In figure 9.2 instead we consider the process $p\,p \to e^-\,e^+\,\mu^-\,\mu^+\,j + X$ with one additional jet in the final state and show the comparison between the MATRIX and GENEVA NLO predictions for the transverse momentum and rapidity of such a jet. Since we are just comparing two fixed-order calculation we expect and observe a perfect agreement (within the statistical fluctuations) in both cases.

In figure 9.3 and 9.4 instead we compare the GENEVA prediction before the reweighting with the NNLO results from MATRIX. In this case there are two effects that can potentially introduce discrepancies between the two results. The first is due to the missing $\mathcal{O}(\alpha_s^2)$ power corrections to the 0-jet exclusive cross section. The second instead is due to the fact that the resummation moves contributions across phase spaces with different parton multiplicities. Because of this, only the observables that are preserved by both the $1 \to 0$ and $2 \to 1$ mappings are theoretically expected to have the same distribution they would have in a fixed-order calculation. In figure 9.3 we show three distributions that are preserved by the two mappings: the mass $m_{4\ell}$ and rapidity $y_{4\ell}$ of the 4-lepton system, the mass $m_{e^-e^+}$ of the electron-positron pair and the rapidity y_{e^-} of the electron. Despite the missing power corrections, all of them display a good agreement with MATRIX. Furthermore, we show the distribution for the rapidity y_{e^-} of the electron, which, despite not being preserved by the mappings, is in good agreement with the fixed-order predictions. This does not happen instead for the two distributions presented in figure 9.4, namely the transverse momenta of the electron-positron pair ($p_{te^-e^+}$) and the electron (p_{te^-}), for

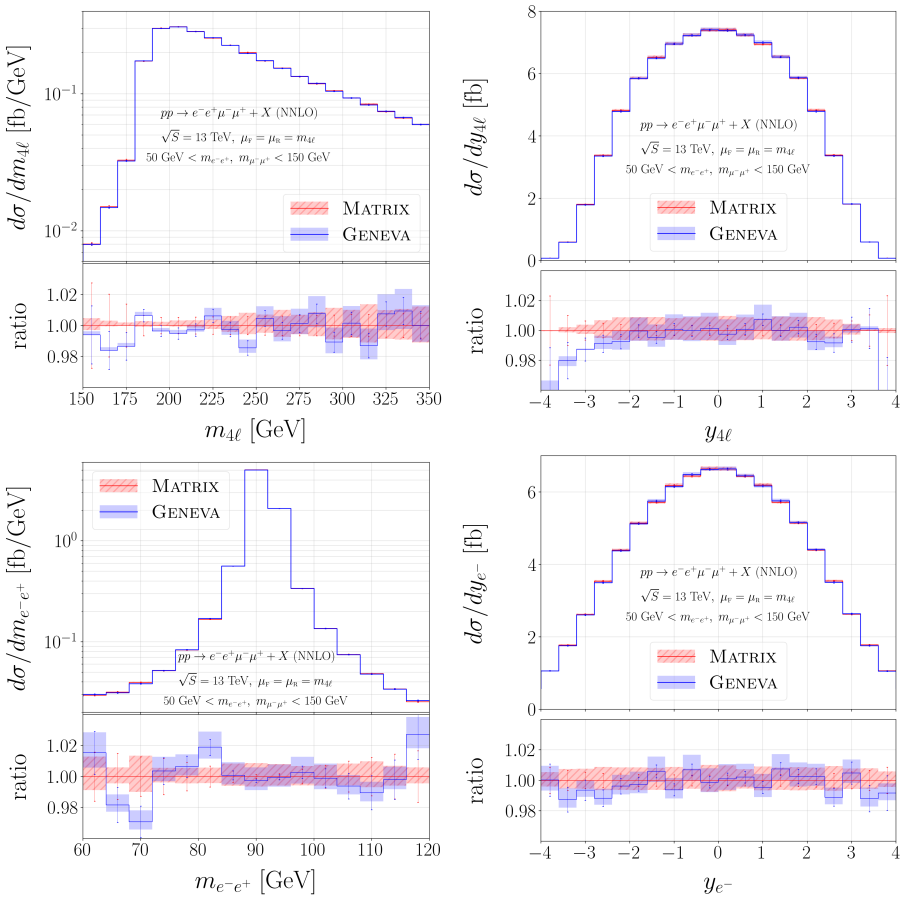

Figure 9.3: MATRIX and GENEVA NNLO distributions for the mass $m_{4\ell}$ and rapidity $y_{4\ell}$ of the 4-lepton system, the mass $m_{e^-e^+}$ of the electron-positron pair and the rapidity y_{e^-} of the electron in the process $p\,p \to e^-\,e^+\,\mu^-\,\mu^+ + X$. The bands represent the theoretical uncertainties estimated through three-point scale variations. The lower panes show the ratio between the two curves.

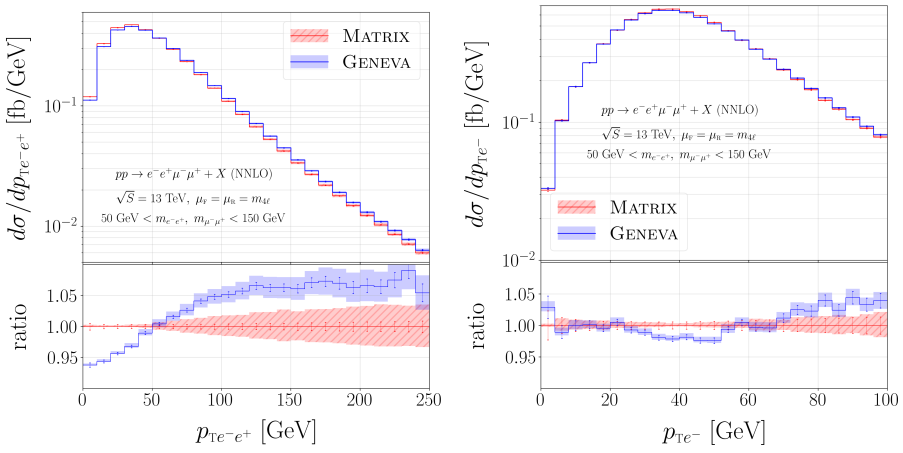

Figure 9.4: MATRIX and GENEVA NNLO distributions for the transverse momenta of the electron-positron pair ($p_{\mathrm{T}e^-e^+}$) and the electron ($p_{\mathrm{T}e^-}$) in the process $p\,p \to e^-\,e^+\,\mu^-\,\mu^+ + X$. The bands represent the theoretical uncertainties estimated through three-point scale variations. The lower panes show the ratio between the two curves.

which the effect of the resummation is larger.

Finally, in figure 9.5 we show the effects of the PYTHIA8 QCD parton shower on the mass $m_{4\ell}$ and rapidity $y_{4\ell}$ of the four-lepton system, the transverse momentum $p_{\mathrm{T}e^-e^+}$ of the electron-positron pair, and the zero-jettiness $\mathcal{T}_0$. The effects of the parton shower are small on all the inclusive distributions, as expected. Furthermore, the deviations introduced in the peak of the $\mathcal{T}_0$ distribution are numerically under control.

The same extensive checks were performed for the process where the four final-state leptons have the same flavor $p\,p \to e^-\,e^+\,e^-\,e^+ + X$.

9.5 Comparison with the experimental data

After validating the implementation of the code, we can now proceed to the comparison with the data from the ATLAS [45] and CMS [46] experiments. Differently from what we did in the previous section, in this case we let PYTHIA8 perform the QED shower, add the multiparton interactions (MPI) and perform the hadronization of the produced partons as well as the subsequent hadron decays. Following what is done in the two experimental analyses, we define the momenta of the *dressed* leptons as the sum of their naked momenta (i.e. the momentum that they have in the event) and the momenta of the photons within a radius $\Delta R_{\ell\gamma} = 0.1$ from their direction. We refrain from describing all the details of the two analyses (which can be found in the original papers), and limit ourselves to reporting the relevant phase space fiducial cuts.

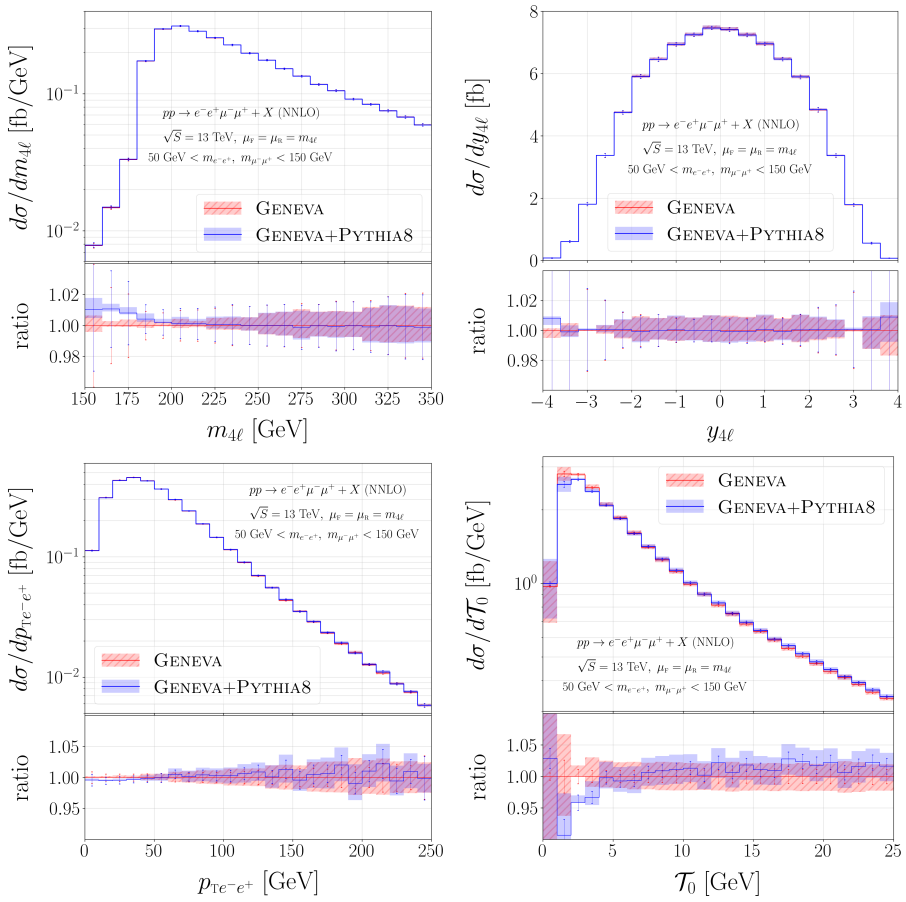

Figure 9.5: Comparison between the partonic and showered GENEVA NNLO distributions for the mass $m_{4\ell}$ and rapidity $y_{4\ell}$ of the four-lepton system, the transverse momentum $p_{\mathrm{T}e^-e^+}$ of the electron-positron pair, and the zero-jettiness $\mathcal{T}_0$ in the process $p\,p \to e^-\,e^+\,\mu^-\,\mu^+ + X$. The bands represent the theoretical uncertainties estimated through three-point scale variations. The lower panes show the ratio between the two results.

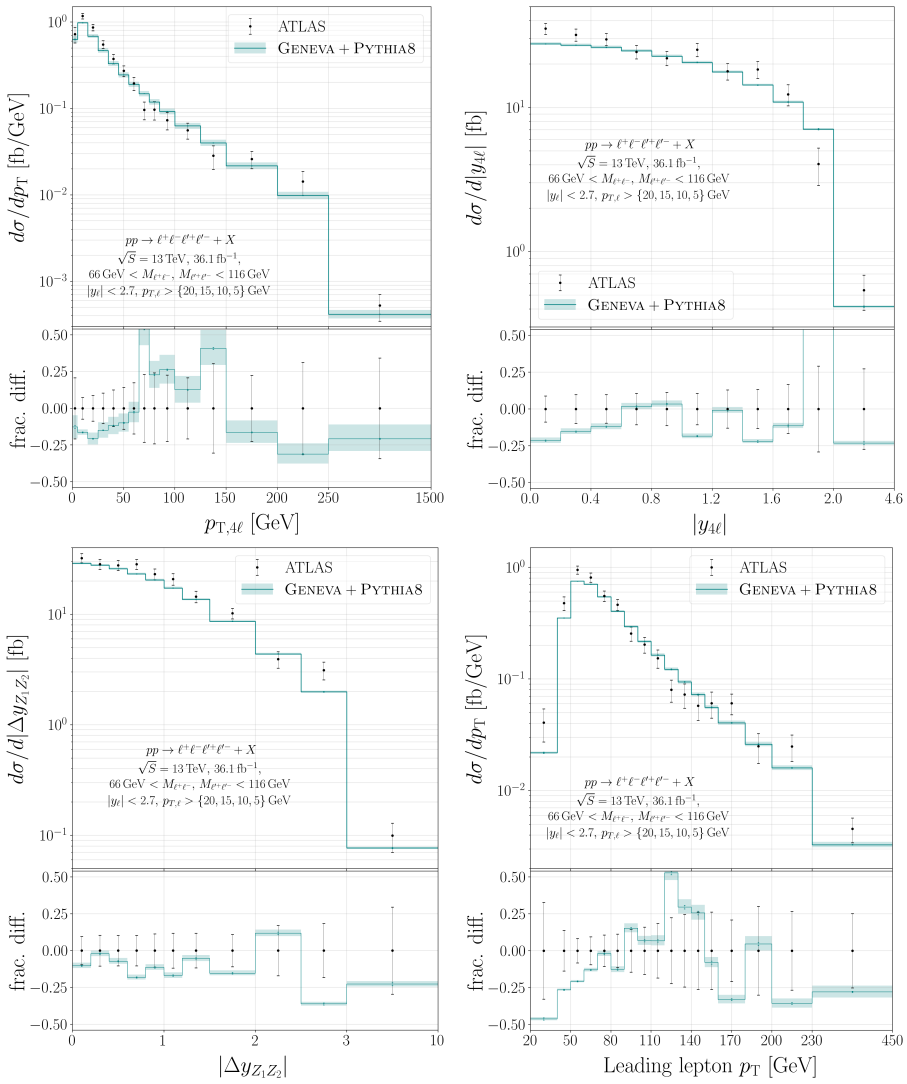

Figure 9.6: Comparison between the Geneva+Pythia8 NNLO distributions and the ATLAS experimental results [45] for the transverse momentum $p_{T,4\ell}$ of the four-lepton system, the absolute value $|y_{4\ell}|$ of the rapidity of the four-lepton system, the absolute value $|\Delta y_{Z_1 Z_2}|$ of the rapidity difference between the two reconstructed Z bosons, and the transverse momentum of the hardest lepton in the process $p\,p \to \ell^-\,\ell^+\,\ell'^-\,\ell'^+ + X$. The bands represent the theoretical uncertainties estimated through three-point scale variations. The lower panes show the ratio between the two results.

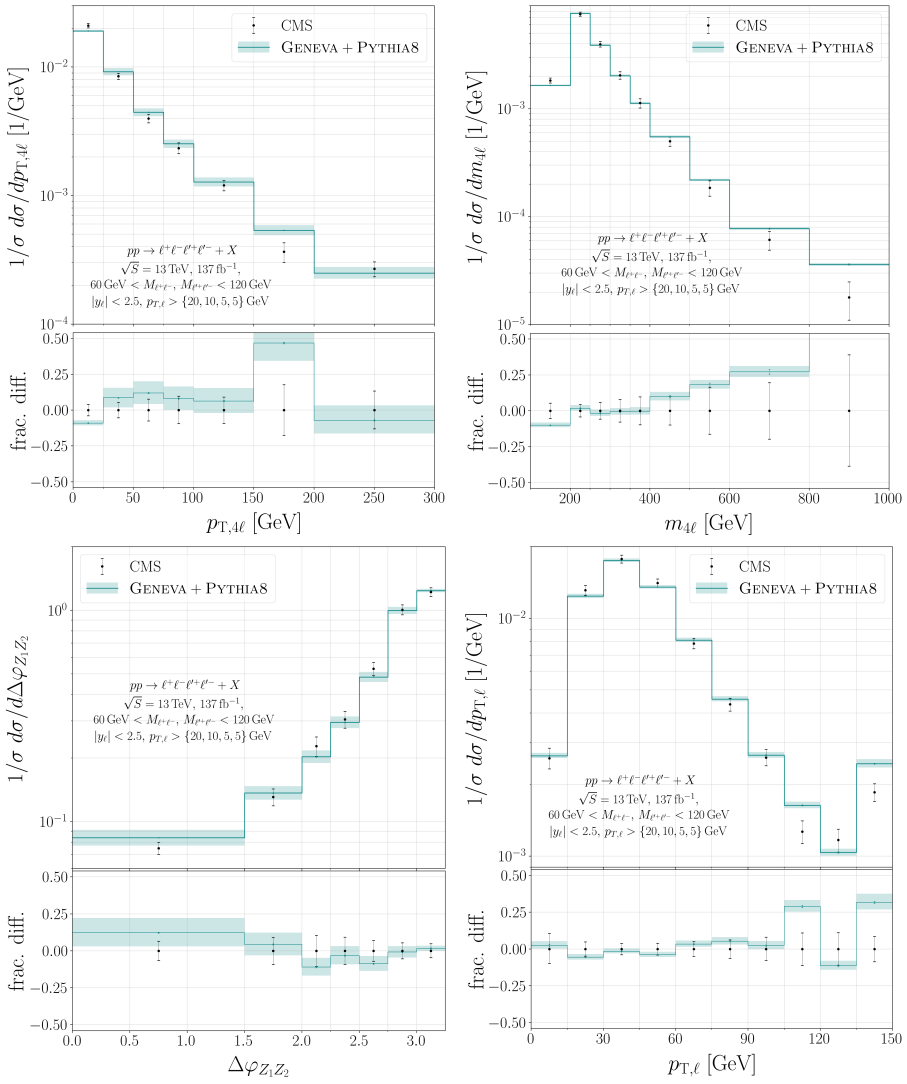

Figure 9.7: Comparison between the Geneva+Pythia8 NNLO distributions and the CMS experimental results [46] for the transverse momentum $p_{\mathrm{T},4\ell}$ of the four-lepton system, the mass $m_{4\ell}$ of the four-lepton system, the azimuthal angle $\Delta\phi_{Z_1Z_2}$ between the two reconstructed Z bosons, and the transverse momentum $p_{\mathrm{T},\ell}$ of the leptons in the process $p\,p \to \ell^-\,\ell^+\,\ell'^-\,\ell'^+ + X$. Each of the above distributions is divided by the total fiducial cross section. Furthermore, the last bin of every distribution is an overflow bin. The bands represent the theoretical uncertainties estimated through three-point scale variations. The lower panes show the ratio between the two results.

9.5.1 ATLAS

The four *hard* leptons ℓ^-, ℓ^+, ℓ'^- and ℓ'^+ are selected as those that minimize the sum

$$|m_{\ell^-\ell^+} - m_{\rm Z}| + |m_{\ell'^-\ell'^+} - m_{\rm Z}| \tag{9.13}$$

where $m_{\ell^-\ell^+}$ and $m_{\ell'^-\ell'^+}$ are the virtuality of the two pairs of same-flavor opposite-charge leptons and $m_{\rm Z} = 91.1876$ GeV. This automatically defines the momenta of the two reconstructed Z bosons Z_1 and Z_2 to be given respectively by the sums of the momenta of ℓ^- and ℓ^+ and those of ℓ'^- and ℓ'^+. Both Z_1 and Z_2 are required to have a mass between 66 and 116 GeV, and, if $\ell = \ell'$, the lepton-antilepton pairs $\ell^-\ell'^+$ and $\ell'^-\ell^+$ must have mass larger than 5 GeV. Furthermore, the four leptons of the quadruplet, ordered from the hardest to the least hard, are required to have transverse momentum larger than 20, 15, 10 and 5 GeV, respectively, and absolute value of the rapidity smaller than 2.7. Finally each same-flavor lepton pair of the quadruplet must have an angular separation $\Delta R_{\ell\ell} > 0.1$ and each opposite-flavor lepton pair of the quadruplet must have an angular separation $\Delta R_{\ell\ell'} > 0.2$.

In figure 9.6 we show the comparison between the GENEVA+PYTHIA8 NNLO distributions and the ATLAS experimental results for the transverse momentum $p_{\rm T,4\ell}$ of the four-lepton system, the absolute value $|y_{4\ell}|$ of the rapidity of the four-lepton system, the absolute value $|\Delta y_{Z_1 Z_2}|$ of the rapidity difference between the two reconstructed Z bosons, and the transverse momentum of the hardest lepton. We observe a reasonably good agreement between the theoretical predictions and the experimental results, even if the former tend to underestimate the latter in the peak regions. Such a behavior has been observed for several other event generators (see figs. 9-12 of ref. 9.6).

9.5.2 CMS

The first reconstructed Z boson (called Z_1) is chosen as the same-flavor lepton-antilepton pair $\ell^-\ell^+$ whose mass is closest to $m_{\rm Z} = 91.2$ GeV. If there are more than four leptons in the final state, the second reconstructed Z boson (called Z_2) is chosen as the remaining same-flavor lepton-antilepton pair $\ell'^-\ell'^+$ with the largest scalar sum of the transverse momenta of ℓ'^- and ℓ'^+. Both Z_1 and Z_2 are required to have a mass between 60 and 120 GeV, and, if $\ell = \ell'$, the lepton-antilepton pairs $\ell^-\ell'^+$ and $\ell'^-\ell^+$ must have mass larger than 4 GeV. Furthermore, the four leptons of the quadruplet, ordered from the hardest to the least hard, are required to have transverse momentum larger than 20, 10, 5 and 5 GeV, respectively, and absolute value of the rapidity smaller than 2.5.

In figure 9.7 we show the comparison between the GENEVA+PYTHIA8 NNLO distributions and the CMS experimental results for the transverse momentum $p_{\rm T,4\ell}$ of the four-lepton system, the mass $m_{4\ell}$ of the four-lepton system, the azimuthal angle $\Delta\phi_{Z_1 Z_2}$ between the two reconstructed Z bosons, and the transverse momentum $p_{\rm T,\ell}$ of the leptons. Each of the distributions is divided by the total fiducial cross section. Furthermore, the last bin of every distribution is an

overflow bin (i.e. it contains all the contributions up to the maximum kinematically allowed value for that observable). We observe an overall good agreement between the theoretical predictions and the experimental results, with some discrepancies in the tail of the distributions, that could be explained by the absence of higher-order EW effects.

Part II

Photon pair production with MiNNLO$_{\mathrm{PS}}$

Chapter 10

The MiNNLO$_{\rm PS}$ method

The MiNNLO$_{\rm PS}$ method [16, 17] provides a framework for building a NNLO Monte Carlo event generator and combining it with parton showers. It was born as the natural NNLO extension of the original MiNLO method [11, 12, 47], which was able to reach NLO accuracy both for the observables inclusive over radiation and those requiring a final-state jet. Calling Q and $p_{\rm T}$ the mass and transverse momentum of the color singlet respectively, the differential cross section for the production of the color singlet in the MiNNLO$_{\rm PS}$ approach is given in eq. (2) of ref. [17] and reads

$$\frac{d\sigma_{\rm CS}^{\rm MiNNLO}}{d\Phi_1} = \sum_k \frac{d}{dp_{\rm T}} \left(e^{-\tilde{S}_{k\bar{k}}(p_{\rm T})} \mathcal{L}_{k\bar{k}}(p_{\rm T}) \right) \theta(Q - p_{\rm T})\, F^{\rm corr}(\Phi_1) + R_f, \qquad (10.1)$$

where $d\Phi_1$ is the phase space for the production of the color singlet accompanied by one parton, the index k runs over the possible flavors of the initial-state partons, the Sudakov form factor $e^{-\tilde{S}_{k\bar{k}}(p_{\rm T})}$ and the luminosity factor $\mathcal{L}_{k\bar{k}}(p_{\rm T})$ provide the $p_{\rm T}$ resummation of the differential cross section and the term R_f contains all the contributions to the production of the color singlet in association with one jet that are non-singular in the $p_{\rm T} \to 0$ limit.[1] Finally, the function $F^{\rm corr}(\Phi_1)$ plays the same role of the splitting function $P_{0\to1}(\Phi_1)$ described for the GENEVA event generator: i.e. it provides a full Φ_1 dependence to a contribution that would be otherwise differential in $p_{\rm T}$ only, without spoiling the distributions that only depend on the underlying phase space $d\Phi_0$ and $p_{\rm T}$.

[1] In the implementation of the differential cross section given in eq. (10.1) in the MiNNLO$_{\rm PS}$ code, instead of using the $\theta(Q - p_{\rm T})$ function, all the logarithms $\log(Q/p_{\rm T})$ are substituted by the modified logarithms $1/p \log(1 + (Q/p_{\rm T})^p)$. If the value of p is large enough ($p \gtrapprox 3$) the differences between the two approaches in the distributions inclusive over radiation is negligible. The results of this work were obtained with the default value $p = 6$.

10.1 The resummed contribution

10.1.1 The Sudakov form factor

The expression for the exponent of the Sudakov form factor is given in eq. (2.9) of ref. [16] and reads

$$\tilde{S}_{k\bar{k}}(p_{\mathrm{T}}) = \int_{p_{\mathrm{T}}^2}^{Q^2} \frac{dq^2}{q^2} \left[A_{k\bar{k}}(q) \log\left(\frac{Q^2}{q^2}\right) + \tilde{B}_{k\bar{k}}(q) \right], \tag{10.2}$$

where

$$\begin{aligned} A_{k\bar{k}}(q) &= \frac{\alpha_{\mathrm{S}}(q)}{2\pi} A_{k\bar{k}}^{(1)} + \left(\frac{\alpha_{\mathrm{S}}(q)}{2\pi}\right)^2 A_{k\bar{k}}^{(2)} + \left(\frac{\alpha_{\mathrm{S}}(q)}{2\pi}\right)^3 A_{k\bar{k}}^{(3)} \\ \tilde{B}_{k\bar{k}}(q) &= \frac{\alpha_{\mathrm{S}}(q)}{2\pi} B_{k\bar{k}}^{(1)} + \left(\frac{\alpha_{\mathrm{S}}(q)}{2\pi}\right)^2 \tilde{B}_{k\bar{k}}^{(2)}, \end{aligned} \tag{10.3}$$

and

$$\tilde{B}_{k\bar{k}}^{(2)} = B_{k\bar{k}}^{(2)} + 2\zeta_3 \left(A_{k\bar{k}}^{(1)}\right)^2 + \frac{\beta_0}{2} H_{k\bar{k}}^{(1)}. \tag{10.4}$$

We will introduce the coefficient $H_{k\bar{k}}^{(1)}$ in the next section. Since in the following we will need the first coefficient of its α_{S} expansion, we write it as

$$\tilde{S}_{k\bar{k}}(p_{\mathrm{T}}) = \frac{\alpha_{\mathrm{S}}(p_{\mathrm{T}})}{2\pi} \tilde{S}_{k\bar{k}}^{(1)}(p_{\mathrm{T}}) + \mathcal{O}\left(\alpha_{\mathrm{S}}^2\right), \tag{10.5}$$

with

$$\tilde{S}_{k\bar{k}}^{(1)}(p_{\mathrm{T}}) = \frac{A_{k\bar{k}}^{(1)}}{2} \log^2\left(\frac{Q^2}{p_{\mathrm{T}}^2}\right) + B_{k\bar{k}}^{(1)} \log\left(\frac{Q^2}{p_{\mathrm{T}}^2}\right). \tag{10.6}$$

The expressions for the $A_{k\bar{k}}$ and $\tilde{B}_{k\bar{k}}$ coefficients appearing above can be found in eqs. (B.9) and (B.10) of ref. [16]. We limit ourselves to reporting the value of $A_{k\bar{k}}^{(1)}$ and $B_{k\bar{k}}^{(1)}$, which read

$$\begin{aligned} A_{q\bar{q}}^{(1)} &= 2C_{\mathrm{F}} \qquad & B_{q\bar{q}}^{(1)} &= -3C_{\mathrm{F}} \\ A_{gg}^{(1)} &= 2C_{\mathrm{A}} \qquad & B_{gg}^{(1)} &= -\beta_0. \end{aligned} \tag{10.7}$$

10.1.2 The luminosity factor

From eq. (23) of ref. [17], the luminosity factor $\mathcal{L}_{k\bar{k}}$ is given by the truncation to order α_{S}^2 in the expansion with respect to the strong coupling of

$$\begin{aligned} \mathcal{L}_{k\bar{k}}(p_{\mathrm{T}}) = \tilde{H}_{k\bar{k}}(p_{\mathrm{T}}) \sum_{jj'} \Big[&\left(\tilde{C}_{kj} \otimes f_j^{[a]}\right)(x_a, p_{\mathrm{T}}) \left(\tilde{C}_{\bar{k}j'} \otimes f_{j'}^{[b]}\right)(x_b, p_{\mathrm{T}}) \\ &+ \left(G_{kj} \otimes f_j^{[a]}\right)(x_a, p_{\mathrm{T}}) \left(G_{\bar{k}j'} \otimes f_{j'}^{[b]}\right)(x_b, p_{\mathrm{T}}) \Big], \end{aligned} \tag{10.8}$$

where $\tilde{H}_{k\bar{k}}(\mu)$, $\tilde{C}_{kj}(z,\mu)$ and $G_{kj}(z,\mu)$ are respectively the hard-virtual and the quark and gluon collinear coefficient functions evaluated at the renormalization and factorization scales μ, and $f_j^{[h]}(x,\mu)$ is the PDF of the parton j carrying a fraction x of the momentum of the hadron h evaluated at the factorization scale μ. Finally, the convolution operator is defined so that, given two generic functions f and g,

$$(f \otimes g)(x) = \int_x^1 \frac{dz}{z}\, f(z)\, g\Big(\frac{x}{z}\Big)\,. \tag{10.9}$$

The hard-virtual coefficient function is given by the amplitude for the production of the color singlet with no jets computed in the $\overline{\rm MS}$ subtraction scheme and can be expanded as

$$\tilde{H}_{k\bar{k}}(p_{\rm T}) = \left(\frac{\alpha_{\rm S}(p_{\rm T})}{2\pi}\right)^{n_{\rm B}} \left[H_{k\bar{k}}^{(0)} + \frac{\alpha_{\rm S}(p_{\rm T})}{2\pi}\, H_{k\bar{k}}^{(1)}(p_{\rm T}) + \left(\frac{\alpha_{\rm S}(p_{\rm T})}{2\pi}\right)^2 \tilde{H}_{k\bar{k}}^{(2)}(p_{\rm T})\right], \tag{10.10}$$

where $n_{\rm B}$ is the power of the strong coupling in the Born matrix elements of the process and

$$\tilde{H}_{k\bar{k}}^{(2)} = H_{k\bar{k}}^{(2)} - 2\zeta_3 A_{k\bar{k}}^{(1)} B_{k\bar{k}}^{(1)}. \tag{10.11}$$

The collinear coefficient functions for color-singlet production are instead process independent and their expansion with respect to the strong coupling is provided in eq. (B.16) of ref. [16]. The quark coefficient functions can be written as

$$\tilde{C}_{kj}(z,p_{\rm T}) = \delta_{kj}\,\delta(1-z) + \frac{\alpha_{\rm S}(p_{\rm T})}{2\pi}\, C_{kj}^{(1)}(z) + \left(\frac{\alpha_{\rm S}(p_{\rm T})}{2\pi}\right)^2 \tilde{C}_{kj}^{(2)}(z)\,, \tag{10.12}$$

where

$$\tilde{C}_{kj}^{(2)}(z) = C_{kj}^{(2)}(z) - 2\zeta_3 A_{k\bar{k}}^{(1)} P_{kj}^{(0)}(z)\,. \tag{10.13}$$

We will introduce the function $P_{kj}^{(0)}(z)$ in the next section. In particular, from eq. (B.17) of ref. [16] the first coefficient of the expansion reads

$$C_{kj}^{(1)}(z) = P'_{kj}(z) - C_{kk}\,\frac{\pi^2}{12}\,\delta_{kj}\,\delta(1-z)\,, \tag{10.14}$$

with the expressions for C_{kk} and $P'_{ij}(z)$ given in eqs. (3.15) and (3.24). The expansion of the gluon coefficient functions instead starts at order $\alpha_{\rm S}$ and can be written as

$$G_{kj}(z,p_{\rm T}) = \frac{\alpha_{\rm S}(p_{\rm T})}{2\pi}\, G_{kj}^{(1)}(z)\,. \tag{10.15}$$

The derivation of the additional terms proportional to ζ_3 appearing in $\tilde{B}_{k\bar{k}}^{(2)}$, $\tilde{H}_{k\bar{k}}^{(2)}$ and $\tilde{C}_{kj}^{(2)}(z)$ is provided in section 4 of ref. [16].

Expansion with respect to the strong coupling

To expand the luminosity factor of eq. (10.8) with respect to the strong coupling, we begin by writing the Dokshitzer–Gribov–Lipatov–Altarelli–Parisi (DGLAP) evolution equation [48], which reads

$$\frac{\partial f_k^{[h]}(x,\mu)}{\partial \mu} = \frac{2}{\mu}\,\frac{\alpha_{\mathrm{S}}(\mu)}{2\pi}\sum_j \Big(P_{kj}^{(0)} \otimes f_j^{[h]}\Big)(x,\mu) + \mathcal{O}\big(\alpha_{\mathrm{S}}^2\big)\,, \tag{10.16}$$

with

$$P_{kj}^{(0)}(z) = \hat{P}_{kj}^{\mathrm{AP}}(z) - \frac{B_{kk}^{(1)}}{2}\,\delta_{kj}\,\delta(1-z)\,, \tag{10.17}$$

where the coefficients $B_{kk}^{(1)}$ were given in eq. (10.7) and $\hat{P}_{kj}^{\mathrm{AP}}(z)$ are the regularized Altarelli–Parisi splitting functions defined as

$$\begin{aligned}
\hat{P}_{qq}^{\mathrm{AP}}(z) &= C_{\mathrm{F}}\,\frac{1+z^2}{(1-z)_+}\\
\hat{P}_{qg}^{\mathrm{AP}}(z) &= T_{\mathrm{F}}\left[z^2 + (1-z)^2\right]\\
\hat{P}_{gq}^{\mathrm{AP}}(z) &= C_{\mathrm{F}}\,\frac{1+(1-z)^2}{z}\\
\hat{P}_{gg}^{\mathrm{AP}}(z) &= 2C_{\mathrm{A}}\left[\frac{z}{(1-z)_+} + \frac{1-z}{z} + z\,(1-z)\right].
\end{aligned} \tag{10.18}$$

In the above equations we made use of the + distribution, which for a generic function f is defined such that

$$\int dz\,\frac{f(z)}{(1-z)_+} = \int dz\,\frac{f(z)-f(1)}{1-z}. \tag{10.19}$$

At this point, we can use the solution to the DGLAP equation

$$f_k^{[h]}(x,\mu) = f_k^{[h]}(x,p_{\mathrm{T}}) + \frac{\alpha_{\mathrm{S}}(p_{\mathrm{T}})}{2\pi}\sum_j \Big(P_{kj}^{(0)} \otimes f_j^{[h]}\Big)(x,p_{\mathrm{T}})\log\left(\frac{\mu^2}{p_{\mathrm{T}}^2}\right) + \mathcal{O}\big(\alpha_{\mathrm{S}}^2\big)\,, \tag{10.20}$$

to impose that the scale-dependent terms of the luminosity factor cancel order by order in the α_{S} expansion, so that we can write

$$\mathcal{L}_{k\bar{k}}(p_{\mathrm{T}}) = \mathcal{L}_{k\bar{k}}^{(0)}(p_{\mathrm{T}},p_{\mathrm{T}}) + \frac{\alpha_{\mathrm{S}}(p_{\mathrm{T}})}{2\pi}\,\mathcal{L}_{k\bar{k}}^{(1)}(p_{\mathrm{T}},p_{\mathrm{T}}) + \left(\frac{\alpha_{\mathrm{S}}(p_{\mathrm{T}})}{2\pi}\right)^2 \mathcal{L}_{k\bar{k}}^{(2)}(p_{\mathrm{T}},p_{\mathrm{T}})\,, \tag{10.21}$$

where the first two coefficients of the expansion read

$$\mathcal{L}^{(0)}_{k\bar{k}}(p_{\rm T},\mu) = H^{(0)}_{k\bar{k}}\, f^{[a]}_{k}(x_a,\mu)\, f^{[b]}_{\bar{k}}(x_b,\mu) \tag{10.22}$$

$$\begin{aligned}\mathcal{L}^{(1)}_{k\bar{k}}(p_{\rm T},\mu) = \Bigg\{ & H^{(0)}_{k\bar{k}} \sum_j \left[\Big(C^{(1)}_{kj} \otimes f^{[a]}_j\Big)(x_a,\mu) - \Big(P^{(0)}_{kj} \otimes f^{[a]}_j\Big)(x_a,\mu) \log\!\left(\frac{\mu^2}{p_{\rm T}^2}\right)\right] \\ & + \frac{1}{2}\, H^{(1)}_{k\bar{k}}(p_{\rm T})\, f^{[a]}_k(x_a,\mu) \Bigg\} f^{[b]}_{\bar{k}}(x_b,\mu) + (a \leftrightarrow b)\,. \end{aligned} \tag{10.23}$$

Since $e^{-\tilde{S}_{k\bar{k}}(Q)} = 1$ (see eq. (10.2)), the total $p_{\rm T}$ cumulant of the resummed contribution appearing in eq. (10.1) is given by

$$\begin{aligned}\mathcal{L}_{k\bar{k}}(Q) = & \frac{1}{2}\, H^{(0)}_{k\bar{k}}\, f^{[a]}_k(x_a,Q)\, f^{[b]}_{\bar{k}}(x_b,Q) + \frac{\alpha_{\rm S}(Q)}{2\pi} \Bigg\{ H^{(0)}_{k\bar{k}} \\ & \times \left[\sum_j \int_{x_a}^1 \frac{dz}{z}\, f^{[a]}_j\Big(\frac{x_a}{z},Q\Big)\, P'_{kj}(z) - \frac{\pi^2}{12}\, C_{kk}\, f^{[a]}_k(x_a,Q) \right] \\ & + \frac{1}{2}\, H^{(1)}_{k\bar{k}}(Q)\, f^{[a]}_k(x_a,Q) \Bigg\} f^{[b]}_{\bar{k}}(x_b,Q) + (a \leftrightarrow b) + \mathcal{O}\big(\alpha_{\rm S}^2\big)\,. \end{aligned} \tag{10.24}$$

10.2 The non-singular contribution

The non-singular contribution R_f appearing in eq. (10.1) contains the difference between the fixed-order differential cross section for the process of production of the color singlet accompanied by one jet and the expansion of the $p_{\rm T}$ resummed spectrum truncated at order $\alpha_{\rm S}^2$. To provide an explicit expression for the latter, we begin by writing the $p_{\rm T}$ spectrum of the resummed contribution as

$$\frac{d}{dp_{\rm T}} \Big(e^{-\tilde{S}_{k\bar{k}}(p_{\rm T})} \mathcal{L}_{k\bar{k}}(p_{\rm T}) \Big) = e^{-\tilde{S}_{k\bar{k}}(p_{\rm T})} D_{k\bar{k}}(p_{\rm T})\,, \tag{10.25}$$

where we have introduced

$$D_{k\bar{k}}(p_{\rm T}) = \frac{d\mathcal{L}_{k\bar{k}}}{dp_{\rm T}}(p_{\rm T}) - \mathcal{L}_{k\bar{k}}(p_{\rm T})\, \frac{d\tilde{S}_{k\bar{k}}}{dp_{\rm T}}(p_{\rm T})\,. \tag{10.26}$$

At this point, we can expand the two derivatives appearing in the above equation as

$$\begin{aligned}\frac{d\tilde{S}_{k\bar{k}}}{dp_{\rm T}}(p_{\rm T}) &= \frac{\alpha_{\rm S}(p_{\rm T})}{2\pi} \left[\frac{d\tilde{S}_{k\bar{k}}}{dp_{\rm T}}\right]^{(1)}\!\!(p_{\rm T},p_{\rm T}) + \left(\frac{\alpha_{\rm S}(p_{\rm T})}{2\pi}\right)^2 \left[\frac{d\tilde{S}_{k\bar{k}}}{dp_{\rm T}}\right]^{(2)}\!\!(p_{\rm T},p_{\rm T}) + \mathcal{O}\big(\alpha_{\rm S}^3\big) \\ \frac{d\mathcal{L}_{k\bar{k}}}{dp_{\rm T}}(p_{\rm T}) &= \frac{\alpha_{\rm S}(p_{\rm T})}{2\pi} \left[\frac{d\mathcal{L}_{k\bar{k}}}{dp_{\rm T}}\right]^{(1)}\!\!(p_{\rm T},p_{\rm T}) + \left(\frac{\alpha_{\rm S}(p_{\rm T})}{2\pi}\right)^2 \left[\frac{d\mathcal{L}_{k\bar{k}}}{dp_{\rm T}}\right]^{(2)}\!\!(p_{\rm T},p_{\rm T}) + \mathcal{O}\big(\alpha_{\rm S}^3\big)\,, \end{aligned} \tag{10.27}$$

where the first orders of the expansions reads

$$\left[\frac{d\tilde{S}_{k\bar{k}}}{dp_{\rm T}}\right]^{(1)}(p_{\rm T},\mu) = -\frac{2}{p_{\rm T}}\left[A^{(1)}_{k\bar{k}}\log\left(\frac{Q^2}{p_{\rm T}^2}\right) + B^{(1)}_{k\bar{k}}\right]$$
$$\left[\frac{d\mathcal{L}_{k\bar{k}}}{dp_{\rm T}}\right]^{(1)}(p_{\rm T},\mu) = \frac{2}{p_{\rm T}}\,H^{(0)}_{k\bar{k}}\sum_j\Big(P^{(0)}_{kj}\otimes f^{[a]}_j\Big)(x_a,\mu)\,f^{[b]}_{\bar{k}}(x_b,\mu) + (a\leftrightarrow b)\,. \tag{10.28}$$

From the above results, we can write the expansion of $D_{k\bar{k}}(p_{\rm T})$ as

$$D_{k\bar{k}}(p_{\rm T}) = \frac{\alpha_{\rm S}(p_{\rm T})}{2\pi}\,D^{(1)}_{k\bar{k}}(p_{\rm T},p_{\rm T}) + \left(\frac{\alpha_{\rm S}(p_{\rm T})}{2\pi}\right)^2 D^{(2)}_{k\bar{k}}(p_{\rm T},p_{\rm T}) + \mathcal{O}\big(\alpha_{\rm S}^3\big)\,, \tag{10.29}$$

where the first order of the expansion read

$$D^{(1)}_{k\bar{k}}(p_{\rm T},\mu) = \frac{2}{p_{\rm T}}H^{(0)}_{k\bar{k}}\Bigg\{\frac{1}{2}\left[A^{(1)}_{k\bar{k}}\log\left(\frac{Q^2}{p_{\rm T}^2}\right) + B^{(1)}_{k\bar{k}}\right] f^{[a]}_k(x_a,\mu)$$
$$+\sum_j\Big(P^{(0)}_{kj}\otimes f^{[a]}_j\Big)(x_a,\mu)\Bigg\}f^{[b]}_{\bar{k}}(x_b,\mu) + (a\leftrightarrow b)\,. \tag{10.30}$$

Finally, from the above equation the spectrum of the resummed-expanded contribution in the MiNNLO$_{\rm PS}$ method can be written as

$$\frac{d\sigma_{\rm RE}}{d\Phi_0\,dp_{\rm T}} = \frac{\alpha_{\rm S}(\mu)}{2\pi}\,\frac{2}{p_{\rm T}}\sum_k H^{(0)}_{k\bar{k}}\Bigg\{-C_{kk}\,\log\left(\frac{p_{\rm T}^2}{Q^2}\right) f^a_k(x_a,\mu)$$
$$+\sum_j\int_{x_a}^1\frac{dz}{z}\,f^a_j\Big(\frac{x_a}{z},\mu\Big)\,\hat{P}^{\rm AP}_{kj}(z)\Bigg\}f^b_{\bar{k}}(x_b,\mu) + (a\leftrightarrow b) + \mathcal{O}\big(\alpha_{\rm S}^2\big)\,. \tag{10.31}$$

The $\mathcal{O}\big(\alpha_{\rm S}^2\big)$ term of the above expression can be found in the appendix of ref. [17].

10.2.1 Modifications to the original MiNNLO$_{\rm PS}$ method

In the formulation of the MiNNLO$_{\rm PS}$ method presented in ref. [17] the expression used for the non-singular contribution is

$$R_f = \sum_k e^{-\tilde{S}_{k\bar{k}}(p_{\rm T})}\Bigg\{\frac{d\sigma^{k\bar{k},{\rm PWG}}_{\rm CS+jet}}{d\Phi_1}(p_{\rm T}) + \frac{\alpha_{\rm S}(p_{\rm T})}{2\pi}\,\tilde{S}^{(1)}_{k\bar{k}}(p_{\rm T})\,\frac{d\sigma^{k\bar{k},{\rm LO}}_{\rm CS+jet}}{d\Phi_1}(p_{\rm T})$$
$$-\left[\frac{\alpha_{\rm S}(p_{\rm T})}{2\pi}\,D^{(1)}_{k\bar{k}}(p_{\rm T},p_{\rm T}) + \left(\frac{\alpha_{\rm S}(p_{\rm T})}{2\pi}\right)^2 D^{(2)}_{k\bar{k}}(p_{\rm T},p_{\rm T})\right]F^{\rm corr}(\Phi_1)\Bigg\}. \tag{10.32}$$

In the above formula $d\sigma^{k\bar{k},{\rm LO}}_{\rm CS+jet}/d\Phi_1(\mu)$ and $d\sigma^{k\bar{k},{\rm PWG}}_{\rm CS+jet}/d\Phi_1(\mu)$ are the LO and NLO (integrated over the second QCD emission) differential cross sections for

the production of the color singlet accompanied by one jet involving partons of flavor k evaluated at renormalization and factorization scales μ. Their explicit expressions are given by the sum over the corresponding signatures of $d\sigma^{f_b,\mathrm{LO}}_{\mathrm{CS+jet}}/d\Phi_1(\mu)$ and $d\sigma^{f_b,\mathrm{PWG}}_{\mathrm{CS+jet}}/d\Phi_1(\mu)$ respectively (see eqs. (11.4) and (11.9)).

We highlight that the formula presented in eq. (10.32) is not fully expanded with respect to α_{S}, but keeps the exponentiated Sudakov form factor in front. This multiplicative approach was inherited by the original MiNLO method [11, 12]. From the numerical point of view, the presence of the Sudakov form factor increases the stability of the Monte Carlo integration of the non-singular contribution up to very small values of p_{T}, where the subtraction of the divergent terms appearing in the fixed-order and resummed-expanded contributions is not fully local in the phase space $d\Phi_1$. On the other hand, when comparing with the results from a fixed-order calculation, the Sudakov form factor and the choice of a scale $\mu = p_{\mathrm{T}}$ are sources of potential discrepancies, which, despite being formally beyond the claimed NNLO accuracy, can be numerically relevant.

In ref. [2] we presented two modifications to the above expression for R_f with the aim of minimizing the discrepancies with respect to a fixed-order calculation (where the factorization and renormalization scales are set to Q).

1. We set the scale μ to the mass of the color singlet Q, instead of its transverse momentum p_{T}.

2. We substitute the exponent $\tilde{S}_{k\bar{k}}$ of the Sudakov form factor given in eq. (10.2) with

$$\bar{S}_{k\bar{k}}(p_{\mathrm{T}}) = \int_{p_{\mathrm{T}}^2}^{Q^2} \frac{dq^2}{q^2}\,\frac{\alpha_{\mathrm{S}}(q)}{2\pi}\left[A^{(1)}_{k\bar{k}}\log\left(\frac{Q^2}{q^2}\right) + B^{(1)}_{k\bar{k}}\right], \tag{10.33}$$

   truncating the expansions with respect to the strong coupling of $A_{k\bar{k}}$ and $\tilde{B}_{k\bar{k}}$ at the first order.

After these two modifications, the expression for R_f presented in eq. (10.32) is substituted by

$$\begin{aligned} R_f = \sum_k e^{-\bar{S}_{k\bar{k}}(p_{\mathrm{T}})}\Bigg\{ & \frac{d\sigma^{k\bar{k},\mathrm{PWG}}_{\mathrm{CS+jet}}}{d\Phi_1}(Q) + \frac{\alpha_{\mathrm{S}}(Q)}{2\pi}\,\tilde{S}^{(1)}_{k\bar{k}}(p_{\mathrm{T}})\,\frac{d\sigma^{k\bar{k},\mathrm{LO}}_{\mathrm{CS+jet}}}{d\Phi_1}(Q) \\ & - \left[\frac{\alpha_{\mathrm{S}}(Q)}{2\pi}\,D^{(1)}_{k\bar{k}}(p_{\mathrm{T}},Q) + \left(\frac{\alpha_{\mathrm{S}}(Q)}{2\pi}\right)^2 D^{(2)}_{k\bar{k}}(p_{\mathrm{T}},Q)\right] F^{\mathrm{corr}}(\Phi_1)\Bigg\}. \end{aligned} \tag{10.34}$$

Validation of the modified method

The difference between the two formulations is beyond the claimed NNLO accuracy and are expected to be numerically negligible for processes where the size of the non-singular contributions is small compared to the total cross section. To check this, we applied the modified MiNNLO$_{\mathrm{PS}}$ method to the processes of

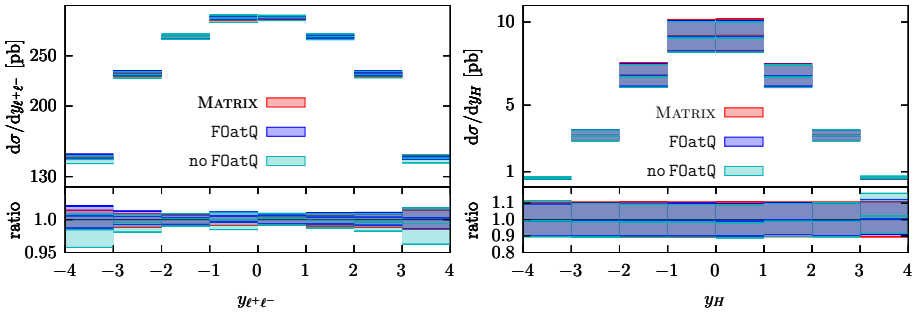

Figure 10.1: Comparison between the predictions from the fixed-order calculation implemented in MATRIX and the *Les Houches* partonic events generated by the POWHEG BOX RES with the original and modified formulations of the MiNNLO$_{\text{PS}}$ method for the rapidity of the color singlet for the processes of Drell-Yan ($y_{\ell^+\ell^-}$) and Higgs (y_H) production. The original and modified MiNNLO$_{\text{PS}}$ formulations are labeled respectively `no FOatQ` and `FOatQ`. The bands represent the estimated theoretical uncertainties of the distributions. In the lower panes of the figures, the ratio between the two curves is shown.

Drell-Yan and Higgs boson production and compared the results with those obtained with the original method and presented in ref. [17]. For each of the three processes (Drell-Yan, Higgs boson and $\gamma\gamma$ production) we compared the total NNLO cross section σ^{NNLO} to the resummed contribution alone σ^{res} given by the integral of the first term of eq. (10.1) (the non-singular contributions are given by the difference of the two terms), finding

$$\begin{aligned}
\sigma^{\text{NNLO}}_{\text{DY}} &= 1919 \pm 1 \text{ pb} & \sigma^{\text{res}}_{\text{DY}} &= 1904 \pm 3 \text{ pb} \\
\sigma^{\text{NNLO}}_{\text{H}} &= 39.64 \pm 0.01 \text{ pb} & \sigma^{\text{res}}_{\text{H}} &= 34.03 \pm 0.07 \text{ pb} \\
\sigma^{\text{NNLO}}_{\gamma\gamma} &= 155.7 \pm 1.0 \text{ pb} & \sigma^{\text{res}}_{\gamma\gamma} &= 55.7 \pm 0.6 \text{ pb}.
\end{aligned} \tag{10.35}$$

For diphoton production, $\sigma^{\text{res}}_{\gamma\gamma}$ contributes to only about one third of the total cross section, at difference with Drell-Yan and Higgs boson production, thereby justifying the choices made in this chapter. As a further validation, in figure 10.1 we compare the rapidity distribution of the color singlet obtained with the original and new formulations (labeled respectively as `no FOatQ` and `FOatQ`) for Drell-Yan and Higgs boson production. The MiNNLO$_{\text{PS}}$ distributions shown in the figure are from the POWHEG partonic events (often called *Les Houches* events). Furthermore, we show the NNLO results from the fixed-order calculation implemented in the public version of the MATRIX code [41], where the renormalization and factorization scales have been set to the mass of the color singlet Q. For this comparison only, we use the same PDF sets used in ref. [17]. The curves show a very good agreement between the NNLO and the MiNNLO$_{\text{PS}}$ results obtained with both the formulations, both for the central scale and the uncertainty band. In particular, since the Drell-Yan process features a very

small perturbative uncertainty band, the remarkable agreement between the NNLO and `FOatQ` curves displayed in the left pane of figure 10.1 represents a robust validation of the new formulation of the MiNNLO$_{\rm PS}$ method.

Chapter 11

The Powheg method

The generation of the events according to eq. (10.1) relies on the POWHEG BOX Monte Carlo event generator [10], which also provides the resummation of the transverse momentum of the second emission appearing in the NLO differential cross section $d\sigma^{k\bar{k},\mathrm{PWG}}_{\mathrm{CS+jet}}/d\Phi_1$ (from now on $d\sigma^{\mathrm{PWG}}_{\mathrm{CS+jet}}/d\Phi_1$) for the production of the color singlet accompanied by one jet. To give a brief introduction to the POWHEG method, discussed in details in refs. [8] and [9], we begin by describing how the Φ_2 configurations are mapped into the phase space $d\Phi_1$.

The amplitude of a Φ_2 configuration diverges in the limit of small relative transverse momentum k_{T} between any couple of partons that represents a valid QCD splitting. This results in a maximum of three divergent regions α_r that we call [0,1], [0,2] and [1,2] parametrized respectively by the transverse momentum of the first ($k_{\mathrm{T}}^{[0,1]}$) or second ($k_{\mathrm{T}}^{[0,2]}$) final-state parton with respect to the beam or the relative transverse momentum $k_{\mathrm{T}}^{[1,2]}$ between the two final-state partons. Instead of assigning a fixed projection to every Φ_2 configuration, the POWHEG BOX event generator divides the contribution from every real signature f_r into one contribution from every divergent α_r region given by

$$\frac{d\sigma^{\alpha_r,\mathrm{LO}}_{\mathrm{CS+2jet}}}{d\Phi_2} = \frac{d\sigma^{f_r,\mathrm{LO}}_{\mathrm{CS+2jet}}}{d\Phi_2}\, f^{\alpha_r}(\Phi_2)\,. \tag{11.1}$$

with the aid of a function f^{α_r} such that

$$\sum_{\alpha_r | f_r} f^{\alpha_r}(\Phi_2) = 1 \qquad\qquad \lim_{k_{\mathrm{T}}^{\alpha_r}\to 0} \frac{d\sigma^{\alpha_r,\mathrm{LO}}_{\mathrm{CS+2jet}}}{d\Phi_2} = \frac{d\sigma^{f_r,\mathrm{LO}}_{\mathrm{CS+2jet}}}{d\Phi_2}. \tag{11.2}$$

This guarantees that each contribution $d\sigma^{f_r,\mathrm{LO}}_{\mathrm{CS+2jet}}/d\Phi_2$ is divergent in one α_r region only. At this point, a different mapping is defined for every contribution following the requirements of infrared safety. This allows us to write the NLO cross section for the process as

$$\sigma^{\mathrm{NLO}}_{\mathrm{CS+jet}} = \sum_{f_b} \int d\Phi_1 \, \frac{d\sigma^{f_b,\mathrm{NLO}}_{\mathrm{CS+jet}}}{d\Phi_1}, \tag{11.3}$$

where $d\sigma^{f_b,\mathrm{NLO}}_{\mathrm{CS+jet}}/d\Phi_1$ contains the integral over the Φ_2 configurations from the α_r contributions whose projection is the configuration Φ_1 with signature f_b.

At this point we introduce several definitions to comply with the standard POWHEG notation. We call the LO and NLO differential cross section for the production of the color singlet accompanied by one jet respectively

$$B^{f_b}(\Phi_1) = \frac{d\sigma^{f_b,\mathrm{LO}}_{\mathrm{CS+jet}}}{d\Phi_1} \qquad \bar{B}^{f_b}(\Phi_1) = \frac{d\sigma^{f_b,\mathrm{NLO}}_{\mathrm{CS+jet}}}{d\Phi_1}, \tag{11.4}$$

and the LO differential cross section for the production of the color singlet accompanied by two jets associated to the singular region α_r

$$R^{\alpha_r}(\Phi_2) = \frac{d\sigma^{\alpha_r,\mathrm{LO}}_{\mathrm{CS+2jet}}}{d\Phi_2}. \tag{11.5}$$

From eq. (4.17) of ref. [9], the POWHEG master formula for the differential cross section for the production of a color singlet accompanied by one jet reads

$$\begin{aligned} d\sigma^{\mathrm{PWG}}_{\mathrm{CS+jet}} = \sum_{f_b} \bar{B}^{f_b}(\Phi_1)\, d\Phi_1 \Bigg[& \Delta^{f_b}(\Phi_1, k_{\mathrm{T}}^{\mathrm{cut}}) \\ & + \sum_{\alpha_r | f_b} \frac{R^{\alpha_r}(\Phi_2)}{B^{f_b}(\Phi_1)}\, \Delta^{f_b}(\Phi_1, k_{\mathrm{T}}^{\alpha_r})\, \theta(k_{\mathrm{T}}^{\alpha_r} - k_{\mathrm{T}}^{\mathrm{cut}})\, \frac{d\Phi_2}{d\Phi_1} \Bigg], \end{aligned} \tag{11.6}$$

where $k_{\mathrm{T}}^{\mathrm{cut}}$ is a resolution parameter (i.e. the Φ_2 configurations with $k_{\mathrm{T}} < k_{\mathrm{T}}^{\mathrm{cut}}$ are considered unresolved and only contribute to the generation of Φ_1 events), and, from eq. (4.16) of the same reference, the POWHEG Sudakov form factor is defined as

$$\Delta^{f_b}(\Phi_1, k_{\mathrm{T}}) = \exp\left(- \sum_{\alpha_r | f_b} \int \frac{d\Phi_2}{d\Phi_1}\, \frac{R^{\alpha_r}(\Phi_2)}{B^{f_b}(\Phi_1)}\, \theta(k_{\mathrm{T}}^{\alpha_r} - k_{\mathrm{T}}) \right). \tag{11.7}$$

The term in the square brackets of eq. (11.6) implements the resummation of the relative transverse momentum of the second emitted parton with a multiplicative approach. The unitarity of the approach is guaranteed by the fact that

$$\Delta^{f_b}(\Phi_1, k_{\mathrm{T}}^{\mathrm{cut}}) + \int \frac{d\Phi_2}{d\Phi_1} \sum_{\alpha_r | f_b} \frac{R^{\alpha_r}(\Phi_2)}{B^{f_b}(\Phi_1)}\, \Delta^{f_b}(\Phi_1, k_{\mathrm{T}})\, \theta(k_{\mathrm{T}} - k_{\mathrm{T}}^{\mathrm{cut}}) = 1, \tag{11.8}$$

which allows us to write

$$\frac{d\sigma^{f_b,\mathrm{PWG}}_{\mathrm{CS+jet}}}{d\Phi_1} = \frac{d\sigma^{f_b,\mathrm{NLO}}_{\mathrm{CS+jet}}}{d\Phi_1} = \bar{B}^{f_b}(\Phi_1)\,. \tag{11.9}$$

Chapter 12

Handling of the QED singularities

Any event generator that aims to reach more than LO accuracy in QCD needs to rely on $\Phi_{n+1} \to \Phi_n$ mappings between phase spaces $d\Phi_{n+1}$ and $d\Phi_n$ with different parton multiplicities. Indeed, the presence of infrared QCD singularities makes it necessary to combine contributions with different number of final-state partons in the differential cross section of the same event. In general, because of that, among the observables that are inclusive over the QCD radiation, only the distributions of those that are preserved by all the mappings can be in exact agreement with those obtained from a fixed-order calculation. All the others may display deviations that are power-suppressed functions of the transverse momentum k_{T} of the radiation (i.e. they vanish in the limit of small k_{T}, where the requirement of infrared safety forces the observable to have the same value when evaluated at both Φ_n and Φ_{n+1}).

However, in the case of production of a photon pair, the picture is complicated by the presence of QED divergences, which lead to two additional problems.

1. The configurations that are far from every QED singular region should not be mapped into configurations close to a QED singular region, and viceversa. If that was not the case, events that are not discarded at the analysis level could receive contributions from unphysical divergent amplitudes, or events that are discarded could carry physical contributions. The requirement can be lifted if the contributions from such configurations are given a strong kinematic suppression.

2. The generation of events which are close to the QED singular regions should be suppressed to keep the event generator efficient.

Furthermore, we would like to avoid introducing any hard cut or isolation criteria at the generation level, leaving the user free to apply their own ones at the analysis level.

12.1 $1 \to 0$ mapping

The projection that we use is determined by the requirements that it preserves

1. The mass of the color singlet.
2. The rapidity of the color singlet.
3. The direction of one of the photons in the laboratory frame.

By doing this we make sure that QED-finite configurations with one final-state parton are not projected to singular configurations with no final-state partons. As far as the MiNNLO$_{\rm PS}$ formulae are concerned, we would just need to define a $1 \to 0$ mapping that projects the Φ_1 configurations to the Φ_0 ones. Nonetheless, we will also introduce its inverse, namely a function that, given a Φ_0 configuration and three additional radiation variables, associates to them a Φ_1 configuration. In practice, we have implemented such function in the code and use it to generate the $d\Phi_1$ phase space from the $d\Phi_0$ one. After doing that, we save the original Φ_0 configuration, so that we do not need to project it later. This represents also a very strong check of the correctness of the mapping.

12.1.1 Preservation of mass and rapidity of the diphoton

To preserve the mass and rapidity of the diphoton, we can use the formulae for the FKS mapping, already discussed in chapter 6. In the laboratory frame of Φ_0 the diphoton mass and rapidity read

$$m_{\gamma\gamma} = \sqrt{S\bar{x}_a\bar{x}_b} \qquad y_{\gamma\gamma} = \frac{1}{2}\log\left(\frac{\bar{x}_a}{\bar{x}_b}\right), \tag{12.1}$$

where S is the squared hadronic center-of-mass energy and $\bar{x}_a$ and $\bar{x}_b$ are the fractions of hadronic momenta carried by the two partons that undergo the hard interaction.

In the partonic center-of-mass frame of Φ_1 instead the momentum of the final-state parton can be written in terms of the FKS variables ξ, y and ϕ as

$$p_j = \frac{\sqrt{s}}{2}\,\xi\left(1, \sqrt{1-y^2}\,\sin\phi, \sqrt{1-y^2}\,\cos\phi, y\right), \tag{12.2}$$

where s is the squared partonic center-of-mass energy of the system. In such a frame the momentum of the diphoton in Φ_1 then reads

$$p_{\gamma\gamma} = \frac{\sqrt{s}}{2}\left(2-\xi, -\xi\sqrt{1-y^2}\,\sin\phi, -\xi\sqrt{1-y^2}\,\cos\phi, -\xi\, y\right) \tag{12.3}$$

and its mass and rapidity are given by

$$m_{\gamma\gamma} = \sqrt{s\,(1-\xi)} \qquad y^{\rm CM}_{\gamma\gamma} = \frac{1}{2}\log\left(\frac{2-\xi\,(1+y)}{2-\xi\,(1-y)}\right). \tag{12.4}$$

Introducing x_a and x_b as the fractions of hadronic momenta carried by the two partons that undergo the hard interaction so that $s = S x_a x_b$, we can finally write the mass and rapidity of the diphoton in the laboratory frame as

$$m_{\gamma\gamma} = \sqrt{S x_a x_b \left(1-\xi\right)} \qquad y_{\gamma\gamma} = \frac{1}{2}\left[\log\left(\frac{x_a}{x_b}\right) + \log\left(\frac{2-\xi\left(1+y\right)}{2-\xi\left(1-y\right)}\right)\right]. \tag{12.5}$$

By equating the expressions of eqs. (12.5) and (12.1), we find the relation between $\bar{x}_a$, $\bar{x}_b$ and x_a, x_b to be

$$\begin{cases} x_a = \dfrac{\bar{x}_a}{\sqrt{1-\xi}}\sqrt{\dfrac{2-\xi\left(1-y\right)}{2-\xi\left(1+y\right)}} \\ x_b = \dfrac{\bar{x}_b}{\sqrt{1-\xi}}\sqrt{\dfrac{2-\xi\left(1+y\right)}{2-\xi\left(1-y\right)}}. \end{cases} \tag{12.6}$$

12.1.2 Preservation of the direction of one photon

Instead of simply boosting the momenta of the Φ_0 diphoton system to give them the total momentum of eq. (12.3), as in the FKS mapping, we now want to enforce the preservation of the direction of one photon. To do that, we need to express the momenta of Φ_0 and Φ_1 in two frames where the diphoton system has the same rapidity. We choose to work in the partonic center-of-mass frame of Φ_1 because in such a frame the Φ_1 momenta have simple expressions (see eqs. (12.2) and (12.3)).

After writing the momenta of the two photons of the configuration Φ_0 in their center-of-mass frame as

$$\begin{cases} \bar{p}_{\gamma_1} = \dfrac{m_{\gamma\gamma}}{2}\left(1, \sin\bar{\theta}\sin\bar{\phi}, \sin\bar{\theta}\cos\bar{\phi}, \cos\bar{\theta}\right) \\ \bar{p}_{\gamma_2} = \dfrac{m_{\gamma\gamma}}{2}\left(1, -\sin\bar{\theta}\sin\bar{\phi}, -\sin\bar{\theta}\cos\bar{\phi}, -\cos\bar{\theta}\right) \end{cases} \tag{12.7}$$

we apply a longitudinal boost with rapidity (12.4) and arrive to

$$\begin{cases} \vec{p}'_{\gamma_1} = \dfrac{m_{\gamma\gamma}}{2}\left(\dfrac{2-\xi-\xi y\cos\bar{\theta}}{\sqrt{\left(2-\xi\right)^2-\xi^2y^2}}, \sin\bar{\theta}\sin\bar{\phi}, \sin\bar{\theta}\cos\bar{\phi}, \dfrac{\left(2-\xi\right)\cos\bar{\theta}-\xi y}{\sqrt{\left(2-\xi\right)^2-\xi^2y^2}}\right) \\ \vec{p}'_{\gamma_2} = \dfrac{m_{\gamma\gamma}}{2}\left(\dfrac{2-\xi+\xi y\cos\bar{\theta}}{\sqrt{\left(2-\xi\right)^2-\xi^2y^2}}, -\sin\bar{\theta}\sin\bar{\phi}, -\sin\bar{\theta}\cos\bar{\phi}, \dfrac{-\left(2-\xi\right)\cos\bar{\theta}-\xi y}{\sqrt{\left(2-\xi\right)^2-\xi^2y^2}}\right). \end{cases} \tag{12.8}$$

At this point, we can impose that the momentum p_{γ_1} of the configuration Φ_1 in the partonic center-of-mass frame has the same direction of $\vec{p}'_{\gamma_1}$. To do that,

we introduce the dimensionless parameter $\mathcal{E}$ and write p_{γ_1} as

$$p_{\gamma_1} = \mathcal{E}\,\sqrt{s}\left(\frac{2-\xi-\xi y\cos\bar{\theta}}{\sqrt{(2-\xi)^2-\xi^2y^2}}, \sin\bar{\theta}\sin\bar{\phi}, \sin\bar{\theta}\cos\bar{\phi}, \frac{(2-\xi)\cos\bar{\theta}-\xi y}{\sqrt{(2-\xi)^2-\xi^2y^2}}\right). \tag{12.9}$$

Finally, we fix the value of $\mathcal{E}$ by imposing that the second photon, whose momentum reads

$$\begin{aligned} p_{\gamma_2} = \sqrt{s}\Bigg(1-\frac{\xi}{2}-\mathcal{E}\,\frac{2-\xi-\xi y\cos\bar{\theta}}{\sqrt{(2-\xi)^2-\xi^2y^2}}, -\frac{\xi}{2}\sqrt{1-y^2}\,\sin\phi-\mathcal{E}\sin\bar{\theta}\sin\bar{\phi}, \\ -\frac{\xi}{2}\sqrt{1-y^2}\,\cos\phi-\mathcal{E}\sin\bar{\theta}\cos\bar{\phi}, -\frac{\xi y}{2}-\mathcal{E}\,\frac{(2-\xi)\cos\bar{\theta}-\xi y}{\sqrt{(2-\xi)^2-\xi^2y^2}}\Bigg), \end{aligned} \tag{12.10}$$

is massless, which imposes

$$\mathcal{E} = \frac{1-\xi}{\sqrt{(2-\xi)^2-\xi^2y^2}+\xi\sqrt{1-y^2}\,\sin\bar{\theta}\cos(\phi-\bar{\phi})}. \tag{12.11}$$

12.1.3 Jacobian

To implement the generation of the $d\Phi_1$ phase space using $\bar{x}_a$, $\bar{x}_b$, $\bar{\theta}$ and $\bar{\phi}$ along with the FKS variables ξ, y and ϕ, we still need to compute analytically the Jacobian of the transformation, which, using eqs. (6.12) and (12.6), can be written as

$$\frac{d\Phi_1}{d\bar{x}_a\,d\bar{x}_b\,d\xi\,dy\,d\phi\,d\cos\bar{\theta}\,d\bar{\phi}} = \frac{S\bar{x}_a\bar{x}_b}{(4\pi)^3}\,\frac{\xi}{(1-\xi)^2}\,\frac{d\Phi_{\gamma\gamma}}{d\cos\bar{\theta}\,d\bar{\phi}}. \tag{12.12}$$

Since $d\Phi_{\gamma\gamma}$ is a Lorentz invariant, we can compute it in any suitable reference frame. In particular, if we call θ' and ϕ' the polar angles of one photon in the center-of-mass frame of the diphoton system, we can write

$$d\Phi_{\gamma\gamma} = \frac{d\cos\theta'\,d\phi'}{32\pi^2}, \tag{12.13}$$

so that we are left with computing the value of

$$J = \frac{d\cos\theta'\,d\phi'}{d\cos\bar{\theta}\,d\bar{\phi}}. \tag{12.14}$$

To do that, we need to find the sequence of boosts that take the momenta of the two photons from the partonic center-of-mass frame of Φ_1 to the center-of-mass frame of the diphoton system. We begin by performing a longitudinal boost on

the momentum p_{γ_1} given in eq. (12.9) to the frame where the diphoton system has zero longitudinal rapidity. Using the expression for $y^{\rm CM}_{\gamma\gamma}$ given in eq. (12.4), we find that in such a frame

$$p'_{\gamma_1} = \mathcal{E}\,\sqrt{s}\,\left(1,\,\sin\bar{\theta}\sin\bar{\phi},\,\sin\bar{\theta}\cos\bar{\phi},\,\cos\bar{\theta}\right). \tag{12.15}$$

Since in this frame the momentum of the photon pair reads

$$p_{\gamma\gamma} = \frac{\sqrt{s}}{2}\left(\sqrt{(2-\xi)^2-\xi^2y^2},\,-\xi\,\sqrt{1-y^2}\,\sin\phi,\,-\xi\,\sqrt{1-y^2}\,\cos\phi,\,0\right), \tag{12.16}$$

to get to the diphoton rest frame, we need to perform a transverse boost with velocity

$$v_{\rm T} = \frac{\xi\sqrt{1-y^2}}{\sqrt{(2-\xi)^2-\xi^2y^2}}\,(\sin\phi,\,\cos\phi,\,0)\,, \tag{12.17}$$

after which the spatial components of the four-vector representing the momentum of the photon become

$$\vec{p}_{\gamma_1} = \frac{m_{\gamma\gamma}}{2}\,\frac{\mathcal{E}}{1-\xi}\left(A\sin\phi + B\cos\phi,\,A\cos\phi - B\sin\phi,\,2\sqrt{1-\xi}\cos\bar{\theta}\right), \tag{12.18}$$

where we have introduced, for ease of notation, the two auxiliary variables

$$\begin{cases} A = \sqrt{(2-\xi)^2-\xi^2y^2}\,\sin\bar{\theta}\cos\big(\phi-\bar{\phi}\big) + \xi\sqrt{1-y^2} \\ B = 2\sqrt{1-\xi}\sin\bar{\theta}\sin\big(\phi-\bar{\phi}\big)\,. \end{cases} \tag{12.19}$$

Finally, we need to equate the result of eq. (12.18) to

$$\vec{p}_{\gamma_1} = \frac{m_{\gamma\gamma}}{2}\,(\sin\theta'\sin\phi',\,\sin\theta'\cos\phi',\,\cos\theta')\,, \tag{12.20}$$

which imposes

$$\begin{cases} \cos\theta' = \dfrac{2\mathcal{E}\cos\bar{\theta}}{\sqrt{1-\xi}} \\ \tan\phi' = \dfrac{A\sin\phi + B\cos\phi}{A\cos\phi - B\sin\phi}, \end{cases} \tag{12.21}$$

so that finally the expression for J reads

$$J = \frac{4\,(1-\xi)}{\left[\sqrt{(2-\xi)^2-\xi^2y^2} + \xi\sqrt{1-y^2}\sin\bar{\theta}\cos\big(\bar{\phi}-\phi\big)\right]^2}. \tag{12.22}$$

12.2 The damping function

The formula presented in eq. (11.6) cannot be directly applied to the process of photon pair production, since events that are far from every QED singular region (and thus not discarded by the analysis) could still receive contributions from divergent amplitudes through the $\bar{B}^{f_b}$ function. In this section, we describe a general way to deal with processes that present QED divergences at the Born level within the POWHEG formalism, with the aim of generating events without introducing any phase space cuts or photon isolation criteria at the generation level.[1]

So far, for every real signature f_r, we have divided the real contribution R^{f_r} into up to three terms R^{α_r}, so that each of them is divergent in one $k_{\mathrm{T}}^{\alpha_r} \to 0$ limit only. We now further split R^{α_r} as

$$R^{\alpha_r} = R^{\alpha_r}_{\mathrm{QED}} + R^{\alpha_r}_{\mathrm{QCD}}, \tag{12.23}$$

so that $R^{\alpha_r}_{\mathrm{QED}}$ is divergent in the QED singular regions, but QCD finite, and viceversa. To do this, we introduce the damping function $F^{\alpha_r}(\Phi_2)$ and define

$$R^{\alpha_r}_{\mathrm{QCD}} = F^{\alpha_r}\, R^{\alpha_r} \qquad\qquad R^{\alpha_r}_{\mathrm{QED}} = (1 - F^{\alpha_r})\, R^{\alpha_r}. \tag{12.24}$$

The explicit expression for the damping function is given by

$$F^{\alpha_r} = \frac{\left(\dfrac{1}{d_{\alpha_r}}\right)^p}{\left(\dfrac{1}{d_{\alpha_r}}\right)^p + \displaystyle\sum_{i=1}^{n_{\mathrm{c}}} \sum_{j=1}^{n_\gamma} \left(\dfrac{1}{d_{[c_i,\gamma_j]}}\right)^p}, \tag{12.25}$$

where

$$d_{[i,j]} = \begin{cases} p_{\mathrm{T}j}^2 & \text{if } i \text{ is an initial-state particle,} \\ 2\min\bigl(E_i^2, E_j^2\bigr)\,(1 - \cos\theta_{ij}) & \text{if } i \text{ and } j \text{ are final-state particles,} \end{cases} \tag{12.26}$$

and the sum in the denominator runs over the n_{c} massless charged particles and the n_γ photons. In eq. (12.26), p is a positive real number, $p_{\mathrm{T}j}$ and E_j are the transverse momentum and energy of the particle j, and θ_{ij} the angle between the particles i and j, everything computed in the partonic center-of-mass frame. The reason why we have not used the invariant mass of the ij pair in the definition of $d_{[i,j]}$ in the case where i and j are both final-state partons is to ensure that in the soft limits $d_{[i,j]}$ has the same scaling with respect to the energy of the radiated parton both in the initial- and final-state case.

At this point, after a few modifications to the formula provided in eq. (11.6), the POWHEG differential cross section for the production of a photon pair accom-

[1] To the best of our knowledge, a similar procedure was first used in ref. [49].

panied by one jet can be written as

$$d\sigma^{\mathrm{PWG}}_{\gamma\gamma+\mathrm{jet}} = \sum_{f_b} \bar{B}^{f_b}_{\mathrm{QCD}}(\Phi_1)\, d\Phi_1 \left[\Delta^{f_b}_{\mathrm{QCD}}(\Phi_1, k_{\mathrm{T}}^{\mathrm{cut}}) + \sum_{\alpha_r | f_b} \frac{R^{\alpha_r}_{\mathrm{QCD}}(\Phi_2)}{B^{f_b}(\Phi_1)}\, \Delta^{f_b}_{\mathrm{QCD}}(\Phi_1, k_{\mathrm{T}}^{\alpha_r}) \times \theta(k_{\mathrm{T}}^{\alpha_r} - k_{\mathrm{T}}^{\mathrm{cut}})\, \frac{d\Phi_2}{d\Phi_1} \right] + \sum_{\alpha_r} R^{\alpha_r}_{\mathrm{QED}}(\Phi_2)\, d\Phi_2, \tag{12.27}$$

where the contributions from $R^{\alpha_r}_{\mathrm{QED}}(\Phi_2)$ are now considered to be unprojectable and therefore not included in $\bar{B}^{f_b}_{\mathrm{QCD}}(\Phi_1)$, and the new POWHEG Sudakov form factor reads

$$\Delta^{f_b}_{\mathrm{QCD}}(\Phi_1, k_{\mathrm{T}}) = \exp\left(- \sum_{\alpha_r | f_b} \int \frac{d\Phi_2}{d\Phi_1}\, \frac{R^{\alpha_r}_{\mathrm{QCD}}(\Phi_2)}{B^{f_b}(\Phi_1)}\, \theta(k_{\mathrm{T}}^{\alpha_r} - k_{\mathrm{T}}) \right). \tag{12.28}$$

We now want to show that the method we have just introduced satisfies the first requirement made in the above section. First, we have to show that it prevents Φ_2 configurations that are far from every QED singular regions from being mapped into Φ_1 configurations that are close to a QED singular region, to avoid generating Φ_2 events from a divergent $\bar{B}^{f_b}(\Phi_1)$. Let us consider a Φ_2 configuration where the closest QED splitting is characterized by a transverse momentum $k_{\mathrm{T}}^{\mathrm{QED}}$. There are two possibilities.

1. The closest singularity is due to QCD (i.e. $k_{\mathrm{T}}^{\alpha_r} < k_{\mathrm{T}}^{\mathrm{QED}}$). Since the mapping is expected to change the momenta of the particles involved in the QED splitting by an amount of order $k_{\mathrm{T}}^{\alpha_r} < k_{\mathrm{T}}^{\mathrm{QED}}$, such QED-finite Φ_2 configurations are not expected to be projected to QED-singular Φ_1 configurations.

2. The closest singularity is due to QED (i.e. $k_{\mathrm{T}}^{\mathrm{QED}} < k_{\mathrm{T}}^{\alpha_r}$). In this case there is the possibility that the projected Φ_1 configuration carries a QED-divergent contribution proportional to

$$B^{f_b} \propto \frac{1}{E_\gamma^2}\, \frac{1}{\theta^2_{\gamma q}} \sim \frac{1}{d_{\gamma q}}. \tag{12.29}$$

   However, in the QED-singular limit the damping function provides a kinematic suppression proportional to

$$F^{\alpha_r} \sim \left(\frac{d_{\gamma q}}{d_{\alpha_r}} \right)^p. \tag{12.30}$$

   Even though B^{f_b} and F^{α_r} are computed using momenta belonging to configurations with different multiplicities, by choosing a large enough value for p we can guarantee that the contributions from the regions close to the QED divergence are negligible. In our case $p = 2$ has proven to be an adequate choice.

Finally, we have to show that $\bar{B}^{f_b}(\Phi_1)$ does not take divergent contributions from Φ_2 configurations that are close to a QED singularity. This is again guaranteed by the fact that the Φ_2 configurations that are close to a QED divergence (i.e. have $k_{\mathrm{T}}^{\mathrm{QED}} < k_{\mathrm{T}}^{\alpha_r}$) are given a kinematic suppression inside $\bar{B}^{f_b}(\Phi_1)$ proportional to

$$F^{\alpha_r} \sim \left(\frac{d_{\gamma q}}{d_{\alpha_r}}\right)^p. \tag{12.31}$$

12.2.1 The suppression factors

With the method described in the previous section, we have made sure that all the events that pass the analysis cuts do not receive contributions from configurations that are too close to the QED singular regions (and thus non physical). We are still left with the problem that the differential cross section presented in eq. (12.27) is not integrable over the entire $d\Phi_1$ phase space due to the QED singularities. A way to solve this problem would be to implement the same cuts that we adopt in the analysis at the generation level. However, unless the cut is made on an observable preserved by the mappings, we would risk to discard configurations that would have contributed to events that are kept by the analysis. To avoid this problem, we could still apply generation cuts that are much tighter than the analysis one, but we would lose efficiency generating a lot of events that are finally discarded. To avoid this, the POWHEG BOX event generator offers the possibility of applying two suppression factors $S_B(\Phi_1)$ and $S_R(\Phi_1)$ to $\bar{B}^{f_b}(\Phi_1)$ and $R^{\alpha_r}(\Phi_2)$ respectively, to make the product $S_B\bar{B}^{f_b}$ and $S_R R^{\alpha_r}$ integrable over the entire phase space. The physical distribution is finally recovered by giving to the event a weight $1/S_B$ or $1/S_R$. The explicit expressions we use for the two suppression factors are

$$S_B = \frac{p^a_{\mathrm{T}\gamma_1}}{p^a_{\mathrm{T}\gamma_1}+\bar{p}^a_{\mathrm{T}\gamma}}\frac{p^a_{\mathrm{T}\gamma_2}}{p^a_{\mathrm{T}\gamma_2}+\bar{p}^a_{\mathrm{T}\gamma}}\frac{R^a_{j_1\gamma_1}}{R^a_{j_1\gamma_1}+\bar{R}^a_{j\gamma}}\frac{R^a_{j_1\gamma_2}}{R^a_{j_1\gamma_2}+\bar{R}^a_{j\gamma}}, \tag{12.32}$$

and

$$S_R = \frac{p^a_{\mathrm{T}\gamma_1}}{p^a_{\mathrm{T}\gamma_1}+\bar{p}^a_{\mathrm{T}\gamma}}\frac{p^a_{\mathrm{T}\gamma_2}}{p^a_{\mathrm{T}\gamma_2}+\bar{p}^a_{\mathrm{T}\gamma}}\frac{R^a_{j_1\gamma_1}}{R^a_{j_1\gamma_1}+\bar{R}^a_{j\gamma}}\frac{R^a_{j_1\gamma_2}}{R^a_{j_1\gamma_2}+\bar{R}^a_{j\gamma}}\frac{R^a_{j_2\gamma_1}}{R^a_{j_2\gamma_1}+\bar{R}^a_{j\gamma}}\frac{R^a_{j_2\gamma_2}}{R^a_{j_2\gamma_2}+\bar{R}^a_{j\gamma}}, \tag{12.33}$$

where $p_{\mathrm{T}i}$ is the transverse momentum of the particle i with respect to the beam axis, and R_{ij} the angular distance between the particles i and j in the azimuth-pseudorapidity plane

$$R_{ij} = \sqrt{(\eta_i-\eta_j)^2+(\phi_i-\phi_j)^2}. \tag{12.34}$$

In our simulation we have set

$$\bar{p}_{\mathrm{T}\gamma} = 22\ \mathrm{GeV} \qquad \bar{R}_{j\gamma} = 0.4 \qquad a = 1. \tag{12.35}$$

Chapter 13

Phenomenological results

13.1 Physical parameters

The phenomenological results presented in this chapter were obtained for a proton-proton collider with a hadronic center-of-mass energy $\sqrt{S} = 13$ TeV. We used the LHAPDF [34] PDF set `NNPDF31_nnlo_as_0118` and the evolution of α_s provided by the same package. The electromagnetic coupling for the final-state photons has been set to $\alpha = 1/137$, and the mass of the top quark to $m_t = 173.2$ GeV.

We apply the photon isolation prescription of Ref. [50] to the two final-state photons. For each photon, we compute the angular distance $R_{i\gamma}$ with respect to the i-th final-state parton. We discard the event unless, for every photon and every $R < R_c$,

$$\sum_{i=1}^{n_{\text{part}}} p_{Ti}\,\theta(R - R_{i\gamma}) < E_T^{\text{max}}\,\chi(R)\,, \tag{13.1}$$

where n_{part} is the number of final-state partons, p_{Ti} is the transverse momentum of i with respect to the beam, and

$$\chi(R) = \left(\frac{1-\cos R}{1-\cos R_{\text{cone}}}\right)^n. \tag{13.2}$$

In our analysis, we have set

$$E_T^{\text{max}} = 4 \text{ GeV} \qquad R_{\text{cone}} = 0.4 \qquad n = 1. \tag{13.3}$$

In addition, the two photons have to fulfill

$$p_{T\gamma_1} > p_{T\gamma_1}^{\text{min}}, \qquad p_{T\gamma_2} > p_{T\gamma_2}^{\text{min}}, \qquad m_{\gamma\gamma} > m_{\gamma\gamma}^{\text{min}}, \tag{13.4}$$

where $p_{T\gamma_1}$ and $p_{T\gamma_1}$ are the transverse momenta of the hardest and next-to-hardest photons, and $m_{\gamma\gamma}$ is the mass of the photon pair, and

$$p_{T\gamma_1}^{\text{min}} = 25 \text{ GeV}, \qquad p_{T\gamma_2}^{\text{min}} = 22 \text{ GeV}, \qquad m_{\gamma\gamma}^{\text{min}} = 25 \text{ GeV}. \tag{13.5}$$

13.2 Matrix elements

The matrix elements for the process $p\,p \to \gamma\,\gamma\,j$ at NLO in QCD were obtained from OpenLoops2 [33, 42, 43, 51, 52]. The two-loop amplitudes for $q\,\bar{q} \to \gamma\,\gamma$ have instead been taken from refs. [53, 54] and implemented into the code. We work in the approximation of 5 light quarks, and neglect the contributions given by two-loop diagrams with one massive loop. We consider instead the contributions given by top-quark loops in the single-loop diagrams for the process $p\,p \to \gamma\,\gamma\,j$.

When comparing with the experimental results from the LHC we include in our predictions the LO contribution from the gluon-initiated process of production of a photon pair through a closed quark loop $g\,g \to \gamma\,\gamma$, which, besides being of the same order $\alpha_{\rm s}^2$ of the NNLO corrections to the quark-initiated process discussed so far, is further enhanced by the sizable gluon luminosity at the LHC. The analytic amplitudes for this process were taken from ref. [55] and implemented in the Powheg Box Res framework after neglecting the top-quark loop contribution, which amounts for at most a few percent in the kinematic distributions we are showing (see e.g. figure 3 of ref. [56]).

13.3 Validation of the code

To validate the implementation of our code, we compared some distributions of phenomenological interest against those produced with the NNLO fixed-order calculation implemented in the public version of the Matrix code [41, 57, 42, 58, 53, 59, 60]. The two predictions are theoretically expected to agree up to terms beyond the NNLO accuracy.

The Matrix results presented in this section were obtained setting the slicing parameter $r_{\rm cut} = 0.0005$ (i.e. they neglect non-singular contributions with $p_{\rm T} < 0.0005\,Q$)[1] and the renormalization and factorization scales equal to the mass of the photon pair $\mu_{\rm R} = \mu_{\rm F} = Q$. The theoretical uncertainty was estimated via a seven-point scale variation obtained by multiplying and dividing the central renormalization and factorization scales by a factor 2. Furthermore, we used the PDFs, fiducial cuts and isolation criterion reported in the previous section.

The central values of the Matrix and MiNNLO$_{\rm PS}$ total cross sections are in agreement within the statistical errors and read respectively[2]

$$\sigma_{\gamma\gamma}^{\rm Matrix} = 155.7 \pm 1.0 \text{ pb} \qquad \sigma_{\gamma\gamma}^{\rm MiNNLO} = 154.9 \pm 0.2 \text{ pb}, \tag{13.6}$$

while the corresponding theoretical uncertainties are given by[3]

$$\sigma_{\gamma\gamma}^{\rm Matrix} = 155.7\,^{+5\%}_{-4\%} \text{ pb} \qquad \sigma_{\gamma\gamma}^{\rm MiNNLO} = 154.9\,^{+6\%}_{-5\%} \text{ pb}. \tag{13.7}$$

[1] Matrix also provides extrapolated results for the total cross section down to $r_{\rm cut} = 0$. However, the extrapolation makes the statistical error much larger, so that we prefer to limit ourselves to the comparison with the results for the lowest non-zero $r_{\rm cut}$ value.

[2] The extrapolated value for the total cross section is equal to $\sigma_{\gamma\gamma}^{\rm Matrix} = 153.9 \pm 1.9$ pb.

[3] The extrapolated theoretical uncertainty is equal to $\sigma_{\gamma\gamma}^{\rm Matrix} = 153.9\,^{+4\%}_{-4\%}$ pb.

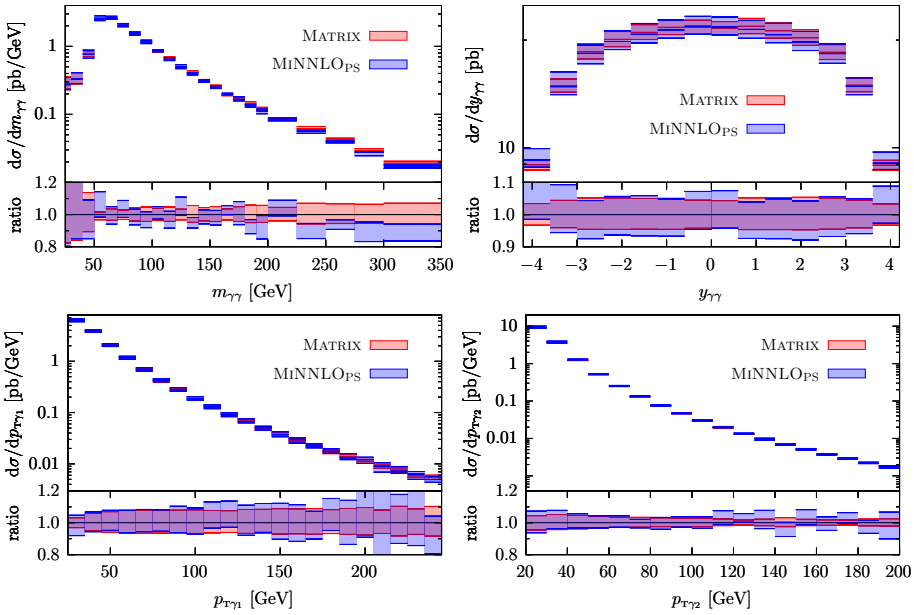

Figure 13.1: Comparison between the predictions from the fixed-order calculation implemented in MATRIX and MiNNLOPS for the mass $m_{\gamma\gamma}$ and rapidity $y_{\gamma\gamma}$ of the photon pair, and the transverse momentum of the hardest ($p_{\mathrm{T}\gamma_1}$) and second-to-hardest ($p_{\mathrm{T}\gamma_2}$) photons. The bands represent the estimated theoretical uncertainties of the distributions. In the lower panes of the figures, the ratio between the two curves is shown.

Both the results are in agreement with each other.

Finally, in figure 13.1 we compare the distributions of the mass $m_{\gamma\gamma}$ and rapidity $y_{\gamma\gamma}$ of the photon pair, and the transverse momentum of the hardest ($p_{\mathrm{T}\gamma_1}$) and second-to-hardest ($p_{\mathrm{T}\gamma_2}$) photons along with the corresponding estimated theoretical uncertainties. We find an overall good agreement between the MATRIX and MiNNLOPS curves, and a compatible size for the scale-variation bands. We ascribe the difference in the high-$m_{\gamma\gamma}$ region to effects beyond the NNLO accuracy of our result.

13.4 Distribution of the partonic events

To study the phenomenology of the process, we generated about 16 million events without any generation cuts apart from imposing a minimum mass of the photon pair of 10 GeV. Since the mass of the photon pair is preserved by all the mappings that we use, this generation cut has no effects on the final distributions as long as it is smaller than the fiducial cut on the mass of the

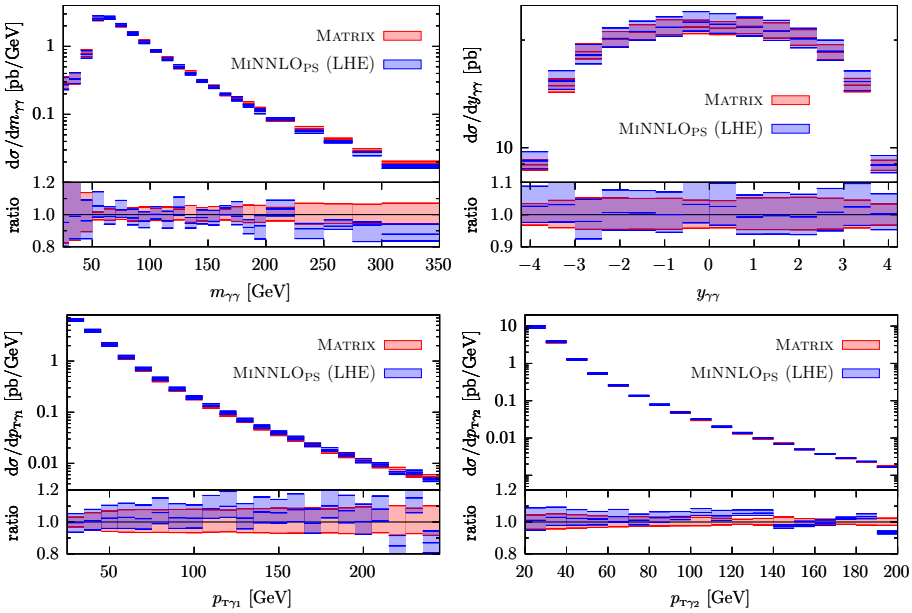

Figure 13.2: Comparison between the predictions from the fixed-order calculation implemented in MATRIX and the *Les Houches* partonic events generated by the POWHEG BOX RES for the mass $m_{\gamma\gamma}$ and rapidity $y_{\gamma\gamma}$ of the photon pair, and the transverse momentum of the hardest ($p_{\mathrm{T}\gamma_1}$) and second-to-hardest ($p_{\mathrm{T}\gamma_2}$) photons. The bands represent the estimated theoretical uncertainties of the distributions. In the lower panes of the figures, the ratio between the two curves is shown.

photon pair $m_{\gamma\gamma}^{\mathrm{min}}$. Except for this constraint, the events can then be used for making predictions with arbitrary fiducial cuts.

We begin by comparing the distributions obtained from the POWHEG partonic events (often denoted as *Les Houches* events) with the MATRIX predictions. In figure 13.2 we show the distributions of the mass $m_{\gamma\gamma}$ and rapidity $y_{\gamma\gamma}$ of the photon pair, and the transverse momentum of the hardest ($p_{\mathrm{T}\gamma_1}$) and second-to-hardest ($p_{\mathrm{T}\gamma_2}$) photons. We observe a good agreement between the two predictions, both for the central value and the estimated theoretical uncertainties. At variance with similar comparisons for other processes not involving photons, this is not trivial due to the presence of an isolation criterion in the definition of the cross section of the process.

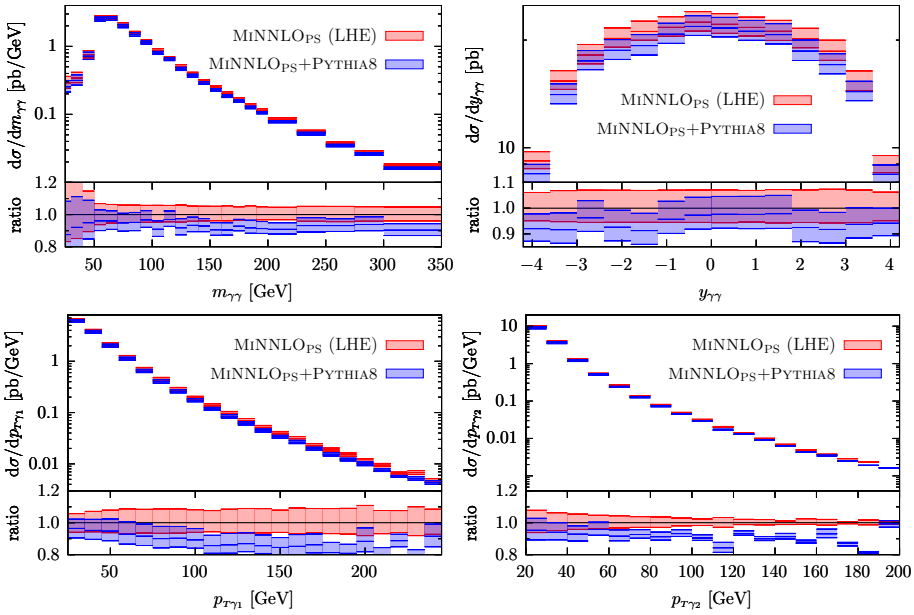

Figure 13.3: Comparison between the distributions obtained from the generated events before and after the Pythia8 parton shower for the mass $m_{\gamma\gamma}$ and rapidity $y_{\gamma\gamma}$ of the photon pair, and the transverse momentum of the hardest ($p_{\mathrm{T}\gamma_1}$) and second-to-hardest ($p_{\mathrm{T}\gamma_2}$) photons. The bands represent the estimated theoretical uncertainties of the distributions. In the lower panes of the figures, the ratio between the two curves is shown.

13.5 Distributions after the parton shower

After comparing the distributions of the partonic events with the fixed-order calculation, we now want to study the effects on the same distributions of the parton shower performed by Pythia8 [61, 62].

To interface Pythia8 to the Powheg Box Res event generator, we rely on the `main31` configuration file (distributed with Pythia8). The results presented in this section were obtained after switching off multiparton interactions (MPI), QED radiation and hadronization effects, and using the Monash tune presented in ref. [63]. Furthermore, we set the Pythia8 parameter `POWHEG:pThard` to 2 (i.e. we used the prescription introduced in section 4 of ref. [64]), and the `SpaceShower:dipoleRecoil` to 1.[4]

In figure 13.3 we compare the distributions obtained from the generated events before and after the Pythia8 parton shower for the mass $m_{\gamma\gamma}$ and rapidity

[4] In the LO contribution from the gluon-initiated process (included only in the comparison with data) the upper limit for the transverse momentum of the shower evolution is set equal to the mass of the photon pair.

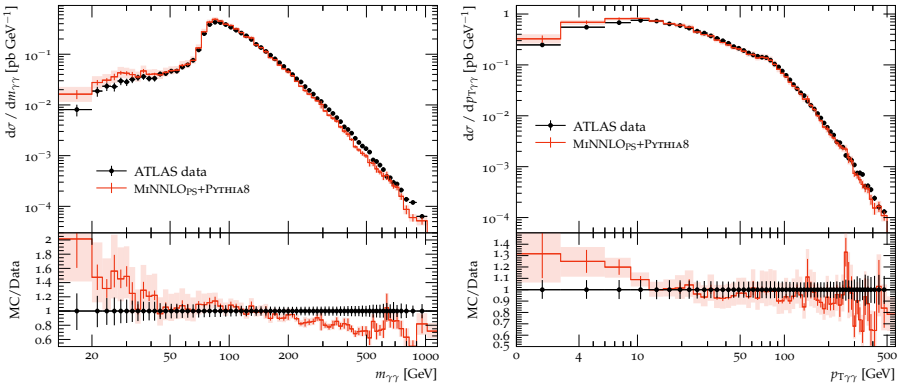

Figure 13.4: Comparison between the NNLO+PS predictions from MiNNLO$_{\text{PS}}$ combined with Pythia8 and the ATLAS data for the mass $m_{\gamma\gamma}$ and transverse momentum $p_{\text{T}\gamma\gamma}$ of the photon pair. The bands and the bars represent respectively the estimated theoretical and statistical uncertainties of the distributions. In the lower panes of the figures, the ratio between the two curves is shown.

$y_{\gamma\gamma}$ of the photon pair, and the transverse momentum of the hardest ($p_{\text{T}\gamma_1}$) and second-to-hardest ($p_{\text{T}\gamma_2}$) photons. We observe a reduction of around 5–10% of the cross sections after the parton shower, especially in the region of high transverse momenta of the two photons. We ascribe this behavior to the fact that, with the increased multiplicity of the partonic activity, the photons in the events after the parton shower are less likely to satisfy the isolation criterion, thus leading to a smaller cross section. We observed the same pattern also in a fully independent (and significantly simpler) code implementing QCD NLO+PS diphoton production in the Powheg Box Res. A similar behavior was observed also in ref. [65].

13.6 Comparison with the ATLAS results

We conclude the discussion on the phenomenology of the process by comparing the NNLO+PS predictions obtained combining MiNNLO$_{\text{PS}}$ with the Pythia8 parton shower to the experimental results presented by the ATLAS collaboration in ref. [66]. To do this, we rely on the analysis provided by Rivet [67]. As discussed above, to make a better comparison with the data, we add to the NNLO-accurate MiNNLO$_{\text{PS}}$ results for the process $q\,\bar{q} \to \gamma\,\gamma$ the LO contribution from the gluon-initiated process $g\,g \to \gamma\,\gamma$. Since there are no interferences among the Feynman diagrams of the two processes up to order α_{S}^2 we compute the final distributions by simply adding the results from the two calculations for every bin of the histograms and combining the errors in quadrature.

The ATLAS results were obtained at a hadronic center-of-mass energy $\sqrt{S} =$

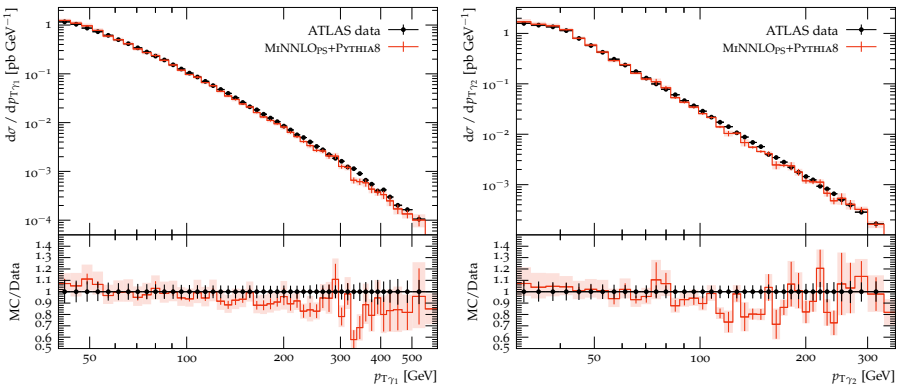

Figure 13.5: Comparison between the NNLO+PS predictions from MiNNLO$_{\rm PS}$ combined with Pythia8 and the ATLAS data for the transverse momentum of the hardest ($p_{\rm T\gamma_1}$) and second-to-hardest ($p_{\rm T\gamma_2}$) photons. The bands and the bars represent respectively the estimated theoretical and statistical uncertainties of the distributions. In the lower panes of the figures, the ratio between the two curves is shown.

13 TeV, with a fiducial volume defined by the requirements that

$$p_{\rm T\gamma_1} > 40 \text{ GeV} \qquad p_{\rm T\gamma_2} > 30 \text{ GeV} \qquad \Delta R_{\gamma\gamma} > 0.4 \tag{13.8}$$

and

$$|y_{\gamma_i}| < 1.37 \qquad 1.52 < |y_{\gamma_i}| < 2.37 \qquad i = 1, 2, \tag{13.9}$$

where $p_{\rm T\gamma_1}$ and $p_{\rm T\gamma_2}$ are the transverse momenta of the hardest and second-to-hardest photons, $\Delta R_{\gamma\gamma}$ is the angular distance between the two photons as defined in eq. (12.34), and y_{γ_i} is the rapidity of the i-th photon. Furthermore, the photon-isolation criterion described in section 4.1 of ref. [66] is applied.

In figure 13.4 we show the distributions for the mass $m_{\gamma\gamma}$ and transverse momentum $p_{\rm T\gamma\gamma}$ of the photon pair. We find a good agreement between the data and theoretical predictions throughout the entire range of the $p_{\rm T\gamma\gamma}$ distribution and in the bulk of the cross section for the $m_{\gamma\gamma}$ distribution. Given the cuts of eqs. (13.8) and (13.9), the region where $m_{\gamma\gamma} < 80$ GeV is populated only by $\gamma\gamma$ accompanied by at least one jet, making our result only NLO accurate, as confirmed also by the wider uncertainty bands. For $m_{\gamma\gamma} < 40$ GeV, the MiNNLO$_{\rm PS}$ results overshoot ATLAS data by an amount compatible with what has been observed, for other predictions of similar accuracy, in ref. [66]. The fact that this region is characterized by a large NLO K-factor [68] hints at the possibility that the inclusion of higher-order corrections will improve the agreement with data. At large $m_{\gamma\gamma}$ values we observe differences up to about 15%, which might be due to higher-order contributions. Top-quark mass effects above the threshold $m_{\gamma\gamma} \simeq 2m_{\rm t}$, that we are neglecting in the quark-induced

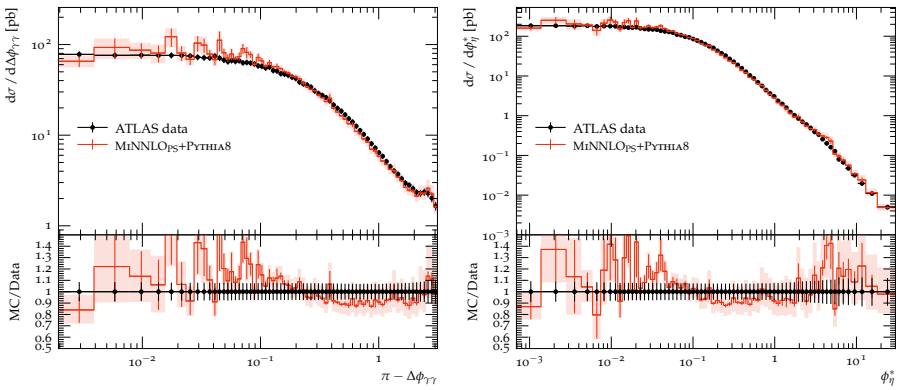

Figure 13.6: Comparison between the NNLO+PS predictions from MiNNLO$_{\rm PS}$ combined with Pythia8 and the ATLAS data for the azimuthal separation of the two photons $\Delta\phi_{\gamma\gamma}$ and ϕ^*_η (see the definition in eq. (13.10)). The bands and the bars represent respectively the estimated theoretical and statistical uncertainties of the distributions. In the lower panes of the figures, the ratio between the two curves is shown.

2-loop amplitudes as well as in the $g\,g \to \gamma\,\gamma$ channel, can also induce differences at the percent level.

In figure 13.5 instead we show the distributions for the transverse momenta of the hardest ($p_{\rm T\gamma_1}$) and second-to-hardest ($p_{\rm T\gamma_2}$) photons, for which we find a good agreement between the data and theoretical predictions.

Finally, in figure 13.6 we show the distributions of two angular observables: the azimuthal separation $\Delta\phi_{\gamma\gamma}$ of the two photons and ϕ^*_η, defined as

$$\phi^*_\eta = \tan\left(\frac{\pi - \Delta\phi_{\gamma\gamma}}{2}\right)\sqrt{1 - \left(\tanh\frac{\Delta y_{\gamma\gamma}}{2}\right)^2}, \tag{13.10}$$

where $\Delta y_{\gamma\gamma}$ is the rapidity difference between the two photons. Such a variable, first introduced for Drell-Yan processes in ref. [69], while being sensitive to the same dynamics governing the $p_{\rm T}$ spectrum, allows for a better resolution at small values of $p_{\rm T}$. The agreement between the data and the theoretical predictions is rather good on the whole range of the two distributions.

Chapter 14

Conclusions

In this thesis, I've presented the implementations of two processes of boson pair production in two different Monte Carlo event generators: GENEVA and MINNLO$_{\text{PS}}$+POWHEG BOX. Despite sharing the same formal NNLO QCD accuracy, the two methods are different from each other. While the MINNLO$_{\text{PS}}$ approach relies on the p_{T} resummation, both for the transverse momentum of the first and the second jet (the latter is performed through the POWHEG method), the GENEVA event generator is natively based on the $\mathcal{T}_N$ resummation (although the method itself is independent from the type of resummation and has also been used with the p_{T} resummation [19]).

The matching between the resummation and the fixed-order matrix elements is also performed differently in two different event generators. The GENEVA method follows an additive approach, where the resummed and fixed-order $\mathcal{T}_0$ spectra are added to each other after subtracting the expansion of the resummed term to avoid double counting. This method is in principle cleaner, since, for every underlying configuration Φ_0 the resummed and resummed-expanded total cumulants exactly cancel each other, thus making the distribution of every observable that is preserved by both the $1 \to 0$ and $2 \to 1$ phase-space mappings (e.g. the mass and rapidity of the color singlet) identical to that obtained from a fixed-order calculation. However, in the actual implementation of the code the above statement is spoiled by the missing non-singular NNLO contributions for the configurations with $\mathcal{T}_0 < \mathcal{T}_0^{\text{cut}}$, whose computation would require the implementation of a NNLO local infrared subtraction. By choosing a small value for $\mathcal{T}_0^{\text{cut}}$, the size of such contributions can be typically reduced to be of the order of or smaller than 1% of the total cross section, but cannot be completely removed since a too small $\mathcal{T}_0^{\text{cut}}$ would make the calculation numerically unstable. If the result from an independent NNLO fixed-order calculation is available, the generated events can be reweighted so as to recover the correct integrated cross section.

The MINNLO$_{\text{PS}}$+POWHEG BOX event generator follows instead a multiplicative approach, building on the original MINLO method [11, 12]. The presence of on overall Sudakov form factor that exponentially suppresses any infrared diver-

gence in the limit of small p_{T} allows to avoid introducing any resolution cut, thus formally including all the NNLO contributions in the calculation. The downside resides in the appearance of spurious terms beyond the claimed NNLO accuracy, which, despite being formally subleading, can become numerically relevant, as was the case for the process of study.

Due to their complexity, every quantum field theory calculation of phenomenological interest heavily relies on several approximations. The availability of different NNLO QCD Monte Carlo event generators is an important tool for better quantifying the effect of some of these approximations and to provide a more accurate estimate of the theoretical uncertainties associated to the calculation. The direct comparison between the distributions produced by the two event generators goes beyond the scope of this thesis. Nonetheless it could be an interesting topic for future works.

Appendix A

The $2 \to 1$ mapping (q_{T} preserving)

A.1 Direct mapping

The q_{T}-preserving $2 \to 1$ mapping implemented in GENEVA is defined under the conditions that it preserves

1. The fully recursive zero-jettiness $\mathcal{T}_0^{\mathrm{FR}}$.
2. The momenta q_i of the particles belonging to the color singlet.

A.1.1 Same Hemisphere ISRA and FSRA

We can treat together the *Same Hemisphere ISRA* and *FSRA* cases since they share the same expressions for the fully-recursive zero-jettiness (see eqs. (7.11) and (7.19)) and the underlying zero-jettiness computed on the projected Φ_1 configuration, given in eqs. (7.12) and (7.20). By imposing that the two expressions are equal and from the equations of momentum conservation, the formulae for $\bar{p}_1$, $\bar{x}_a$ and $\bar{x}_b$ read

$$\begin{cases} \hat{\bar{p}}_1^+ = \hat{p}_{12}^+ \\ \hat{\bar{p}}_1^- = \dfrac{p_{12\mathrm{T}}^2}{\hat{p}_{12}^+} \\ \vec{\bar{p}}_{1\mathrm{T}} = \vec{p}_{12\mathrm{T}} \end{cases} \qquad \begin{cases} \bar{x}_a = x_a - \dfrac{e^{y_{\mathrm{CS}}}}{\sqrt{S}} \left(\hat{p}_{12}^- - \dfrac{p_{12\mathrm{T}}^2}{\hat{p}_{12}^+} \right) \\ \bar{x}_b = x_b, \end{cases} \tag{A.1}$$

where we called $S = (P_a + P_b)^2$.

A.1.2 Opposite Hemisphere ISRA

Following the same steps as above, the mapping in the *Opposite Hemisphere ISRA* case reads

$$\begin{cases} \hat{\bar{p}}_1^+ = \dfrac{p_{12\mathrm{T}}^2}{\hat{p}_1^- + \hat{p}_2^+} \\ \hat{\bar{p}}_1^- = \hat{p}_1^- + \hat{p}_2^+ \\ \vec{\bar{p}}_{1\mathrm{T}} = \vec{p}_{12\mathrm{T}} \end{cases} \qquad \begin{cases} \bar{x}_a = x_a - \dfrac{e^{y_{\mathrm{CS}}}}{\sqrt{S}} \left(\hat{p}_2^- - \hat{p}_2^+\right) \\ \bar{x}_b = x_b - \dfrac{e^{-y_{\mathrm{CS}}}}{\sqrt{S}} \left(\hat{p}_{12}^+ - \dfrac{p_{12\mathrm{T}}^2}{\hat{p}_1^- + \hat{p}_2^+}\right), \end{cases} \tag{A.2}$$

where we called $S = (P_a + P_b)^2$.

A.2 Inverse mapping

A.2.1 Same Hemisphere ISRA

The formulae for p_2 only depend on the expressions for $\mathcal{T}_1$, given in eq. (7.11), z, given in eq. (7.33), and ϕ, so they are the same derived for the default mapping and presented in eq. (7.34). Once we know them, we can invert the formulae of eq. (A.1) to write the expression of the inverse mapping for the *Same Hemisphere ISRA* case

$$\begin{cases} \hat{p}_1^+ = \hat{\bar{p}}_1^+ - \hat{p}_2^+ \\ \hat{p}_1^- = \dfrac{\left(\vec{\bar{p}}_{1\mathrm{T}} - \vec{p}_{2\mathrm{T}}\right)^2}{\hat{\bar{p}}_1^+ - \hat{p}_2^+} \\ \vec{p}_{1\mathrm{T}} = \vec{\bar{p}}_{1\mathrm{T}} - \vec{p}_{2\mathrm{T}} \end{cases} \qquad \begin{cases} x_a = \bar{x}_a + \dfrac{e^{y_{\mathrm{CS}}}}{\sqrt{S}} \left(\hat{p}_{12}^- - \dfrac{p_{12\mathrm{T}}^2}{\hat{p}_{12}^+}\right) \\ x_b = \bar{x}_b. \end{cases} \tag{A.3}$$

A.2.2 Opposite Hemisphere ISRA

Similarly to what we did above, we take the formulae for p_2 from eq. (7.34), and invert the formulae of eq. (A.2) to write the expression of the inverse mapping for the *Opposite Hemisphere ISRA* case

$$\begin{cases} \hat{p}_1^+ = \dfrac{\left(\vec{\bar{p}}_{1\mathrm{T}} - \vec{p}_{2\mathrm{T}}\right)^2}{\hat{\bar{p}}_1^- - \hat{p}_2^+} \\ \hat{p}_1^- = \hat{\bar{p}}_1^- - \hat{p}_2^+ \\ \vec{p}_{1\mathrm{T}} = \vec{\bar{p}}_{1\mathrm{T}} - \vec{p}_{2\mathrm{T}} \end{cases} \qquad \begin{cases} x_a = \bar{x}_a + \dfrac{e^{y_{\mathrm{CS}}}}{\sqrt{S}} \left(\hat{p}_2^- - \hat{p}_2^+\right) \\ x_b = \bar{x}_b + \dfrac{e^{-y_{\mathrm{CS}}}}{\sqrt{S}} \left(\hat{p}_{12}^+ - \dfrac{p_{12\mathrm{T}}^2}{\hat{p}_1^- + \hat{p}_2^+}\right). \end{cases} \tag{A.4}$$

A.2.3 FSRA

From the expression of $\mathcal{T}_1$ given in eq. (7.2), and by inverting the formulae of eq. (A.1) we find

$$\begin{cases} \hat{p}_{12}^{+} = \hat{\bar{p}}_1^{+} \\ \hat{p}_{12}^{-} = \dfrac{\hat{\bar{p}}_1^{-}\hat{\bar{p}}_1^{+} + \mathcal{T}_1\hat{\bar{p}}_1^{+} - \mathcal{T}_1^2}{\hat{\bar{p}}_1^{+} - \mathcal{T}_1} \\ \vec{p}_{12\mathrm{T}} = \vec{\bar{p}}_{1\mathrm{T}} \end{cases} \qquad \begin{cases} x_a = \bar{x}_a + \dfrac{e^{y_{\mathrm{CS}}}}{\sqrt{S}}\left(\hat{p}_{12}^{-} - \dfrac{p_{12\mathrm{T}}^2}{\hat{p}_{12}^{+}}\right) \\ x_b = \bar{x}_b. \end{cases} \tag{A.5}$$

A.3 Integration limits

A.3.1 FSRA

For the *FSRA* case we can recycle the entire calculation done in section 7.5.2 for the mapping that does not preserve q_{T}, granted that this time M^2 and $\hat{p}_{12}^{-}$ have a different expression in terms of $\bar{p}_1$ and $\mathcal{T}_1$. The constraints on z and ϕ are then the same as those given in eqs. (7.70), (7.76) and (7.77).

Additional constraint

When generating the phase space GENEVA puts the Φ_2 configurations that do not satisfy the condition

$$p_2^0 < \bar{p}_1^0 \tag{A.6}$$

among the non-projectable ones for technical reasons. This is allowed since such configurations are never divergent, but must be taken into account when computing the integration limits on z and ϕ. From the definition of z given in eq. (7.40) and the expression of $\bar{p}_1$ given in eq. (A.1) the condition of eq. (A.6) translates into the further constraint

$$z > \frac{p_{12}^{-}p_{12}^{+} - p_{12\mathrm{T}}^2}{p_{12}^{+}\left(p_{12}^{-} + p_{12}^{+}\right)}. \tag{A.7}$$

It can be seen from the expression of $\bar{p}_1$ in the mapping that does not preserve q_{T}, given in eq. (7.31), that the condition of eq. (A.6) does not impose any further constraint on z and ϕ.

A.3.2 ISRA

Constraints imposed by the mapping

We start from the expression for $d\Phi_2$ given in eq. (7.49), which, using the formulae presented in eq. (7.47) and (7.48) and imposing

$$\begin{aligned} \hat{p}_{1x} &= -\hat{p}_{2x} - q_x & \qquad m_{\mathrm{CS}}^2 &= q^2 \\ \hat{p}_{1y} &= -\hat{p}_{2y} - q_y & \qquad \hat{p}_{2\mathrm{T}}^2 &= \hat{p}_2^{-}\hat{p}_2^{+} \end{aligned} \tag{A.8}$$

to remove four integration variables, can be rewritten as

$$\begin{aligned} d\Phi_2 = dx_a\, dx_b\, \frac{dq^-\, dq^+\, dq_{\scriptscriptstyle\mathrm{T}}^2\, d\Phi_q}{4}\, \theta\big(q^-\big)\, \theta\big(q^+\big)\, \frac{d\hat{p}_1^-\, d\hat{p}_1^+}{2\,(2\pi)^3}\, \theta\big(\hat{p}_1^-\big)\, \theta\big(\hat{p}_1^+\big) \\ \times \delta\Big(\hat{p}_1^-\hat{p}_1^+ - \hat{p}_2^-\hat{p}_2^+ - q_{\scriptscriptstyle\mathrm{T}}^2 - 2\sqrt{\hat{p}_2^-\hat{p}_2^+ q_{\scriptscriptstyle\mathrm{T}}^2}\cos(\phi-\Phi_q)\Big) \\ \times \frac{d\hat{p}_2^-\, d\hat{p}_2^+\, d\phi}{4\,(2\pi)^3}\, \theta\big(\hat{p}_2^-\big)\, \theta\big(\hat{p}_2^+\big)\, \delta\left(\hat{p}_1^- + \hat{p}_2^- + \sqrt{q^-q^+} - \sqrt{S}x_a\sqrt{\frac{q^+}{q^-}}\right) \\ \times \delta\left(\hat{p}_1^+ + \hat{p}_2^+ + \sqrt{q^-q^+} - \sqrt{S}x_b\sqrt{\frac{q^-}{q^+}}\right) d\Phi_{\scriptscriptstyle\mathrm{CS}}\big(q^-q^+ - q_{\scriptscriptstyle\mathrm{T}}^2\big)\,. \end{aligned} \tag{A.9}$$

At this point we can use two of the three remaining δ functions to remove the integration over x_a and x_b and impose

$$x_a = \sqrt{\frac{q^-}{q^+}}\left(\frac{\hat{p}_1^- + \hat{p}_2^- + \sqrt{q^-q^+}}{\sqrt{S}}\right) \qquad x_b = \sqrt{\frac{q^+}{q^-}}\left(\frac{\hat{p}_1^+ + \hat{p}_2^+ + \sqrt{q^-q^+}}{\sqrt{S}}\right). \tag{A.10}$$

Since the integral over both x_a and x_b was limited to the interval $(0,1)$, we have to enforce that the above expressions are in such a range. We can immediately see that the positivity of q^-, q^+, $\hat{p}_1^-$, $\hat{p}_1^+$, $\hat{p}_2^-$ and $\hat{p}_2^+$ guarantees that the above expressions for x_a and x_b are always positive. We are then left with requiring that they are smaller than 1 by adding two more θ functions, which leads us to

$$\begin{aligned} d\Phi_2 = \frac{dq^-\, dq^+\, dq_{\scriptscriptstyle\mathrm{T}}^2\, d\Phi_q}{4S}\, \theta\big(q^-\big)\, \theta\big(q^+\big)\, \frac{d\hat{p}_1^-\, d\hat{p}_1^+}{2\,(2\pi)^3}\, \theta\big(\hat{p}_1^-\big)\, \theta\big(\hat{p}_1^+\big) \\ \times \delta\Big(\hat{p}_1^-\hat{p}_1^+ - \hat{p}_2^-\hat{p}_2^+ - q_{\scriptscriptstyle\mathrm{T}}^2 - 2\sqrt{\hat{p}_2^-\hat{p}_2^+ q_{\scriptscriptstyle\mathrm{T}}^2}\cos(\phi-\Phi_q)\Big) \\ \times \frac{d\hat{p}_2^-\, d\hat{p}_2^+\, d\phi}{4\,(2\pi)^3}\, \theta\big(\hat{p}_2^-\big)\, \theta\big(\hat{p}_2^+\big)\, \theta\left(\sqrt{S}\sqrt{\frac{q^+}{q^-}} - \hat{p}_1^- - \hat{p}_2^- - \sqrt{q^-q^+}\right) \\ \times \theta\left(\sqrt{S}\sqrt{\frac{q^-}{q^+}} - \hat{p}_1^+ - \hat{p}_2^+ - \sqrt{q^-q^+}\right) d\Phi_{\scriptscriptstyle\mathrm{CS}}\big(q^-q^+ - q_{\scriptscriptstyle\mathrm{T}}^2\big)\,. \end{aligned} \tag{A.11}$$

To compute the integration limits on z and ϕ, we need to have six independent integration variables that do not depend on z and ϕ (i.e. they are only functions of Φ_1 and $\mathcal{T}_1$). The variables q^-, q^+, $q_{\scriptscriptstyle\mathrm{T}}^2$, Φ_q and $\hat{p}_2^+$ satisfy such a requirement. We will choose the sixth variable to be $\hat{p}_1^+$ in the *Same Hemisphere ISRA* case and $\hat{p}_2^-$ in the *Opposite Hemisphere ISRA* case.

Same Hemisphere ISRA Starting from eq. (A.11), after imposing

$$\hat{p}_1^- = \frac{\hat{p}_2^-\hat{p}_2^+ + q_{\scriptscriptstyle\mathrm{T}}^2 + 2\sqrt{\hat{p}_2^-\hat{p}_2^+ q_{\scriptscriptstyle\mathrm{T}}^2}\cos(\phi-\Phi_q)}{\hat{p}_1^+} \tag{A.12}$$

we can use the last δ function to remove the $\hat{p}_1^-$ integration variable and arrive to the final expression

$$\begin{aligned} d\Phi_2 = & \frac{dq^-\, dq^+\, dq_{\scriptscriptstyle\mathrm{T}}^2\, d\Phi_q}{8\,(2\pi)^3\, S}\,\theta\big(q^-\big)\,\theta\big(q^+\big)\,\frac{d\hat{p}_1^+}{\hat{p}_1^+}\theta\big(\hat{p}_1^+\big)\,\frac{d\hat{p}_2^-\, d\hat{p}_2^+\, d\phi}{4\,(2\pi)^3}\,\theta\big(\hat{p}_2^-\big)\,\theta\big(\hat{p}_2^+\big) \\ & \times\theta\left(\sqrt{S}\sqrt{\frac{q^+}{q^-}}-\hat{p}_2^- - \sqrt{q^-q^+} - \frac{\hat{p}_2^-\,\hat{p}_2^+ + q_{\scriptscriptstyle\mathrm{T}}^2 + 2\sqrt{\hat{p}_2^-\,\hat{p}_2^+\,q_{\scriptscriptstyle\mathrm{T}}^2}\cos(\phi-\Phi_q)}{\hat{p}_1^+}\right) \\ & \times\theta\left(\sqrt{S}\sqrt{\frac{q^-}{q^+}}-\hat{p}_1^+ - \hat{p}_2^+ - \sqrt{q^-q^+}\right)\,d\Phi_{\scriptscriptstyle\mathrm{CS}}\big(q^-q^+ - q_{\scriptscriptstyle\mathrm{T}}^2\big)\,. \end{aligned} \tag{A.13}$$

The constraints on z and ϕ that we are looking for will then be given by the two θ functions that depend on $\hat{p}_2^-$ and ϕ. The first one just imposes that $\hat{p}_2^-$ is positive, which from eq. (7.33) translates into requiring that $z<1$. We are left with solving the inequality

$$\hat{p}_2^-\,\big(\hat{p}_1^+ + \hat{p}_2^+\big) + 2\sqrt{\hat{p}_2^-\,\hat{p}_2^+\,q_{\scriptscriptstyle\mathrm{T}}^2}\cos(\phi-\Phi_q) - \hat{p}_1^+\left(\sqrt{S}\sqrt{\frac{q^+}{q^-}}-\sqrt{q^-q^+}\right) + q_{\scriptscriptstyle\mathrm{T}}^2 < 0 \tag{A.14}$$

with respect to ϕ, which imposes the constraint

$$\cos(\phi-\Phi_q) < \frac{\hat{p}_1^+\left(\sqrt{S}\sqrt{\dfrac{q^+}{q^-}}-\sqrt{q^-q^+}\right) - q_{\scriptscriptstyle\mathrm{T}}^2 - \hat{p}_2^-\,\big(\hat{p}_1^+ + \hat{p}_2^+\big)}{2\sqrt{\hat{p}_2^-\,\hat{p}_2^+\,q_{\scriptscriptstyle\mathrm{T}}^2}}. \tag{A.15}$$

Opposite Hemisphere ISRA Starting from eq. (A.11), after imposing

$$\hat{p}_1^+ = \frac{\hat{p}_2^-\,\hat{p}_2^+ + q_{\scriptscriptstyle\mathrm{T}}^2 + 2\sqrt{\hat{p}_2^-\,\hat{p}_2^+\,q_{\scriptscriptstyle\mathrm{T}}^2}\cos(\phi-\Phi_q)}{\hat{p}_1^-}, \tag{A.16}$$

we can use the last δ function to remove the $\hat{p}_1^+$ integration variable and arrive to the final expression

$$\begin{aligned} d\Phi_2 = & \frac{dq^-\, dq^+\, dq_{\scriptscriptstyle\mathrm{T}}^2\, d\Phi_q}{8\,(2\pi)^3\, S}\,\theta\big(q^-\big)\,\theta\big(q^+\big)\,\frac{d\hat{p}_1^-}{\hat{p}_1^-}\theta\big(\hat{p}_1^-\big)\,\frac{d\hat{p}_2^-\, d\hat{p}_2^+\, d\phi}{4\,(2\pi)^3}\,\theta\big(\hat{p}_2^-\big)\,\theta\big(\hat{p}_2^+\big) \\ & \times\theta\left(\sqrt{S}\sqrt{\frac{q^-}{q^+}}-\hat{p}_2^+ - \sqrt{q^-q^+} - \frac{\hat{p}_2^-\,\hat{p}_2^+ + q_{\scriptscriptstyle\mathrm{T}}^2 + 2\sqrt{\hat{p}_2^-\,\hat{p}_2^+\,q_{\scriptscriptstyle\mathrm{T}}^2}\cos(\phi-\Phi_q)}{\hat{p}_1^-}\right) \\ & \times\theta\left(\sqrt{S}\sqrt{\frac{q^+}{q^-}}-\hat{p}_1^- - \hat{p}_2^- - \sqrt{q^-q^+}\right)\,d\Phi_{\scriptscriptstyle\mathrm{CS}}\big(q^-q^+ - q_{\scriptscriptstyle\mathrm{T}}^2\big)\,. \end{aligned} \tag{A.17}$$

This time there are three θ functions that depend on $\hat{p}_2^-$ and ϕ. As we have seen before, the first one just imposes that $z < 1$. The last one still does not depend on ϕ and imposes that

$$\hat{p}_2^- < \sqrt{S}\sqrt{\frac{q^+}{q^-}} - \sqrt{q^- q^+} - \hat{p}_1^- . \tag{A.18}$$

Finally the third condition reads

$$\hat{p}_2^- \hat{p}_2^+ + 2\sqrt{\hat{p}_2^- \hat{p}_2^+ q_{\text{T}}^2}\cos(\phi - \Phi_q) - \hat{p}_1^- \left(\sqrt{S}\sqrt{\frac{q^-}{q^+}} - \sqrt{q^- q^+} - \hat{p}_2^+\right) + q_{\text{T}}^2 < 0, \tag{A.19}$$

and imposes that

$$\cos(\phi - \Phi_q) < \frac{\hat{p}_1^- \left(\sqrt{S}\sqrt{\frac{q^-}{q^+}} - \sqrt{q^- q^+}\right) - q_{\text{T}}^2 - \hat{p}_2^+ \left(\hat{p}_1^- + \hat{p}_2^-\right)}{2\sqrt{\hat{p}_2^- \hat{p}_2^+ q_{\text{T}}^2}}. \tag{A.20}$$

Constraints imposed by the slicing of the phase space

Following what we did for the mapping that does not preserve q_{T}, we now need to impose that $\hat{p}_2^+$ is the smallest among all the possible expressions for the one-jettiness (see eq. (7.62)). Furthermore, this time $\hat{p}_1^-$ and $\hat{p}_1^+$ could depend on z and ϕ, meaning that we also need to enforce that the expression we are using for $\mathcal{T}_0$ is the smallest among those given in eq. (7.8). To do that, we have to distinguish between the *Same Hemisphere ISRA* and *Opposite Hemisphere ISRA* cases.

Same Hemisphere ISRA In this case the condition on the zero-jettiness reads

$$\hat{p}_1^+ < \hat{p}_1^- , \tag{A.21}$$

and, together with the constraints of eq. (7.62), imposes that

$$\hat{p}_2^- > \hat{p}_2^+ \tag{A.22}$$

and

$$\begin{cases} \cos(\phi - \Phi_q) > \dfrac{\left(\hat{p}_1^+\right)^2 - \hat{p}_2^- \hat{p}_2^+ - q_{\text{T}}^2}{2\sqrt{\hat{p}_2^- \hat{p}_2^+ q_{\text{T}}^2}} \\ \cos(\phi - \Phi_q) > \dfrac{\hat{p}_1^+ \hat{p}_2^+ - \hat{p}_2^- \left(\hat{p}_1^+ + \hat{p}_2^+\right)}{2\sqrt{\hat{p}_2^- \hat{p}_2^+ q_{\text{T}}^2}}. \end{cases} \tag{A.23}$$

Opposite Hemisphere ISRA In this case the condition on the zero-jettiness reads

$$\hat{p}_1^- < \hat{p}_1^+, \tag{A.24}$$

and, together with the constraints of eq. (7.62), imposes that

$$\hat{p}_2^- > \hat{p}_2^+ \tag{A.25}$$

and

$$\begin{cases} \cos(\phi - \Phi_q) > \dfrac{\left(\hat{p}_1^-\right)^2 - \hat{p}_2^- \hat{p}_2^+ - q_{\mathrm{T}}^2}{2\sqrt{\hat{p}_2^- \hat{p}_2^+ q_{\mathrm{T}}^2}} \\ \cos(\phi - \Phi_q) > -\dfrac{\left(\hat{p}_2^- \hat{p}_2^+ + q_{\mathrm{T}}^2\right)\left(\hat{p}_2^- - \hat{p}_2^+\right) + \hat{p}_2^- \hat{p}_2^+ \hat{p}_1^-}{2\sqrt{\hat{p}_2^- \hat{p}_2^+ q_{\mathrm{T}}^2}\left(\hat{p}_1^- + \hat{p}_2^- - \hat{p}_2^+\right)}. \end{cases} \tag{A.26}$$

A.4 Jacobian

ISRA

Starting from the expression of eq. (6.6) and following the same steps that took us from eq. (7.45) to eqs. (A.13) and (A.17), we can write the phase space with one final-state parton in the *Same Hemisphere ISRA* case as

$$\begin{aligned} d\Phi_1 = {} & \frac{d\bar{q}^-\, d\bar{q}^+\, d\bar{q}_{\mathrm{T}}^2\, d\bar{\Phi}_q}{8\,(2\pi)^3\, S}\, \theta\left(\bar{q}^-\right)\theta\left(\bar{q}^+\right)\frac{d\mathcal{T}_0}{\mathcal{T}_0}\,\theta(\mathcal{T}_0)\, d\Phi_{\mathrm{CS}}\left(\bar{q}^-\bar{q}^+ - \bar{q}_{\mathrm{T}}^2\right) \\ & \times \theta\left(\sqrt{S}\sqrt{\frac{\bar{q}^+}{\bar{q}^-}} - \frac{\bar{q}_{\mathrm{T}}^2}{\mathcal{T}_0} - \sqrt{\bar{q}^-\bar{q}^+}\right)\theta\left(\sqrt{S}\sqrt{\frac{\bar{q}^-}{\bar{q}^+}} - \mathcal{T}_0 - \sqrt{\bar{q}^-\bar{q}^+}\right) \end{aligned} \tag{A.27}$$

and in the *Opposite Hemisphere ISRA* case as

$$\begin{aligned} d\Phi_1 = {} & \frac{d\bar{q}^-\, d\bar{q}^+\, d\bar{q}_{\mathrm{T}}^2\, d\bar{\Phi}_q}{8\,(2\pi)^3\, S}\, \theta\left(\bar{q}^-\right)\theta\left(\bar{q}^+\right)\frac{d\mathcal{T}_0}{\mathcal{T}_0}\,\theta(\mathcal{T}_0)\, d\Phi_{\mathrm{CS}}\left(\bar{q}^-\bar{q}^+ - \bar{q}_{\mathrm{T}}^2\right) \\ & \times \theta\left(\sqrt{S}\sqrt{\frac{\bar{q}^+}{\bar{q}^-}} - \mathcal{T}_0 - \sqrt{\bar{q}^-\bar{q}^+}\right)\theta\left(\sqrt{S}\sqrt{\frac{\bar{q}^-}{\bar{q}^+}} - \frac{\bar{q}_{\mathrm{T}}^2}{\mathcal{T}_0} - \sqrt{\bar{q}^-\bar{q}^+}\right). \end{aligned} \tag{A.28}$$

At this point, starting from the result of eqs. (A.13) and (A.17), since

$$\frac{d\hat{p}_1^+}{\hat{p}_1^+} = \frac{d\mathcal{T}_0}{\mathcal{T}_0 - \mathcal{T}_1}. \tag{A.29}$$

and $d\hat{p}_2^+ = d\mathcal{T}_1$, using eq. (7.81), we finally arrive to

$$\frac{d\Phi_2}{d\Phi_1\, d\mathcal{T}_1\, dz\, d\phi} = \frac{\sqrt{S}\bar{x}_a e^{-y_{\mathrm{CS}}}}{4\,(2\pi)^3\, z^2}\,\frac{\mathcal{T}_0}{\mathcal{T}_0 - \mathcal{T}_1}. \tag{A.30}$$

FSRA

In this case we start from the expression of $d\Phi_1$ and $d\Phi_2$ given in eqs. (7.68) and (7.78). From eq. (A.5) we can write that $\hat{p}_{12}^+ = \hat{\bar{p}}_1^+$, $\Phi = \bar{\Phi}_1$, and

$$d\hat{p}_{12}^- \, dM^2 = \mathcal{T}_0 \left[1 + \frac{q_{\scriptscriptstyle \mathrm{T}}^2}{(\mathcal{T}_0 - \mathcal{T}_1)^2} \right] d\hat{\bar{p}}_1^- \, d\mathcal{T}_1. \tag{A.31}$$

At this point, from the above equation and eq. (7.85), we finally arrive to

$$\frac{d\Phi_2}{d\Phi_1 \, d\mathcal{T}_1 \, dz \, d\phi} = \frac{\mathcal{T}_0}{4\,(2\pi)^3\,\beta_0} \left[1 + \frac{q_{\scriptscriptstyle \mathrm{T}}^2}{(\mathcal{T}_0 - \mathcal{T}_1)^2} \right]. \tag{A.32}$$

We highlight that $\mathcal{T}_1$ is always strictly smaller than $\mathcal{T}_0$ so that the denominator in the above expression is never 0.

A.5 Comparison of the two $2 \to 1$ mappings

The default $2 \to 1$ mapping used in GENEVA (which was also used for producing all the NNLO distributions presented in this work) is the one that does not preserve the transverse momentum of the color singlet. Such a choice is dictated by the effect that the mapping has on some of the exclusive distributions. Indeed, while the distributions of the observables that only depend on Φ_N and $\mathcal{T}_N$ have, by construction, no dependence on the $N+1 \to N$ mapping, all the others have.

In particular, the $2 \to 1$ $q_{\scriptscriptstyle \mathrm{T}}$-preserving mapping introduces an unphysical distortion in the distribution of the rapidity difference $y_{j_1} - y_{\scriptscriptstyle \mathrm{CS}}$ between the color singlet and the hardest jet. Calling p_1 the momentum of the hardest parton, we can write such observable as

$$y_{j_1} - y_{\scriptscriptstyle \mathrm{CS}} = \frac{1}{2} \log \frac{\hat{p}_1^-}{\hat{p}_1^+}. \tag{A.33}$$

The condition presented in eq. 7.23 under which the $2 \to 1$ mapping that does not preserve $q_{\scriptscriptstyle \mathrm{T}}$ is built ensures that the Φ_2 configurations where the hardest parton has $\hat{p}_1^- < \hat{p}_1^+$ are projected on Φ_1 configurations where the parton still has $\hat{\bar{p}}_1^- < \hat{\bar{p}}_1^+$, thus preventing $y_{j_1} - y_{\scriptscriptstyle \mathrm{CS}}$ from changing sign, which would spoil the peak of the distribution.

Appendix B

Theoretical uncertainties in the MiNNLO$_{\rm PS}$ method

The theoretical uncertainties in the MiNNLO$_{\rm PS}$ method are estimated via a seven-point scale variation, where the factorization and renormalization scales $\mu_{\rm F}$ and $\mu_{\rm R}$ are multiplied respectively by the factors $K_{\rm F}$ and $K_{\rm R}$, whose values can be 1, 2 or 1/2. Out of the nine results, those with $K_{\rm F} = 1/2$ and $K_{\rm R} = 2$ or $K_{\rm F} = 2$ and $K_{\rm R} = 1/2$ are discarded, and the maximum and minimum values among the remaining seven provide the estimate of the theoretical uncertainties.

B.1 RG and DGLAP equations

The explicit dependence of the luminosity factor and Sudakov form factor from $K_{\rm F}$ and $K_{\rm R}$ can be derived by imposing that it cancels, order by order in the $\alpha_{\rm S}$ expansion, the dependence of the PDFs and the strong coupling from the same parameters. To do this, we first need to write the solution to the renormalization-group (RG) evolution equation for the strong coupling [70, 71]

$$\frac{\partial}{\partial\mu}\left(\frac{\alpha_{\rm S}(\mu)}{2\pi}\right) = -\frac{2}{\mu}\sum_n \bar{\beta}_n \left(\frac{\alpha_{\rm S}(\mu)}{2\pi}\right)^{n+2}, \tag{B.1}$$

where we have introduced (with the aim of simplifying the expression of the following equations) the coefficients $\bar{\beta}_n = \beta_n/2$ (the latter given in eq. (3.55)), and the DGLAP equation for the PDFs [48]

$$\frac{\partial f_k^{[h]}(x,\mu)}{\partial\mu} = \frac{2}{\mu}\sum_n\sum_j \left(P_{kj}^{(n)} \otimes f_j^{[h]}\right)(x,\mu)\left(\frac{\alpha_{\rm S}(\mu)}{2\pi}\right)^{n+1}, \tag{B.2}$$

where the splitting functions $P_{kj}^{(0)}$ were given in eq. (10.17). The solution to the RG equation is given by

$$\frac{\alpha_{\rm S}(\mu)}{2\pi} = \frac{\alpha_{\rm S}(p_{\rm T})}{2\pi} - \left(\frac{\alpha_{\rm S}(p_{\rm T})}{2\pi}\right)^2 \bar{\beta}_0 \log\left(\frac{\mu^2}{p_{\rm T}^2}\right) - \left(\frac{\alpha_{\rm S}(p_{\rm T})}{2\pi}\right)^3 \left[\bar{\beta}_1 \log\left(\frac{\mu^2}{p_{\rm T}^2}\right) - \bar{\beta}_0^2 \log^2\left(\frac{\mu^2}{p_{\rm T}^2}\right)\right] + \mathcal{O}\big(\alpha_{\rm S}^4\big)\,. \quad \text{(B.3)}$$

The solution to the DGLAP equation (which improves the result of eq. (10.20) instead reads

$$\begin{aligned} f_k^{[h]}(x,\mu) = f_k^{[h]}(x,p_{\rm T}) &+ \frac{\alpha_{\rm S}(p_{\rm T})}{2\pi} \sum_j \Big(P_{kj}^{(0)} \otimes f_j^{[h]}\Big)(x,p_{\rm T}) \log\left(\frac{\mu^2}{p_{\rm T}^2}\right) \\ &+ \left(\frac{\alpha_{\rm S}(p_{\rm T})}{2\pi}\right)^2 \left[\sum_j \Big(P_{kj}^{(1)} \otimes f_j^{[h]}\Big)(x,p_{\rm T}) \log\left(\frac{\mu^2}{p_{\rm T}^2}\right)\right. \\ &+ \sum_{jj'} \Big(P_{kj'}^{(0)} \otimes P_{j'j}^{(0)} \otimes f_j^{[h]}\Big)(x,p_{\rm T})\, \frac{1}{2} \log^2\left(\frac{\mu^2}{p_{\rm T}^2}\right) \\ &\left. - \bar{\beta}_0 \sum_j \Big(P_{kj}^{(0)} \otimes f_j^{[h]}\Big)(x,p_{\rm T})\, \frac{1}{2} \log^2\left(\frac{\mu^2}{p_{\rm T}^2}\right)\right] + \mathcal{O}\big(\alpha_{\rm S}^3\big)\,. \quad \text{(B.4)} \end{aligned}$$

B.2 Scale dependence of the resummed term

Using the results of eqs. (B.3) and (B.4) to expand the strong coupling and the PDFs around the scale $p_{\rm T}$, we can now derive the explicit dependence on $\mu_{\rm F}$ and $\mu_{\rm R}$ of all the terms appearing in the resummed contribution. The scale-dependent hard-virtual coefficient functions appearing in eq. (10.10) then reads

$$H_{k\bar{k}}^{(1)}(\mu_{\rm R}) = H_{k\bar{k}}^{(1)}(p_{\rm T}) + n_{\rm B}\, \bar{\beta}_0\, \log\left(\frac{\mu_{\rm R}^2}{p_{\rm T}^2}\right) H_{k\bar{k}}^{(0)} \quad \text{(B.5)}$$

$$\begin{aligned} H_{k\bar{k}}^{(2)}(\mu_{\rm R}) = H_{k\bar{k}}^{(2)}(p_{\rm T}) &+ (n_{\rm B}+1)\, \bar{\beta}_0\, \log\left(\frac{\mu_{\rm R}^2}{p_{\rm T}^2}\right) H_{k\bar{k}}^{(1)}(\mu_{\rm R}) \\ &+ \left[n_{\rm B}\, \bar{\beta}_1\, \log\left(\frac{\mu_{\rm R}^2}{p_{\rm T}^2}\right) - \frac{n_{\rm B}\,(n_{\rm B}+1)}{2}\, \bar{\beta}_0^2\, \log^2\left(\frac{\mu_{\rm R}^2}{p_{\rm T}^2}\right)\right] H_{k\bar{k}}^{(0)}\,. \end{aligned} \quad \text{(B.6)}$$

The quark collinear coefficient function reads

$$C_{kj}^{(1)}(z,\mu_{\rm F},\mu_{\rm R}) = C_{kj}^{(1)}(z) - P_{kj}^{(0)}(z)\log\left(\frac{\mu_{\rm F}^2}{p_{\rm T}^2}\right) \tag{B.7}$$

$$\begin{aligned}\tilde{C}_{kj}^{(2)}(z,\mu_{\rm F},\mu_{\rm R}) = \tilde{C}_{kj}^{(2)}(z) &- \sum_{j'}\left(C_{kj'}^{(1)}\otimes P_{j'j}^{(0)}\right)(z)\log\left(\frac{\mu_{\rm F}^2}{p_{\rm T}^2}\right)\\ &- P_{kj}^{(1)}(z)\log\left(\frac{\mu_{\rm F}^2}{p_{\rm T}^2}\right) + \sum_{j'}\left(P_{kj'}^{(0)}\otimes P_{j'j}^{(0)}\right)(z)\,\frac{1}{2}\log^2\left(\frac{\mu_{\rm F}^2}{p_{\rm T}^2}\right)\\ &+ \bar{\beta}_0 P_{kj}^{(0)}(z)\,\frac{1}{2}\log^2\left(\frac{\mu_{\rm F}^2}{p_{\rm T}^2}\right) + \bar{\beta}_0 C_{kj}^{(1)}(z,\mu_{\rm F},\mu_{\rm R})\log\left(\frac{\mu_{\rm R}^2}{p_{\rm T}^2}\right)\end{aligned} \tag{B.8}$$

and the coefficients of the Sudakov form factor

$$A_{k\bar{k}}^{(2)}(K_{\rm R}) = A_{k\bar{k}}^{(2)} + A_{k\bar{k}}^{(1)}\bar{\beta}_0\log\left(K_{\rm R}^2\right) \qquad B_{k\bar{k}}^{(2)}(K_{\rm R}) = B_{k\bar{k}}^{(2)} + B_{k\bar{k}}^{(1)}\bar{\beta}_0\log\left(K_{\rm R}^2\right). \tag{B.9}$$

Finally, the scale dependence of the gluon collinear coefficient function is trivial, since it appears at LO only.

B.3 Scale dependence of the non-singular term

After using the above equations to compute the scale variations of the resummed contribution, we are left with the doing the same for the non-singular term. The derivatives of the Sudakov form factor and the luminosity factor up to second order in the $\alpha_{\rm S}$ expansion reads

$$\left[\frac{d\tilde{S}_{k\bar{k}}}{dp_{\rm T}}\right]^{(1)}(p_{\rm T},\mu_{\rm R}) = -\frac{2}{p_{\rm T}}\left\{A_{k\bar{k}}^{(1)}\log\left(\frac{Q^2}{p_{\rm T}^2}\right) + B_{k\bar{k}}^{(1)}\right\} \tag{B.10}$$

$$\left[\frac{d\tilde{S}_{k\bar{k}}}{dp_{\rm T}}\right]^{(2)}(p_{\rm T},\mu_{\rm R}) = -\frac{2}{p_{\rm T}}\left\{A_{k\bar{k}}^{(2)}\log\left(\frac{Q^2}{p_{\rm T}^2}\right) + \tilde{B}_{k\bar{k}}^{(2)} + \bar{\beta}_0\left[\frac{d\tilde{S}_{k\bar{k}}}{dp_{\rm T}}\right]^{(1)}(p_{\rm T},\mu_{\rm R})\log\left(\frac{\mu_{\rm R}^2}{p_{\rm T}^2}\right)\right\} \tag{B.11}$$

and

$$\left[\frac{d\mathcal{L}_{k\bar{k}}}{dp_{\mathrm{T}}}\right]^{(1)}(p_{\mathrm{T}},\mu_{\mathrm{F}},\mu_{\mathrm{R}}) = \frac{2}{p_{\mathrm{T}}}\,H^{(0)}_{k\bar{k}}\sum_j\Big(P^{(0)}_{kj}\otimes f^{[a]}_j\Big)(x_a,\mu_{\mathrm{F}})\,f^{[b]}_{\bar{k}}(x_b,\mu_{\mathrm{F}}) + (a\leftrightarrow b) \tag{B.12}$$

$$\begin{aligned}\left[\frac{d\mathcal{L}_{k\bar{k}}}{dp_{\mathrm{T}}}\right]^{(2)}(p_{\mathrm{T}},\mu_{\mathrm{F}},\mu_{\mathrm{R}}) = \frac{2}{p_{\mathrm{T}}}\Bigg\{ & H^{(0)}_{k\bar{k}}\sum_j\Big(P^{(1)}_{kj}\otimes f^{[a]}_j\Big)(x_a,\mu_{\mathrm{F}})\,f^{[b]}_{\bar{k}}(x_b,\mu_{\mathrm{F}}) \\ & + H^{(0)}_{k\bar{k}}\sum_{jj'}\Big[\Big(C^{(1)}_{kj'}\otimes P^{(0)}_{j'j}\otimes f^{[a]}_j\Big)(x_a,\mu_{\mathrm{F}})\,f^{[b]}_{\bar{k}}(x_b,\mu_{\mathrm{F}}) \\ & + \Big(P^{(0)}_{kj}\otimes f^{[a]}_j\Big)(x_a,\mu_{\mathrm{F}})\Big(C^{(1)}_{kj'}\otimes f^{[b]}_{j'}\Big)(x_b,\mu_{\mathrm{F}})\Big] \\ & - H^{(0)}_{k\bar{k}}\sum_{jj'}\Big[\Big(P^{(0)}_{kj'}\otimes P^{(0)}_{j'j}\otimes f^{[a]}_j\Big)(x_a,\mu_{\mathrm{F}})\,f^{[b]}_{\bar{k}}(x_b,\mu_{\mathrm{F}}) \\ & + \Big(P^{(0)}_{kj}\otimes f^{[a]}_j\Big)(x_a,\mu_{\mathrm{F}})\Big(P^{(0)}_{\bar{k}j}\otimes f^{[b]}_j\Big)(x_b,\mu_{\mathrm{F}})\Big]\log\left(\frac{\mu^2_{\mathrm{F}}}{p^2_{\mathrm{T}}}\right) \\ & + H^{(1)}_{k\bar{k}}(\mu_{\mathrm{R}})\sum_j\Big(P^{(0)}_{kj}\otimes f^{[a]}_j\Big)(x_a,\mu_{\mathrm{F}})\,f^{[b]}_{\bar{k}}(x_b,\mu_{\mathrm{F}}) \\ & + (a\leftrightarrow b) - \bar{\beta}_0\mathcal{L}^{(1)}_{k\bar{k}}(p_{\mathrm{T}},\mu_{\mathrm{F}},\mu_{\mathrm{R}}) \\ & + \bar{\beta}_0\left[\frac{d\mathcal{L}_{k\bar{k}}}{dp_{\mathrm{T}}}\right]^{(1)}(p_{\mathrm{T}},\mu_{\mathrm{F}},\mu_{\mathrm{R}})\log\left(\frac{\mu^2_{\mathrm{R}}}{p^2_{\mathrm{T}}}\right)\Bigg\},\end{aligned} \tag{B.13}$$

In the non-singular contribution R_f of the original MiNNLOPS approach presented in eq. (10.32), the presence of the Sudakov form factor and the use of factorization and renormalization scales $\mu_{\mathrm{F}} = \mu_{\mathrm{R}} = p_{\mathrm{T}}$ introduce $\mathcal{O}\big(\alpha_{\mathrm{S}}^3\big)$ deviations with respect to a fixed-order calculation that, despite being beyond the claimed accuracy, could have sizable numerical effects. However, there is typically a numerical cancellation between the two effects, due to the fact that the Sudakov form factor tends to reduce the total cross section and the scale p_{T} (instead of Q) has typically the opposite effect. If we call

$$\frac{d\sigma^{\mathrm{NS,LO}}_{k\bar{k}}}{d\Phi_1}(\mu) = \frac{d\sigma^{k\bar{k},\mathrm{LO}}_{\mathrm{CS+jet}}}{d\Phi_1}(\mu) - \frac{\alpha_{\mathrm{S}}(\mu)}{2\pi}\,D^{(1)}_{k\bar{k}}(p_{\mathrm{T}},\mu) \tag{B.14}$$

$$\begin{aligned}\frac{d\sigma^{\mathrm{NS,NLO}}_{k\bar{k}}}{d\Phi_1}(\mu) = \frac{d\sigma^{k\bar{k},\mathrm{PWG}}_{\mathrm{CS+jet}}}{d\Phi_1}(\mu) - \Bigg\{ & \frac{\alpha_{\mathrm{S}}(\mu)}{2\pi}\,D^{(1)}_{k\bar{k}}(p_{\mathrm{T}},\mu) \\ & + \left(\frac{\alpha_{\mathrm{S}}(\mu)}{2\pi}\right)^2\Big[D^{(2)}_{k\bar{k}}(p_{\mathrm{T}},\mu) - \tilde{S}^{(1)}_{k\bar{k}}(p_{\mathrm{T}})\Big]\Bigg\}F^{\mathrm{corr}}(\Phi_1)\,,\end{aligned} \tag{B.15}$$

the original R_f can be written as

$$R_f = e^{-\tilde{S}_{k\bar{k}}(p_{\rm T})} \left[\frac{d\sigma^{\rm NS,NLO}_{k\bar{k}}}{d\Phi_1}(p_{\rm T}) + \frac{\alpha_{\rm S}(p_{\rm T})}{2\pi}\, \tilde{S}^{(1)}_{k\bar{k}}(p_{\rm T})\, \frac{d\sigma^{\rm NS,LO}_{k\bar{k}}}{d\Phi_1}(p_{\rm T}) \right], \tag{B.16}$$

and we can write

$$\begin{aligned} e^{-\tilde{S}_{k\bar{k}}(p_{\rm T})} &= 1 - \frac{\alpha_{\rm S}(p_{\rm T})}{2\pi}\, \tilde{S}^{(1)}_{k\bar{k}}\,(p_{\rm T}) - C_1 \left(\frac{\alpha_{\rm S}}{2\pi}\right)^2 + \mathcal{O}\big(\alpha_{\rm S}^3\big) \\ \frac{d\sigma^{\rm NS,NLO}_{k\bar{k}}}{d\Phi_1}(p_{\rm T}) &= \frac{d\sigma^{\rm NS,NLO}_{k\bar{k}}}{d\Phi_1}(Q) + C_2 \left(\frac{\alpha_{\rm S}}{2\pi}\right)^3 + \mathcal{O}\big(\alpha_{\rm S}^4\big)\,, \end{aligned} \tag{B.17}$$

where C_1 and C_2 are two functions that we typically expect to be positive, so that the product reads

$$e^{-\tilde{S}_{k\bar{k}}(p_{\rm T})}\, \frac{d\sigma^{\rm NS,NLO}_{k\bar{k}}}{d\Phi_1}(p_{\rm T}) = \frac{d\sigma^{\rm NS,NLO}_{k\bar{k}}}{d\Phi_1}(Q) + \left(C_2 - \tilde{C}_1\right) \left(\frac{\alpha_{\rm S}}{2\pi}\right)^3 + \mathcal{O}\big(\alpha_{\rm S}^4\big)\,, \tag{B.18}$$

and we have called $\tilde{C}_1$ the product between C_1 and the Sudakov form factor. However, this is not anymore the case once scale variations are taken into account. Indeed, both the scale variations are of order $\mathcal{O}\big(\alpha_{\rm S}^3\big)$

$$\begin{aligned} e^{-\tilde{S}_{k\bar{k}}(p_{\rm T},K)} &= e^{-\tilde{S}_{k\bar{k}}(p_{\rm T})} - D_1 \left(\frac{\alpha_{\rm S}}{2\pi}\right)^3 + \mathcal{O}\big(\alpha_{\rm S}^4\big) \\ \frac{d\sigma^{\rm NS,NLO}_{k\bar{k}}}{d\Phi_1}(Kp_{\rm T}) &= \frac{d\sigma^{\rm NS,NLO}_{k\bar{k}}}{d\Phi_1}(p_{\rm T}) + D_2 \left(\frac{\alpha_{\rm S}}{2\pi}\right)^3 + \mathcal{O}\big(\alpha_{\rm S}^4\big)\,, \end{aligned} \tag{B.19}$$

where D_1 and D_2 are two other functions. However, after the multiplication we find

$$e^{-\tilde{S}_{k\bar{k}}(p_{\rm T},K)}\, \frac{d\sigma^{\rm NS,NLO}_{k\bar{k}}}{d\Phi_1}(Kp_{\rm T}) = e^{-\tilde{S}_{k\bar{k}}(p_{\rm T})}\, \frac{d\sigma^{\rm NS,NLO}_{k\bar{k}}}{d\Phi_1}(p_{\rm T}) + D_2 \left(\frac{\alpha_{\rm S}}{2\pi}\right)^3 + \mathcal{O}\big(\alpha_{\rm S}^4\big)\,, \tag{B.20}$$

which means that the scale variation is dominated by one contribution alone, and the numerical cancellation that we observed before is not there anymore.

Bibliography

[1] Simone Alioli et al. "Next-to-next-to-leading order event generation for Z boson pair production matched to parton shower". In: *Phys. Lett. B* 818 (2021), p. 136380. DOI: 10.1016/j.physletb.2021.136380. arXiv: 2103.01214 [hep-ph].

[2] Alessandro Gavardi, Carlo Oleari, and Emanuele Re. "NNLO+PS Monte Carlo simulation of photon pair production with MiNNLO$_{PS}$". In: *JHEP* 09 (2022), p. 061. DOI: 10.1007/JHEP09(2022)061. arXiv: 2204.12602 [hep-ph].

[3] Christian Bierlich et al. "A comprehensive guide to the physics and usage of PYTHIA 8.3". In: (Mar. 2022). arXiv: 2203.11601 [hep-ph].

[4] Johannes Bellm et al. "Herwig 7.0/Herwig++ 3.0 release note". In: *Eur. Phys. J. C* 76.4 (2016), p. 196. DOI: 10.1140/epjc/s10052-016-4018-8. arXiv: 1512.01178 [hep-ph].

[5] Johannes Bellm et al. "Herwig 7.2 release note". In: *Eur. Phys. J. C* 80.5 (2020), p. 452. DOI: 10.1140/epjc/s10052-020-8011-x. arXiv: 1912.06509 [hep-ph].

[6] Enrico Bothmann et al. "Event Generation with Sherpa 2.2". In: *SciPost Phys.* 7.3 (2019), p. 034. DOI: 10.21468/SciPostPhys.7.3.034. arXiv: 1905.09127 [hep-ph].

[7] Stefano Frixione and Bryan R. Webber. "Matching NLO QCD computations and parton shower simulations". In: *JHEP* 06 (2002), p. 029. DOI: 10.1088/1126-6708/2002/06/029. arXiv: hep-ph/0204244.

[8] Paolo Nason. "A New method for combining NLO QCD with shower Monte Carlo algorithms". In: *JHEP* 11 (2004), p. 040. DOI: 10.1088/1126-6708/2004/11/040. arXiv: hep-ph/0409146.

[9] Stefano Frixione, Paolo Nason, and Carlo Oleari. "Matching NLO QCD computations with Parton Shower simulations: the POWHEG method". In: *JHEP* 11 (2007), p. 070. DOI: 10.1088/1126-6708/2007/11/070. arXiv: 0709.2092 [hep-ph].

[10] Simone Alioli et al. "A general framework for implementing NLO calculations in shower Monte Carlo programs: the POWHEG BOX". In: *JHEP* 06 (2010), p. 043. DOI: 10.1007/JHEP06(2010)043. arXiv: 1002.2581 [hep-ph].

[11] Keith Hamilton, Paolo Nason, and Giulia Zanderighi. "MINLO: Multi-Scale Improved NLO". In: *JHEP* 10 (2012), p. 155. DOI: 10.1007/JHEP10(2012)155. arXiv: 1206.3572 [hep-ph].

[12] Keith Hamilton et al. "Merging H/W/Z + 0 and 1 jet at NLO with no merging scale: a path to parton shower + NNLO matching". In: *JHEP* 05 (2013), p. 082. DOI: 10.1007/JHEP05(2013)082. arXiv: 1212.4504 [hep-ph].

[13] Stefan Hoeche et al. "QCD matrix elements + parton showers: The NLO case". In: *JHEP* 04 (2013), p. 027. DOI: 10.1007/JHEP04(2013)027. arXiv: 1207.5030 [hep-ph].

[14] R. Frederix and S. Frixione. "Merging meets matching in MC@NLO". In: *JHEP* 12 (2012), p. 061. DOI: 10.1007/JHEP12(2012)061. arXiv: 1209.6215 [hep-ph].

[15] Leif Lönnblad and Stefan Prestel. "Merging Multi-leg NLO Matrix Elements with Parton Showers". In: *JHEP* 03 (2013), p. 166. DOI: 10.1007/JHEP03(2013)166. arXiv: 1211.7278 [hep-ph].

[16] Pier Francesco Monni et al. "MiNNLO$_{PS}$: a new method to match NNLO QCD to parton showers". In: *JHEP* 05 (2020), p. 143. DOI: 10.1007/JHEP05(2020)143. arXiv: 1908.06987 [hep-ph].

[17] P. Francesco Monni, Emanuele Re, and Marius Wiesemann. "MiNNLO$_{\mathrm{PS}}$: optimizing $2 \to 1$ hadronic processes". In: *Eur. Phys. J. C* 80.11 (2020), p. 1075. DOI: 10.1140/epjc/s10052-020-08658-5. arXiv: 2006.04133 [hep-ph].

[18] Simone Alioli et al. "Drell-Yan production at NNLL'+NNLO matched to parton showers". In: *Phys. Rev. D* 92.9 (2015), p. 094020. DOI: 10.1103/PhysRevD.92.094020. arXiv: 1508.01475 [hep-ph].

[19] Simone Alioli et al. "Matching NNLO predictions to parton showers using N3LL color-singlet transverse momentum resummation in geneva". In: *Phys. Rev. D* 104.9 (2021), p. 094020. DOI: 10.1103/PhysRevD.104.094020. arXiv: 2102.08390 [hep-ph].

[20] Simone Alioli et al. "Higgsstrahlung at NNLL'+NNLO matched to parton showers in GENEVA". In: *Phys. Rev. D* 100.9 (2019), p. 096016. DOI: 10.1103/PhysRevD.100.096016. arXiv: 1909.02026 [hep-ph].

[21] S. Alioli et al. "Precise predictions for photon pair production matched to parton showers in GENEVA". In: *JHEP* 04 (2021), p. 041. DOI: 10.1007/JHEP04(2021)041. arXiv: 2010.10498 [hep-ph].

[22] Daniele Lombardi, Marius Wiesemann, and Giulia Zanderighi. "Advancing MiNNLO$_{PS}$ to diboson processes: Zγ production at NNLO+PS". In: *JHEP* 06 (2021), p. 095. DOI: 10.1007/JHEP06(2021)095. arXiv: 2010.10478 [hep-ph].

[23] Thomas Cridge, Matthew A. Lim, and Riccardo Nagar. "Wγ production at NNLO+PS accuracy in Geneva". In: *Phys. Lett. B* 826 (2022), p. 136918. DOI: 10.1016/j.physletb.2022.136918. arXiv: 2105.13214 [hep-ph].

[24] Daniele Lombardi, Marius Wiesemann, and Giulia Zanderighi. "W$^+$W$^-$ production at NNLO+PS with MINNLO$_{PS}$". In: *JHEP* 11 (2021), p. 230. DOI: 10.1007/JHEP11(2021)230. arXiv: 2103.12077 [hep-ph].

[25] Luca Buonocore et al. "ZZ production at nNNLO+PS with MiNNLO$_{PS}$". In: *JHEP* 01 (2022), p. 072. DOI: 10.1007/JHEP01(2022)072. arXiv: 2108.05337 [hep-ph].

[26] Jonas M. Lindert et al. "$W^{\pm}Z$ production at NNLO QCD and NLO EW matched to parton showers with MiNNLO$_{\mathrm{PS}}$". In: (Aug. 2022). arXiv: 2208.12660 [hep-ph].

[27] J. Mazzitelli et al. "Top-pair production at the LHC with MINNLO$_{PS}$". In: *JHEP* 04 (2022), p. 079. DOI: 10.1007/JHEP04(2022)079. arXiv: 2112.12135 [hep-ph].

[28] T. Kinoshita. "Mass singularities of Feynman amplitudes". In: *J. Math. Phys.* 3 (1962), pp. 650–677. DOI: 10.1063/1.1724268.

[29] T. D. Lee and M. Nauenberg. "Degenerate Systems and Mass Singularities". In: *Phys. Rev.* 133 (1964). Ed. by G. Feinberg, B1549–B1562. DOI: 10.1103/PhysRev.133.B1549.

[30] Iain W. Stewart, Frank J. Tackmann, and Wouter J. Waalewijn. "The Quark Beam Function at NNLL". In: *JHEP* 09 (2010), p. 005. DOI: 10.1007/JHEP09(2010)005. arXiv: 1002.2213 [hep-ph].

[31] Carola F. Berger et al. "Higgs Production with a Central Jet Veto at NNLL+NNLO". In: *JHEP* 04 (2011), p. 092. DOI: 10.1007/JHEP04(2011)092. arXiv: 1012.4480 [hep-ph].

[32] Iain W. Stewart, Frank J. Tackmann, and Wouter J. Waalewijn. "Factorization at the LHC: From PDFs to Initial State Jets". In: *Phys. Rev. D* 81 (2010), p. 094035. DOI: 10.1103/PhysRevD.81.094035. arXiv: 0910.0467 [hep-ph].

[33] Federico Buccioni et al. "OpenLoops 2". In: *Eur. Phys. J. C* 79.10 (2019), p. 866. DOI: 10.1140/epjc/s10052-019-7306-2. arXiv: 1907.13071 [hep-ph].

[34] Andy Buckley et al. "LHAPDF6: parton density access in the LHC precision era". In: *Eur. Phys. J. C* 75 (2015), p. 132. DOI: 10.1140/epjc/s10052-015-3318-8. arXiv: 1412.7420 [hep-ph].

[35] Ansgar Denner et al. "Electroweak corrections to charged-current e+ e- —> 4 fermion processes: Technical details and further results". In: *Nucl. Phys. B* 724 (2005). [Erratum: Nucl.Phys.B 854, 504–507 (2012)], pp. 247–294. DOI: 10.1016/j.nuclphysb.2011.09.001. arXiv: hep-ph/0505042.

[36] Eite Tiesinga et al. "CODATA recommended values of the fundamental physical constants: 2018*". In: *Rev. Mod. Phys.* 93.2 (2021), p. 025010. DOI: 10.1103/RevModPhys.93.025010.

[37] P. A. Zyla et al. "Review of Particle Physics". In: *PTEP* 2020.8 (2020), p. 083C01. DOI: 10.1093/ptep/ptaa104.

[38] D. Yu. Bardin et al. "Energy Dependent Width Effects in e+ e- Annihilation Near the Z Boson Pole". In: *Phys. Lett. B* 206 (1988), pp. 539–542. DOI: 10.1016/0370-2693(88)91627-9.

[39] "Combination of CDF and D0 Results on the Mass of the Top Quark". In: (Mar. 2009). arXiv: 0903.2503 [hep-ex].

[40] S. Dittmaier et al. "Handbook of LHC Higgs Cross Sections: 2. Differential Distributions". In: (Jan. 2012). DOI: 10.5170/CERN-2012-002. arXiv: 1201.3084 [hep-ph].

[41] Massimiliano Grazzini, Stefan Kallweit, and Marius Wiesemann. "Fully differential NNLO computations with MATRIX". In: *Eur. Phys. J. C* 78.7 (2018), p. 537. DOI: 10.1140/epjc/s10052-018-5771-7. arXiv: 1711.06631 [hep-ph].

[42] Fabio Cascioli, Philipp Maierhofer, and Stefano Pozzorini. "Scattering Amplitudes with Open Loops". In: *Phys. Rev. Lett.* 108 (2012), p. 111601. DOI: 10.1103/PhysRevLett.108.111601. arXiv: 1111.5206 [hep-ph].

[43] Federico Buccioni, Stefano Pozzorini, and Max Zoller. "On-the-fly reduction of open loops". In: *Eur. Phys. J. C* 78.1 (2018), p. 70. DOI: 10.1140/epjc/s10052-018-5562-1. arXiv: 1710.11452 [hep-ph].

[44] Thomas Gehrmann, Andreas von Manteuffel, and Lorenzo Tancredi. "The two-loop helicity amplitudes for $q\bar{q}' \to V_1V_2 \to 4$ leptons". In: *JHEP* 09 (2015), p. 128. DOI: 10.1007/JHEP09(2015)128. arXiv: 1503.04812 [hep-ph].

[45] Morad Aaboud et al. "$ZZ \to \ell^+\ell^-\ell'^+\ell'^-$ cross-section measurements and search for anomalous triple gauge couplings in 13 TeV pp collisions with the ATLAS detector". In: *Phys. Rev. D* 97.3 (2018), p. 032005. DOI: 10.1103/PhysRevD.97.032005. arXiv: 1709.07703 [hep-ex].

[46] Albert M Sirunyan et al. "Measurements of pp $\to$ ZZ production cross sections and constraints on anomalous triple gauge couplings at $\sqrt{s} = 13\,\text{TeV}$". In: *Eur. Phys. J. C* 81.3 (2021), p. 200. DOI: 10.1140/epjc/s10052-020-08817-8. arXiv: 2009.01186 [hep-ex].

[47] Keith Hamilton et al. "NNLOPS simulation of Higgs boson production". In: *JHEP* 10 (2013), p. 222. DOI: 10.1007/JHEP10(2013)222. arXiv: 1309.0017 [hep-ph].

[48] Guido Altarelli and G. Parisi. "Asymptotic Freedom in Parton Language". In: *Nucl. Phys. B* 126 (1977), pp. 298–318. DOI: 10.1016/0550-3213(77)90384-4.

[49] Luca D'Errico and Peter Richardson. "Next-to-Leading-Order Monte Carlo Simulation of Diphoton Production in Hadronic Collisions". In: *JHEP* 02 (2012), p. 130. DOI: 10.1007/JHEP02(2012)130. arXiv: 1106.3939 [hep-ph].

[50] Stefano Frixione. "Isolated photons in perturbative QCD". In: *Phys. Lett. B* 429 (1998), pp. 369–374. DOI: 10.1016/S0370-2693(98)00454-7. arXiv: hep-ph/9801442.

[51] A. van Hameren. "OneLOop: For the evaluation of one-loop scalar functions". In: *Comput. Phys. Commun.* 182 (2011), pp. 2427–2438. DOI: 10.1016/j.cpc.2011.06.011. arXiv: 1007.4716 [hep-ph].

[52] A. van Hameren, C. G. Papadopoulos, and R. Pittau. "Automated one-loop calculations: A Proof of concept". In: *JHEP* 09 (2009), p. 106. DOI: 10.1088/1126-6708/2009/09/106. arXiv: 0903.4665 [hep-ph].

[53] C. Anastasiou, E. W. Nigel Glover, and M. E. Tejeda-Yeomans. "Two loop QED and QCD corrections to massless fermion boson scattering". In: *Nucl. Phys. B* 629 (2002), pp. 255–289. DOI: 10.1016/S0550-3213(02)00140-2. arXiv: hep-ph/0201274.

[54] Stefano Catani et al. "Universality of transverse-momentum resummation and hard factors at the NNLO". In: *Nucl. Phys. B* 881 (2014), pp. 414–443. DOI: 10.1016/j.nuclphysb.2014.02.011. arXiv: 1311.1654 [hep-ph].

[55] Zvi Bern, Lance J. Dixon, and Carl Schmidt. "Isolating a light Higgs boson from the diphoton background at the CERN LHC". In: *Phys. Rev. D* 66 (2002), p. 074018. DOI: 10.1103/PhysRevD.66.074018. arXiv: hep-ph/0206194.

[56] John M. Campbell et al. "Predictions for diphoton production at the LHC through NNLO in QCD". In: *JHEP* 07 (2016), p. 148. DOI: 10.1007/JHEP07(2016)148. arXiv: 1603.02663 [hep-ph].

[57] Stefano Catani et al. "Diphoton production at hadron colliders: a fully-differential QCD calculation at NNLO". In: *Phys. Rev. Lett.* 108 (2012). [Erratum: Phys.Rev.Lett. 117, 089901 (2016)], p. 072001. DOI: 10.1103/PhysRevLett.108.072001. arXiv: 1110.2375 [hep-ph].

[58] Ansgar Denner, Stefan Dittmaier, and Lars Hofer. "Collier: a fortran-based Complex One-Loop LIbrary in Extended Regularizations". In: *Comput. Phys. Commun.* 212 (2017), pp. 220–238. DOI: 10.1016/j.cpc.2016.10.013. arXiv: 1604.06792 [hep-ph].

[59] Stefano Catani et al. "Vector boson production at hadron colliders: hard-collinear coefficients at the NNLO". In: *Eur. Phys. J. C* 72 (2012), p. 2195. DOI: 10.1140/epjc/s10052-012-2195-7. arXiv: 1209.0158 [hep-ph].

[60] Stefano Catani and Massimiliano Grazzini. "An NNLO subtraction formalism in hadron collisions and its application to Higgs boson production at the LHC". In: *Phys. Rev. Lett.* 98 (2007), p. 222002. DOI: 10.1103/PhysRevLett.98.222002. arXiv: hep-ph/0703012.

[61] Torbjorn Sjostrand, Stephen Mrenna, and Peter Z. Skands. "PYTHIA 6.4 Physics and Manual". In: *JHEP* 05 (2006), p. 026. DOI: 10.1088/1126-6708/2006/05/026. arXiv: hep-ph/0603175.

[62] Torbjörn Sjöstrand et al. "An introduction to PYTHIA 8.2". In: *Comput. Phys. Commun.* 191 (2015), pp. 159–177. DOI: 10.1016/j.cpc.2015.01.024. arXiv: 1410.3012 [hep-ph].

[63] Peter Skands, Stefano Carrazza, and Juan Rojo. "Tuning PYTHIA 8.1: the Monash 2013 Tune". In: *Eur. Phys. J. C* 74.8 (2014), p. 3024. DOI: 10.1140/epjc/s10052-014-3024-y. arXiv: 1404.5630 [hep-ph].

[64] Paolo Nason and Carlo Oleari. "Generation cuts and Born suppression in POWHEG". In: (Mar. 2013). arXiv: 1303.3922 [hep-ph].

[65] Adam Kardos and Zoltán Trócsányi. "Hadroproduction of t anti-t pair in association with an isolated photon at NLO accuracy matched with parton shower". In: *JHEP* 05 (2015), p. 090. DOI: 10.1007/JHEP05(2015)090. arXiv: 1406.2324 [hep-ph].

[66] Georges Aad et al. "Measurement of the production cross section of pairs of isolated photons in *pp* collisions at 13 TeV with the ATLAS detector". In: *JHEP* 11 (2021), p. 169. DOI: 10.1007/JHEP11(2021)169. arXiv: 2107.09330 [hep-ex].

[67] Andy Buckley et al. "Rivet user manual". In: *Comput. Phys. Commun.* 184 (2013), pp. 2803–2819. DOI: 10.1016/j.cpc.2013.05.021. arXiv: 1003.0694 [hep-ph].

[68] Stefano Catani et al. "Diphoton production at the LHC: a QCD study up to NNLO". In: *JHEP* 04 (2018), p. 142. DOI: 10.1007/JHEP04(2018)142. arXiv: 1802.02095 [hep-ph].

[69] A. Banfi et al. "Optimisation of variables for studying dilepton transverse momentum distributions at hadron colliders". In: *Eur. Phys. J. C* 71 (2011), p. 1600. DOI: 10.1140/epjc/s10052-011-1600-y. arXiv: 1009.1580 [hep-ex].

[70] H. David Politzer. "Reliable Perturbative Results for Strong Interactions?" In: *Phys. Rev. Lett.* 30 (1973). Ed. by J. C. Taylor, pp. 1346–1349. DOI: 10.1103/PhysRevLett.30.1346.

[71] D. J. Gross and Frank Wilczek. "Asymptotically Free Gauge Theories - I". In: *Phys. Rev. D* 8 (1973), pp. 3633–3652. DOI: 10.1103/PhysRevD.8.3633.